DC Dissertation

Magnetism and Hall Effect in Intermetallic Compounds with Noncollinear Spin Textures

非共線磁気構造を持つ金属間化合物の磁性とホール効果

Hiroaki HAYASHI

Supervisor: Prof. Kazunari YAMAURA

Hokkaido University
Graduate School of Chemical Sciences and Engineering

March 2024

Acknowledgements

I would like to offer my special thanks to Prof. Kazunari Yamaura for giving me a great opportunity to join his group. He gave me constructive comments and a warm encouragement in my whole doctoral research life. I have actively engaged in experiments and participated in conferences, allowing me to make significant progress as a researcher. Thanks to these experiences, I have really enjoyed my research. I would also like to express my deepest gratitude to Prof. Hiroyuki K. Yoshida and Prof. Yoshihiro Tsujimoto for their continuous support and instructive advice. I am indeed encouraged their gracious words many times.

I would like to express my special thanks to Prof. Kosei Ueno and Prof. Kiyoharu Tadanaga. They gave me the valuable comments and thoughtful feedback in the review process of this dissertation.

I sincerely thank Dr. Hiroya Sakurai who promote this research and my own growth. Not only discussions but also many of daily conversations were valuable and enjoyable. In addition, the researchers in NIMS, especially, Dr. Alexei Belik, Dr. Fumio Kawamura, Dr. Naoki Kikugawa, Dr. Taichi Terashima, and Dr. Yoshitaka Matsushita gave me a helpful discussion. I gratefully appreciate their constructive comments and insightful suggestions. Besides, I thank the member of my research group, Dr. Yuichi Shirako, Dr. Masayuki Fukuda, Ms. Xun Kang, Mr. Yu Meng, Mr. Shaoxuan Li, and Mr. Xuan Liang for their daily support and kindness.

My research is also indebted to Dr. Masahiko Isobe and Dr. Pascal Puphal in Max Planck Institute, Stuttgart, Germany. I appreciate for giving me a wonderful opportunity and their instructions of prominent expertise. I would also thank the group members, Ms. Apushkinskaya Olga, Mr. Christof Busch, Mr. Dorner-Finkbeiner, Ms. LorenzLacher Sabine, and Ms. Schwarz, Kersten for their warm welcome and a kind support. Thanks to them, I had precious experiences in my stay in Stuttgart.

I would like to express my gratitude to Prof. Hironori Nakao in High Energy Accelerator Research Organization (KEK). His support and active stance encouraged me many times as I had a tough time with my experiments.

I appreciate useful discussions and daily conversations with Prof. Migaku Oda, Mr. Yuto Ishii, Ms. Moyu Kato, and the members of Electronic Properties of Solids Laboratory in Hokkaido University. They continued to warmly welcome me after I graduated from the laboratory, and I could refresh myself in pleasant conversations with them.

Finally, I am very grateful to my family and friends for giving me a generous support and a warm encouragement, and thanks to all of them, I have had an invaluable time.

Contents

Chapter 1

Introduction

1.1 Spin textures

Strongly correlated electron system provides various electromagnetic properties by orbital hybridization between localized spins and itinerant electrons. In particular, the correlation among the charge, orbital, and spin degrees of freedom produces exotic properties such as unconventional superconductivity and cross-correlated phenomena [1, 2].

Spin textures are the spatial arrangement of spins produced by the interaction between electrons and can be broadly classified into two types: collinear spin structures and noncollinear spin structures as shown in Fig.1.1 [3]. In collinear spin structures, all spins are in a parallel or antiparallel to each other, e.g. ferromagnetic and antiferromagnetic structures. On the other hand, in noncollinear spin structures: helimagnetic structures and magnetic skyrmion structures, all spins are not in a parallel (antiparallel) to each other. Furthermore, noncollinear spin structures are classified into two types: coplanar and noncoplanar spin structures. In coplanar spin structures, all spins are aligned on one plane, and single-propagation vector Q is defined perpendicular to that spin rotating plane, as in a helical spin structure. On the other hand, in noncoplanar spin structures, all spins are not in one plane as in a magnetic skyrmion structure. In noncoplanar spin structures, at least two propagation vectors are defined, being called multi-Q states.

A vector spin chirality and a scalar spin chirality characterize noncollinear and noncoplanar magnetic structures, respectively. The vector spin chirality κ_{ij} calculating between two neighboring spins S_i and S_j, and the spin scalar chirality χ_{ijk} calculating among three neighboring spins S_i, S_j, and S_k, are defined as

$$\kappa_{ij} = S_i \times S_j, \tag{1.1}$$

and

$$\chi_{ijk} = S_i \dot{(} S_j \times S_k). \tag{1.2}$$

The former, as is clear from the definition, is equal to zero if the two spins are aligned to one direction (Collinear) and non-zero if they are not (Noncollinear). In the same way, the latter is non-zero if the three spins are in not in a plane (noncoplanar) as shown in Fig.1.2. The finite scalar spin chirality in noncoplanar spin textures affects itinerant electrons as an effective magnetic field through the spin-charge coupling arising from hybridization between itinerant electrons and localized spins [4, 5]. Here, the Berry phase that an itinerant electron acquires

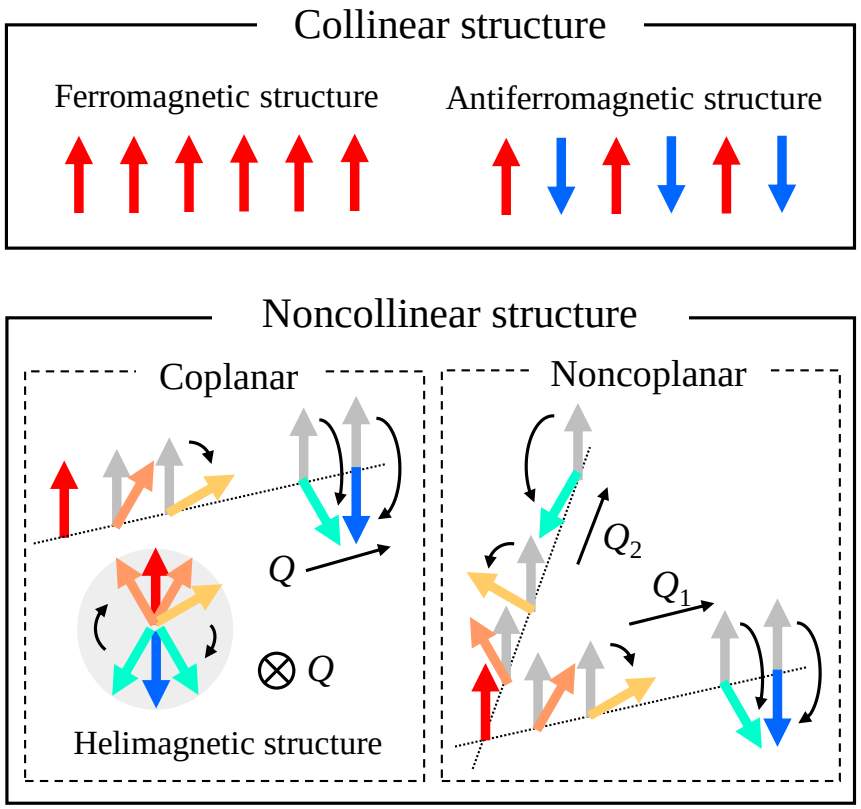

Figure 1.1: Classification of spin textures: collinear and noncollinear structure. In collinear structures, spins are aligned parallel (ferromagnetic) and antiparallel (antiferromagnetic). The noncollinear structures are futher classified into coplanar and noncoplanar structures. In these structures, spin rotation propagates one (two or more) direction, which structures are defined as single- (double- or multi-) Q state.

by circling the three neighboring spins $i \to j \to k \to i$ is proportional to χ, being equivalent to the phase acquired by itinerant electrons under an external magnetic field, which acts as an effective magnetic field for itinerant electrons. In other words, the noncoplanar spin structures are the intrinsic origin of electromagnetic response induced by external magnetic fields, such as the Hall effect [5–7]. The anomalous Hall effect of scalar spin chirality (topological Hall effect) will be discussed in section 1.2.

I have focused only on a spin degrees of freedom of electrons to discuss magnetic structures, whereas an orbital degrees of freedom are also important in considering magnetism. This orbital degrees of freedom (orbital angular momentum) is attributed to the orbital motion of the electrons, which hybridizes with the spin degrees of freedom (spin angular momentum) to each other, resulting in a predominance of spin-orbit interactions. Therefore, orbital effects are expected to influence magnetic properties. Exotic properties often appear in the systems with effective spin-orbit coupling, however, are difficult to describe the convoluted hybridization of both degrees of freedom. For the unified understanding of the two degrees of freedom, the concept of *multipole* was established, which enables us to express an anisotropy of a magnetic

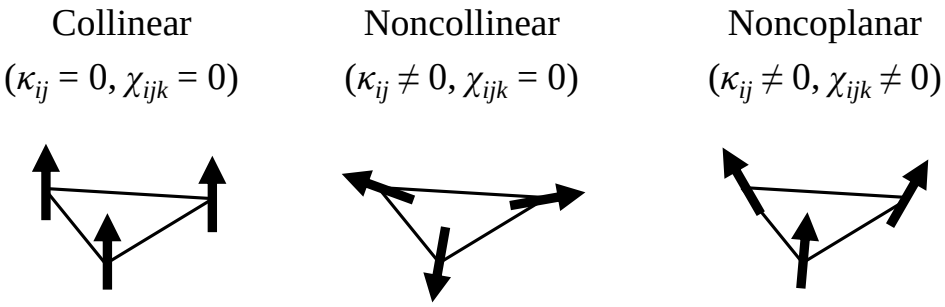

Vector spin chirality: $\kappa_{ij} = (S_1 \times S_2)$

Scalar spin chirality: $\chi_{ijk} = S_1 \cdot (S_2 \times S_3)$

Figure 1.2: The definition of a vector spin chirality and scalar spin chirality in collinear, noncollinear, and noncoplaner spin structures.

distribution and a charge distribution due to the spin degrees of freedom and the orbital degrees of freedom, simultaneously. Here, the unified anisotropy of the magnetic and charge distributions are called magnetic and electric multipole, respectively. Recently, the possibility of higher-order multipole, such as magnetic octupole, electric hexadecapole, and so on, has been proposed and actively studied both experimentally and theoretically [8, 9].

1.1.1 Magnetic skyrmions

Magnetic skyrmion crystals are representative as a typical noncoplanar spin textures with triple-Q state characterized by the superposition of three different spin propagation vectors [10–13]. The skyrmion crystal, topologically nontrivial spin vortex textures, given by the spin configuration superposed on multiple helical spin structures, are expressed by skyrmion number n_{sk}, and which is described as

$$n_{\mathrm{sk}} = \frac{1}{4\pi} \int \boldsymbol{M} \cdot \left(\frac{\partial \boldsymbol{M}}{\partial x} \times \frac{\partial \boldsymbol{M}}{\partial x} \right) dxdy, \tag{1.3}$$

where M is the unit vector of the direction of local spins [14]. The skyrmion number n_{sk}, in other words, is the number of times the projected spins in the magnetic unit cell covers the unit sphere as shown in Fig.1.3. In coplanar spin structures, n_{sk} is equal to zero as well as spin scalar chirality. On the other hand, $n_{\mathrm{sk}} = 0$ is permitted in noncoplanar spin structures with finite spin scalar chirality. Magnetic structures with $n_{\mathrm{sk}} = 0$ are distinguished topologically nontrivial magnetic structures, while those with $n_{\mathrm{sk}} \neq 0$ are topologically nontrivial magnetic structures. In addition, skyrmion crystals with $n_{\mathrm{sk}} = 1$ and $n_{\mathrm{sk}} = -1$ are called skyrmion and antiskyrmion, respectively.

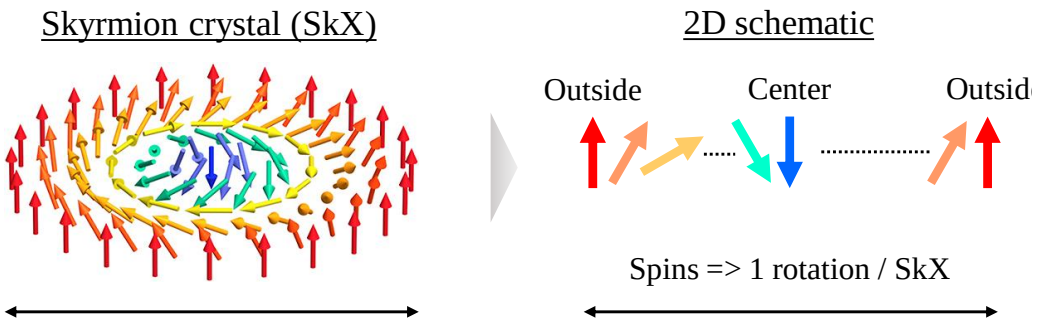

Figure 1.3: The schematics of magnetic skyrmion crystal (SkX). When the skyrmion number is equal to ±1, the spins are one rotation per SkX.

1.1.2 Dzyaloshinskii-Moriya (DM) interaction in chiral magnet MnSi

Skyrmion crystals were first observed in cubic chiral magnet, MnSi, breaking both spatial inversion symmetry and crystal chirality in crystal structure [15, 16]. Figure 1.4 (a) shows the temperature-magnetic field phase diagram of MnSi, in which the skyrmion crystals appear in phase A, in the finite temperature and magnetic field region. The cubic chiral magnets are described by the following Hamiltonian [17]

$$\mathcal{H} = \int dr \left[\frac{J}{2} \nabla \boldsymbol{S}(r)^2 + D\boldsymbol{S}(r) \cdot \nabla \times \boldsymbol{S}(r) - \boldsymbol{H} \cdot \boldsymbol{S}(r) \right], \tag{1.4}$$

where $\boldsymbol{S}(r)$ denotes the localized spin at position r in real space. The first term represents the ferromagnetic exchange interaction $J(> 0)$, the second term the Dzyaloshinskii-Moriya (DM) interaction D [18, 19], and the third term the Zeeman coupling of the localized spins with the magnetic field H. The DM interaction arising from noncentrosymmetric crystal structure favors helical magnetic ordering. In Eq.1.4, the ferromagnetic state becomes the ground state due to the ferromagnetic exchange interaction with $D = 0$ and $H = 0$, whereas the helical magnetic state becomes the ground state due to the DM interaction with $D \neq 0$ and $H = 0$. The rotation angle $|Q|$ in helical magnetic state is equal to the ratio D/J, consequently, the rotation angle D/J is generally small. Therefore, period of the helical propagation is sufficiently longer than the lattice constant.

The microscopic stabilization mechanism of the skyrmion crystal in MnSi is understood as a hybridization of DM interaction and thermal fluctuations [15, 20, 21]. First, since a skyrmion crystal is characterized by superposition of helical magnetic structures, dominant DM interaction is required to stabilize skyrmion crystals. In MnSi under intermediate magnetic field, the helical magnetic structures are stabilized by DM interaction. In addition to this, by thermal fluctuations, the skyrmion crystals are stabilized. In fact, theoretical calculations using mean-field theory exhibits that the conical phase is always emerged in the lowest energy state without thermal fluctuations, while skyrmion crystals are emerged with thermal fluctuations [15].

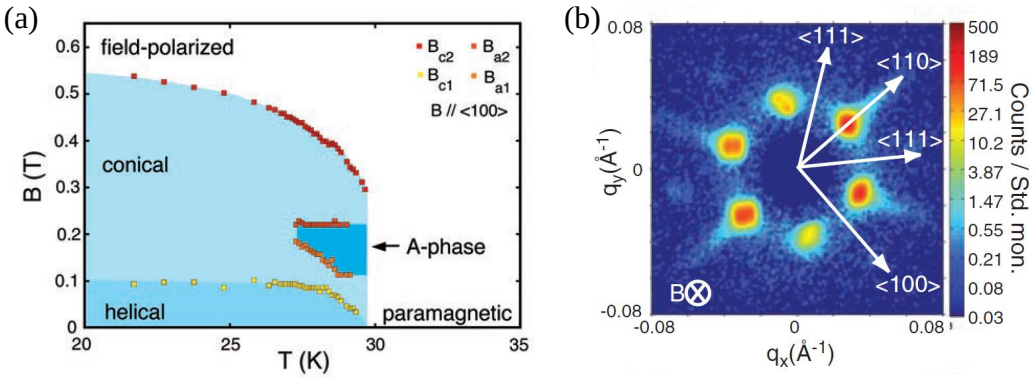

Figure 1.4: (a) The temperature-magnetic field phase diagram of chiral magnet, MnSi [15]. (b) The neutron scattering profile obtained at T = 26.45 K and H = 0.164 T [15].

1.1.3 Magnetic multipole

Magnetic multipoles were originally used in classical electromagnetism to describe anisotropic charge and magnetic charge distributions in real space. On the other hand, they can also be applied to quantum mechanics, which is composed of microscopic scales like electrons. The introduction of such a multipole concept can explain not only the simple conventional charge and magnetic orders, but also the complex interplay of charge, spin, and orbital degrees of freedom in solid state materials. Here I present the various types of multipoles (Fig.1.5).

Magnetic monopole: A magnetic monopole moment is a fundamental magnetic moment, a state in which a single magnetic pole (north or south pole) exists. It is usually predicted to exist in theoretical discussions, however has not yet been found in compounds. On the other hand, by considering some spins as clusters, pseudo magnetic monopoles can be represented like a hedgehog skyrmion.

Magnetic dipole: A magnetic dipole is composed of two precisely contrasting magnetic poles, which is the most common magnetic moment such as magnetic spins.

Magnetic quadrupole: A magnetic quadrupole consists of four symmetrical magnetic poles and has a more complex structure than a dipole. It can be observed in certain crystal structures and magnets.

Magnetic octupole: Magnetic Octupoles consist of eight magnetic poles and represent a very high-order multipole structure. It is usually observed only in certain materials under special conditions. In Mn_3Sb, Mn spins form a cluster magnetic octupole, thus exhibit large anomalous Hall effect.

Mathematically, multipole systems are just extended systems with more independent degrees of freedom, such as the Ising model with 1 degree of freedom, the Heisenberg model with 3 degrees of freedom, the SU(3) model with 8 degrees of freedom, etc. On the other hand, in condensed matter physics, each degree of freedom shows different electrical and magnetic responses, resulting in interesting properties. Furthermore, these degrees of freedom are mutually

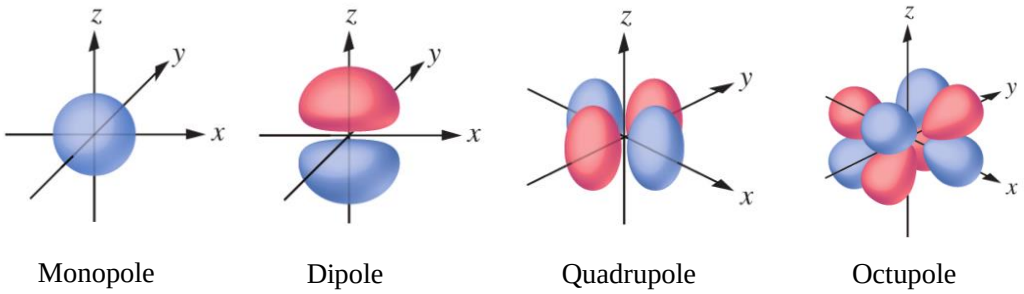

Figure 1.5: The schematics of various types of multipoles. From left to right are monopole, dipole, quadrupole, and octupole [22].

intertwined and produce unexpected responses, which are still difficult to observe directly at present.

1.2 Hall effect

The Hall effect was discovered by Edwin Hall in 1879 and described as

$$\rho_{\mathrm{yx}} = R_0 B + 4\pi R_{\mathrm{SM}} + \rho^{\mathrm{T}}_{yx} \tag{1.5}$$

including the normal Hall effect proportional to the external magnetic field B [23], the anomalous Hall effect proportional to the spontaneous magnetization M [24, 25], and the topological Hall effect proportional to the scalar spin chirality χ [4–7, 26, 27]. Here, R_0 is the normal Hall coefficient and R_{S} is the anomalous Hall coefficient [28].

The normal Hall effect is a phenomenon where itinerant electrons in a paramagnetic metal exhibit cyclotron motion due to the Lorentz force induced by a magnetic field, resulting in an electric field in the direction perpendicular to both the current and the magnetic field. Whereas, the anomalous Hall effect is understood as a phenomenon where Hall resistance appears proportional to the spontaneous magnetization M in a magnetic compound, and the anomalous Hall coefficient R_{S} is known to show a strong temperature dependence. In the case of ferromagnetic Ni, for example, R_{S} decreases as the temperature approaches absolute zero, while it reaches a maximum around the Curie temperature T_{C} and then becomes zero again in the paramagnetic phase at higher temperatures (Fig.1.6) [29]. The origin of this behavior can be distinguished into intrinsic and extrinsic mechanisms as written later. The topological Hall effect is the scattering of itinerant electrons by the topologically nontrivial magnetic structure of skyrmion crystals. Therefore, it is independent of magnetic field and magnetization and is induced via the Berry phase [6, 7, 26, 27].

In general, the anomalous Hall effect can be classified into intrinsic and extrinsic mechanisms. The former [30], considering orbital motion of electrons ($\sim$ Bloch electrons) under a virtual magnetic field is understood as the scattering of itinerant electrons through the Berry phase derived from the geometry of the electron wave function $\Omega_{\mathrm{B}}(k)$ [31]. To understand the mechanism of intrinsic Hall effect and Berry phase in detail, consider itinerant spins in systems with finite scalar spin chirality [4, 5]. In systems with a strong Hund's coupling J_{H} between

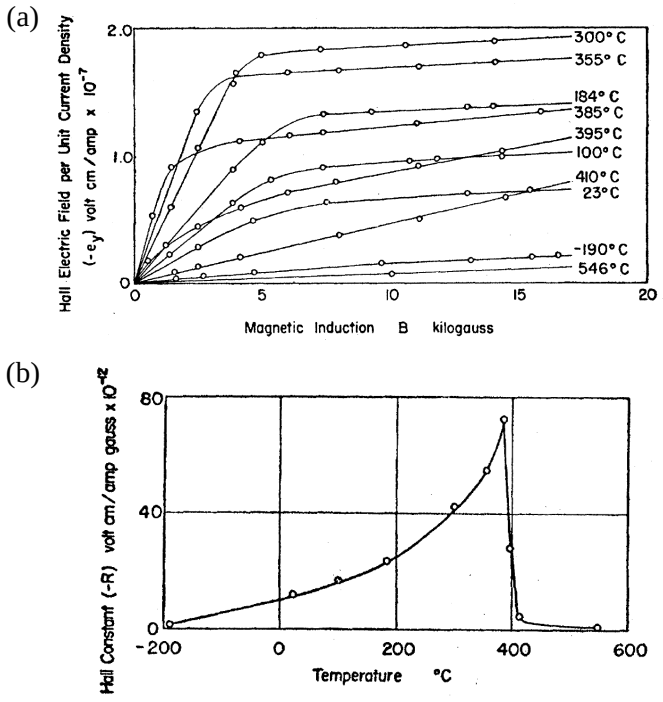

Figure 1.6: (a) Hall effect in nickel. (b) The temperature dependence of the anomalous Hall coefficient R_{H} in nickel [29].

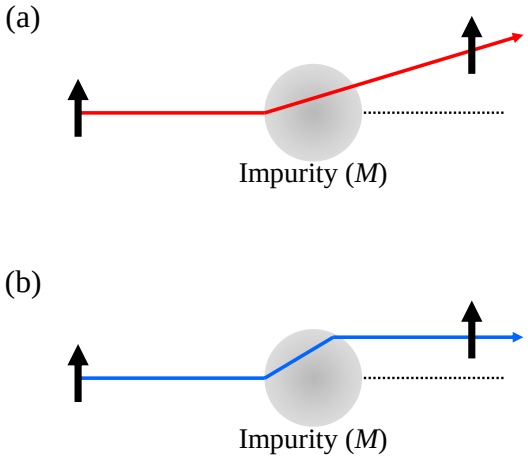

Figure 1.7: The schematics of (a) skew scattering and (b) side jump scattering in extrinsic anomalous Hall effect.

itinerant and localized spins, the itinerant spins are aligned to parallel on each sites of localized spins. Here, considering hopping from site i to j, the Hamiltonian is described as

$$\mathcal{H} = -\sum_{ij}(t_{ij}^{\mathrm{eff}} c_i^{\dagger} c_j + h.c.), \tag{1.6}$$

where $c_i^{\dagger}(c_i)$ is itinerant electron creation (annihilation) operator on site i. When J_{H} is strong enough, the wave function at site i of the itinerant is expressed as

$$|\chi\rangle = {}^{t}\left[e^{ib_i}\cos\left(\frac{\theta_i}{2}\right), e^{ib_i+\phi_i}\sin\left(\frac{\theta_i}{2}\right)\right], \tag{1.7}$$

where θ_i and ϕ_i are the polar coordinates of the localized spin at the i site. The overall phase bi corresponds to the gauge degrees of freedom and does not appear in physical quantities. Therefore, the effective transfer integral ti j_{eff} is given by

$$\begin{aligned} t_{ij}^{\mathrm{eff}} &= t\langle\chi_i|\chi_j\rangle \\ &= te^{i(-b_i+b_j)}\left[\cos\left(\frac{\theta_i}{2}\right)\cos\left(\frac{\theta_j}{2}\right) + e^{\phi_i+\phi_j}\sin\left(\frac{\theta_i}{2}\right)\sin\left(\frac{\theta_j}{2}\right)\right] \\ &= te^{ia_{ij}}\cos\left(\frac{\theta_{ij}}{2}\right). \end{aligned} \tag{1.8}$$

Here, θ_{ij} is the angle between the localized spins S_i and S_j, and the phase a_{ij} is the vector potential generated by the spins, corresponding to the Berry phase. When the itinerant spin is hopping like $1 \to 2 \to 3 \to 1$, a noncoplanar spin structure with finite scalar spin chirality consisting of three sites (Fig.1.2) can be denoted as

$$\begin{aligned} \langle \boldsymbol{n_1}|\boldsymbol{n_3}\rangle\langle \boldsymbol{n_3}|\boldsymbol{n_2}\rangle\langle \boldsymbol{n_2}|\boldsymbol{n_1}\rangle &= (1 + \boldsymbol{n_1}\cdot\boldsymbol{n_2} + \boldsymbol{n_2}\cdot\boldsymbol{n_3} + \boldsymbol{n_3}\cdot\boldsymbol{n_1}) + i\boldsymbol{n_1}\cdot(\boldsymbol{n_2}\times\boldsymbol{n_3}) \\ &\propto e^{i(a_{12}+a_{23}+a_{31})} \\ &= e^{i\Omega/2}, \end{aligned} \tag{1.9}$$

where $|\boldsymbol{n_i}\rangle$ is the two-component spinor wave function of the spin polarized along $\boldsymbol{n_i} = \boldsymbol{S_i}/|\boldsymbol{S_i}|$ direction. The itinerant spins acquire a phase factor $\Omega_{\mathrm{B}} = a_{12}+a_{23}+a_{31}$. This phase factor is the Berry phase, which corresponds to half the value of solid angle Ω between three spins created on the unit sphere. When a spin structure with finite scalar spin chirality is realized, the Berry phase is emerged and affects to the itinerant electrons as a virtual magnetic field, just like a real magnetic field. The result is the anomalous Hall effect.

Recently, this mechanism has been associated with topology, and is called the topological Hall effect. In this thesis, the topological Hall effect is distinguished as the anomalous Hall effect due to the intrinsic mechanism. On the other hand, the latter is distinguished into skew scattering [32, 33] and side jump scattering [34]. In skew scattering, up and down spins are scattered by impurities via spin-orbit interaction. Here, the interaction shows different sign $\lambda_S \cdot L$ depending on the spin direction, therefore, each spins are scattered to opposite directions. The incident wave and the scattered wave have different wavenumber. On the other hand, in side jump scattering, conduction-electron orbitals are shifted by impurity scattering without changing the wavenumber. Schematics of the anomalous Hall effect due to skew scattering and side jump scattering are shown in Fig.1.7 (a) and (b), respectively.

1.3 Application aspects

1.3.1 Hall sensor

A Hall sensor is one of the typical magnetic sensors using semiconductors. In general, Hall Effect sensors consist of a thin semiconductor material through a continuous current flows. When a magnetic field is applied perpendicular to the direction of current flow, it creates a voltage difference across the semiconductor material. This voltage, known as the Hall voltage, is proportional to the strength of the magnetic field. Actually, Hall sensors convert the strength and direction of a magnetic field into the magnitude and positive/negative of a voltage. Their main applications are detection of rotation, position, open/close, current, and orientation. The most common example is in non-contact switch applications such as open/close detection of refrigerator doors, electronic equipment lids and cases, etc. Hall sensors can be broadly classified into three types as shown below [35].

Latch type

In the latch type, the output voltage gets high (low) when the N-pole (S-pole) approaches, and the output state is maintained even when the N-pole (S-pole) are leaved. In other words, once the N-pole changes the voltage to high, it is necessary to move the S-pole closer in order to change to low. Latch type one applies the effect of magnetic hysteresis and is currently used in the automotive industry. Figure 1.8 (a) shows the latch type operation mechanism, where the horizontal axis is the strength of the magnetic field and the vertical axis is the voltage level of the output signal.

Switch type

In the switch type, the output gets low when the magnets are close to each other and gets high when they leave. There are also two types of switch types: unipolar (single-pole detection) and omnipolar (double-pole detection). Unipolar detection responds only to either the N-pole or S-pole, while omnipolar detection responds to both the N-pole and S-pole. The switch type sensor has a basic on/off action and detects magnetic fields simply and effectively. Therefore, as a simple sensor, it is used for open/close sensing, proximity detection, and security systems. Figure 1.8 (b) shows the operation mechanism in the case of omnipolar detection.

Analog type

The output voltage of the analog output type varies linearly with the strength of the N-pole/S-pole as shown in Fig.1.8. In other words, the output voltage increases (decreases) by N-pole (S-pole) getting closer to the Hall sensor, allowing more precise detection of the degree and direction of changes in the magnetic field. Due to their continuous signal output, analog Hall sensors are suitable for applications requiring high accuracy and detailed monitoring of magnetic field fluctuations such as position detection, angle sensing, magnetic field mapping.

Recently, in addition, Hall sensors that do not require a magnetic field have been attracted much attention, and the anomalous Hall effect is applied for this purpose. As already explained, the anomalous Hall effect utilizes the magnetization (mainly ferromagnetism) of a material as a scattering source of itinerant electrons.

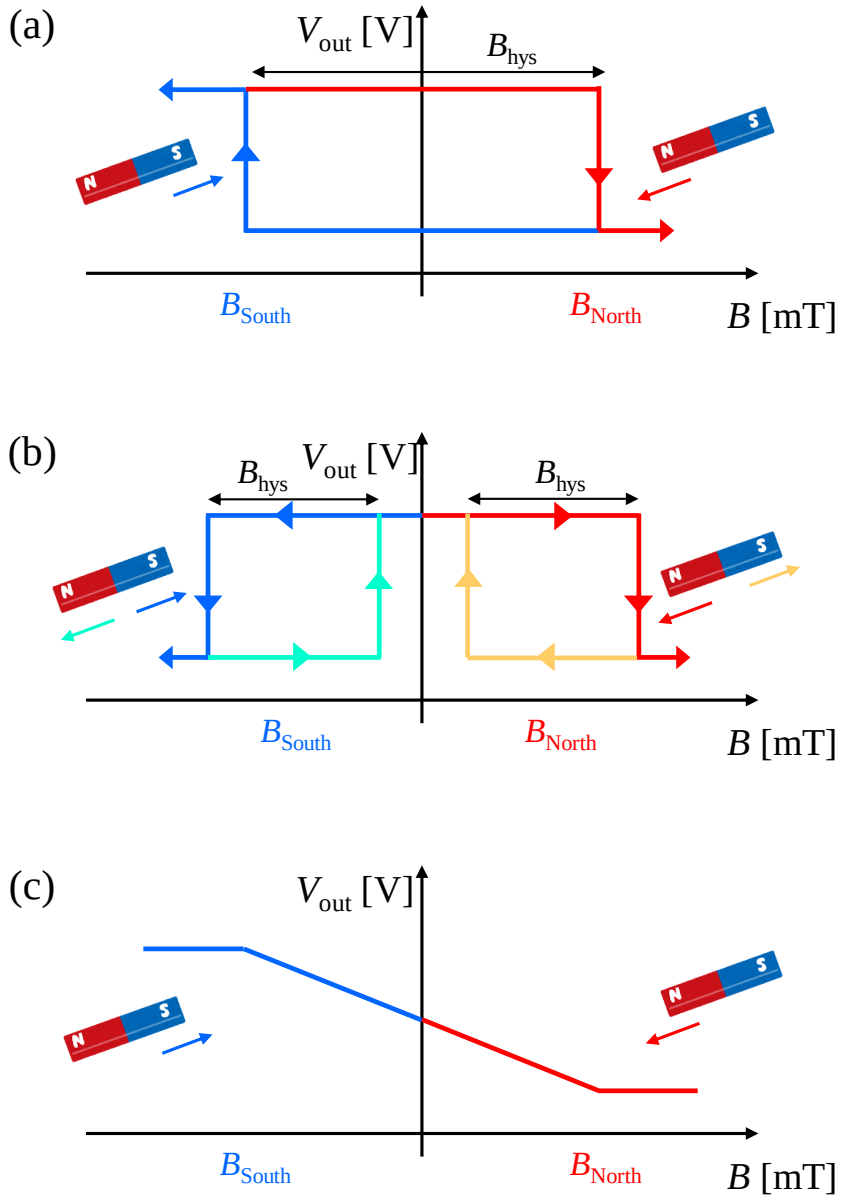

Figure 1.8: The operation mechanisms for (a) latch type, (b) switch type, and (c) analog type Hall sensors.

1.3.2 Skyrmion memory

Because of topological features of skyrmion crystals, they are robust against external disturbances such as thermal fluctuations and magnetic fields, and exhibit a larger electromagnetic response to small external field than trivial magnetic structures. Therefore, skyrmion crystals are attracting many researchers' attention as an innovative magnetic structure for realizing stable and power-saving magnetic memory and computing devices. In addition, recent studies have gradually revealed that low-energy excitation of skyrmion crystals have various device functions such as microwave rectification effects, microwave-to-voltage conversion, and high-sensitivity magnetic field detection. Here, I present the advantages for applying skyrmions to magnetic devices.

Stability: Skyrmions are more stable than traditional magnetic domains, making them stable to external perturbations.
Small size: Skyrmions can be much smaller than magnetic domains, potentially allowing for higher data storage density.
Low energy consumption: The manipulation of skyrmions can be achieved with lower energy consumption compared to some other magnetic memory technologies.

These advantages have led to a variety of applied research of skyrmions. To realize practical skyrmion memory devices, topologically protected information carriers must be generated and manipulated in materials to achieve both writing and addressing functions. Also, in such devices, binary data bits "1" and "0" are suggested to be represented by existence and absence of skyrmions, respectively. The following are some of the most recent and attractive ones.

Skyrmion shift device for memory

While much theoretical research has focused on skyrmion memory [36], here I present some experimental studies that have attracted a lot of attention. At first, the concept of skyrmion based magnetic memory is depicted in Fig.1.9 (a) [37]. The skyrmion with topologically protected spin swirling texture is more stable than other ordinary magnetic structures, therefore, the presence and absence of a skyrmion are regarded as "1" and "0" information. Figure 1.9 (b) shows the relationship between the distance between each of the individual skyrmions and the number of skyrmions. Obviously, the larger the number of skyrmions, the shorter the distance between the skyrmions and the higher density state can be realized. Figure 1.9 also indicates a model and experimental realization in which the presence and absence of a skyrmion corresponds to the information "1" and "0". Here, "1" and "0" represents a skyrmion and a ferromagnetic domain as illustrated in Fig.1.9.

Next, I introduce how to create and control skyrmions, which are reported by W. Jiang, *et al*. [38], and G. Yu *et al*. [39]. To generate single skyrmion, the mechanism of soap bubble formation from thin films is applied. Figure 1.10 shows how a magnetic topological structure, a skirmion bubble, is formed in a solid system in a similar manner: applying a pulsed current to the chiral stripes in the left container, a single skyrmion is generated in the right container. This single skyrmion can be moved by applying current, and the direction of movement can be controlled by switching the direction of current application. Furthermore, during the shifting of skyrmions, no new skyrmion was generated, confirming the selective device operation controlled by the pulse shape.

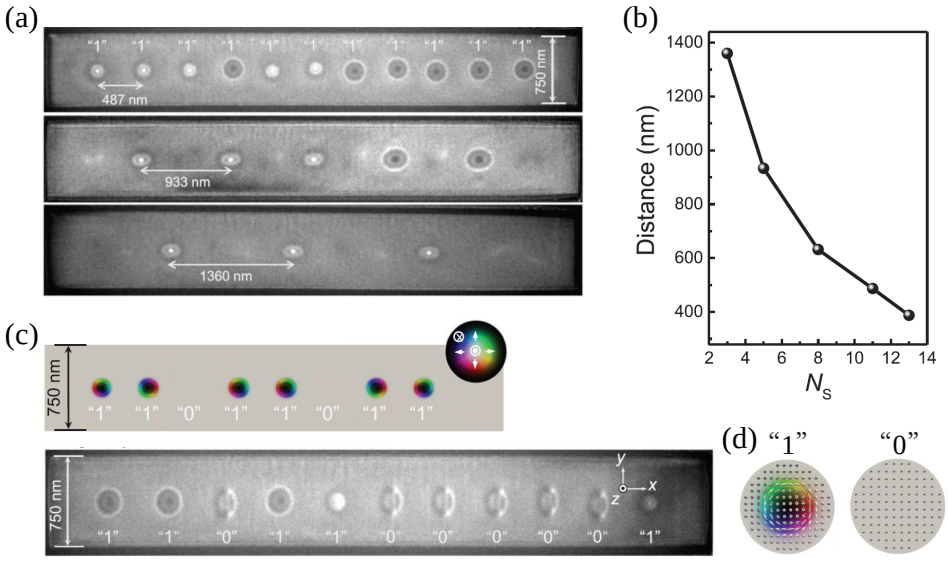

Figure 1.9: The skyrmion based magnetic memory [37]. (a) Variation of the distance between the two nearest skyrmions in Fe_3Sn_2 nanostripes under a magnetic field of 450 mT. (b) The skyrmion number N_S dependence of distance between the two nearest skyrmions in the nanostripes under a magnetic field of 450 mT. (c) Experimental realization of a single skyrmion in the 750 nm width Fe_3Sn_2 nanostripe, with an out-of-plane magnetic field of 450 mT and an in-plane field component of 39 mT along y axis. (d) The magnetic configuration of skyrmion ("1") and ferromagnetic domain ("0").

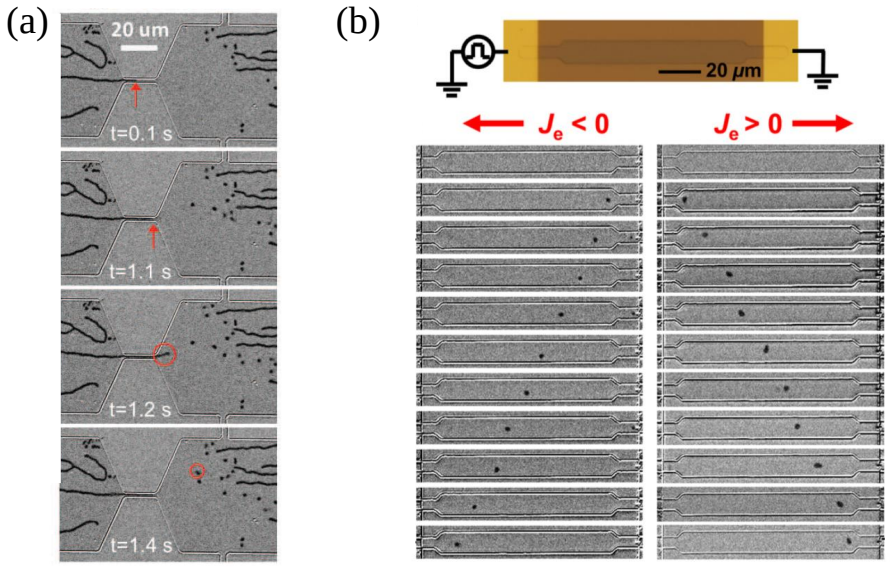

Figure 1.10: (a) Capturing the transformational dynamics from stripe domains to skyrmions and motion of skyrmions. From a top photo, the stripe domains are forced to pass through the constriction and are eventually converted into skyrmions at the right side of the device by constant current density $j_e = +6.4 \times 10^4$ A/cm^2 under +0.46 mT. (b) The skyrmion generation and motion driven by a current pulse for negative and positive direction.

1.4 Recent research

In this section, I introduce the recent studies about skyrmions and anomalous Hall effect in new compounds. In these studies, some novel theories that differ from conventional mechanisms and precise experiments supporting these theories have been reported. Furthermore, some compounds, far surpass conventional properties have been discovered.

1.4.1 Centrosymmetric skyrmion compounds

Initially, magnetic skyrmions were observed only in materials without crystallographic inversion center. Examples include MnSi, EuPtSi, and FeGe, where the Dzyaloshinski-Moriya interaction plays a pivotal role in magnetism [7, 12, 40–42]. However, theoretical advancements have proposed the possibility of skyrmion formation even in compounds with centrosymmetry [43–48]. For instance, in J_1-J_2(J_3) triangular-lattice antiferromagnets, geometrical frustration was predicted to lead to the emergence of skyrmion lattices, despite these systems being insulating unlike their predecessors [49]. Additionally, skyrmions observed in the Gd^{3+} triangular lattices in Gd_2PdSi_3 [50–53] and the breathing kagome networks in $Gd_3Ru_4Al_{12}$ [54–56] further support the influence of this magnetic frustration.

More recently, it has been suggested that the skyrmion lattice may also manifest in non-frustrated lattices with centrosymmetry and metallic attributes. The interplay between the Ruderman-Kittel-Kasuya-Yoshida (RKKY) interaction and multiple spin interaction is considered crucial in this context. This possibility was demonstrated in studies of the tetragonal

compound $GdRu_2Si_2$ [57–62]. These findings suggest the ubiquitous presence of skyrmions across a variety of material systems.

Another important aspect of the skyrmion lattice is related to its characteristic transport properties. In particular, the topological Hall effect manifests itself in connection with the skyrmion lattice [7, 63–65] due to the scalar spin chirality $S_i(S_j \times S_k)$, which acts like a fictitious magnetic field. However, only a few metallic compounds with special inversion symmetry currently studied show the existence of a skyrmion lattice [53, 56–58, 66]. Among them, I will introduce Gd_2PdSi_3 and $GdRu_2Si_2$ which have attracted great attention due to their multi-Q-skyrmion lattice and complex magnetic phase diagram [53, 58].

Gd_2PdSi_3

A centrosummetric intermetallic magnet, Gd_2PdSi_3 exhibits skyrmion lattice on a triangular lattice with magnetic frustration [43, 48, 49]. Here, let us considering the following Hamiltonian on a triangular lattice [49],

$$\mathcal{H} = -J_1 \sum_{<ij>} \boldsymbol{S}_i \cdot \boldsymbol{S}_j - J_3 \sum_{<<ij>>} \boldsymbol{S}_i \cdot \boldsymbol{S}_j - H \sum_i S_i^z, \tag{1.10}$$

where $\boldsymbol{S}_i$ ($|\boldsymbol{S}_i| = 1$) is the localized spin on real space i. The first, second, and third terms represent the nearest-neighbor ferromagnetic exchange interaction $J_1(> 0)$, the third-neighbor antiferromagnetic exchange interaction $J_3(< 0)$, the effect of the magnetic field H in the z direction, respectively: when $J_3 = 0$ and $H = 0$, the ferromagnetic state becomes ground state by the nearest-neighbor ferromagnetic exchange interaction. On the other hand, when $J_3 \neq 0$, magnetic frustration occurs [Fig.1.11 (a)] and the ground state depends on the ratio of J_1 to J_3. In Fig.1.11 (a), both spin 1 and spin 2 are expected to align upwards due to ferromagnetic exchange interaction, as well as spin 3 due to ferromagnetic exchange interaction with spin 2. On the other hand, spin 3 also favors a down spin through antiferromagnetic exchange interaction with spin 1. In such a situation with strong magnetic frustration, a helical magnetic state is realized. Specifically, the ground state of this system is distinguished as ferromagnetic state ($J_1/|J_3| \geq 4$), and the helical state ($J_1/|J_3| < 4$). The rotation angle of the helical magnetic state is given by $|\boldsymbol{Q}| = 2\cos^{-1}\{(1 + \sqrt{1 - 2J_1/J_3})/4\}$, where $\boldsymbol{Q}$ is parallel to the nearest bond direction.

When $J_1/|J_3| < 4$, the ground state is expressed by three propagation vectors, $Q_1 \parallel (1, 0)$, $Q_2 \parallel (-1/2, 3/2)$, and $Q_3 \parallel (-1/2, -\sqrt{3}/2)$, suggesting double-$Q$ or triple-Q state as a superposition of multiple helical structures. However, in mean-field calculations without thermal fluctuations, the single-Q state is more stable regardless of temperature and magnetic field. Therefore, thermal fluctuation is important for stabilization of multiple-Q state in frustrated magnetic system as well as in chiral magnetic one. Figure 1.11 (b) illustrates the temperature-field phase diagram at $J_1/J_3 = -1/3$ obtained from theoretical calculations. Here, the Double-q, Triple-q (skyrmion phase), and Z phases appear with noncoplanar structures in a finite temperature and magnetic field region.

$GdRu_2Si_2$

$GdRu_2Si_2$ as a centrosymmetric skyrmion compound has attracted much attention. First, in order to understand the stabilization mechanism of noncoplanar structures (skyrmion lattice) in

sentrosymmetric crystals, let us consider Kondo lattice model in itinerant electron system,

$$\mathcal{H} = \sum_{ij\sigma} t_{ij} c^{\dagger}_{i\sigma} c_{j\sigma} - J \sum_{i\sigma\sigma'} c^{\dagger}_{i\sigma} \boldsymbol{\sigma}_{\sigma\sigma'} c_{i\sigma'} \cdot \boldsymbol{S}_i - H \sum_i S^z_i, \tag{1.11}$$

where $c^{\dagger}_{k\sigma}(c_{k\sigma})$ and $\boldsymbol{S}_i$ are creation (annihilation) operator of itinerant electron with spin σ and localized electron ($|\boldsymbol{S}_i| = 1$), respectively [45, 67]. The first term express the kinetic energy of the itinerant electron, and t_{ij} is the hopping integral from i to j. The second indicates the spin-charge coupling J, denoted by the Pauli matrix, $\boldsymbol{\sigma} = (\sigma^x, \sigma^y, \sigma^z)$, and the third represents an external field. By considering the situation where an energy scale of the spin-charge coupling is smaller than one of a bandwidth, Eq.1.11 is given

$$\mathcal{H} = \mathcal{H}_0 + \mathcal{H}', \tag{1.12}$$

$$\mathcal{H}_0 = \sum_{k\sigma} \epsilon_k c^{\dagger}_{k\sigma} c_{k\sigma}, \tag{1.13}$$

$$\mathcal{H}' = \frac{J}{\sqrt{N}} \sum_{kq\sigma\sigma'} c^{\dagger}_{k\sigma} \boldsymbol{\sigma}_{\sigma\sigma'} c_{k+q\sigma'} \cdot \boldsymbol{S}_q, \tag{1.14}$$

on reciprocal space [44, 68]. Here, N and $\boldsymbol{S}_q$ are the number of lattice points and the Fourier component of localized spins. Finally, the effective spin model is transformed [69–71]

$$\mathcal{H} = 2 \sum_{\nu} \left[-\tilde{J} \boldsymbol{S}_{Q_\nu} \cdot \boldsymbol{S}_{-Q_\nu} + \frac{K}{N} (\boldsymbol{S}_{Q_\nu} \cdot \boldsymbol{S}_{-Q_\nu})^2 \right], \tag{1.15}$$

where Q_ν is the wave vector with the maximum value of susceptibility χ^0_q ($\tilde{J} > 0$ and $K > 0$. In Eq.1.15, the first term represents the RKKY interaction, which induces a helical magnetic state, while the multiple spin interaction represented by the second term induces a mult-Q state. In this Hamiltonian, a magnetic frustration: itinerant frustration between the helical magnetic structure characterized by Q_1, and the double-Q state characterized by Q_1 and Q_2 exists. For instance, $|\boldsymbol{S}_{Q_1}|^2$ has a maximum value of $N/2$, thus obtaining the maximum energy gain from the RKKY interaction. However, since $K > 0$, it suffers the largest energy loss from multiple spin interactions. On the other hand, in the double-Q state, $|\boldsymbol{S}_{Q_1}|^2, |\boldsymbol{S}_{Q_2}|^2 < N/2$ due to harmonic components such as $|\boldsymbol{S}_{Q_1 \pm Q_2}|^2$ and $|\boldsymbol{S}_{-Q_1 \pm Q_2}|^2$. Considering the energy gain with respect to helical structures, the RKKY interaction is energetically unstable, while the multiple spin interaction is stable. This competition of both interactions, originated from itinerant electrons, is called the itinerant frustration (Fig.1.12).

Originating from this itinerant electron system, the Multi-Q state is stabilized in $GdRu_2Si_2$. Figure 1.12 (b) shows the crystal structure of $GdRu_2Si_2$, where the Gd^{3+} ions responsible for the magnetism form a square lattice, thus no geometric frustration occurs on Gd layers. On the other hand, itinerant electrons, mainly Ru-4d electrons, are responsible for conductivity, and the anisotropic contribution (K) is relatively larger in $GdRu_2Si_2$, which allows itinerant frustration to work effectively and a double-Q state (skyrmion lattice) to develop [Fig.1.12 (c)].

1.4.2 Large anomalous Hall effect in a noncollinear antiferromagnet

Mn_3Sn

Recent breakthroughs in both theory and experiment have provided a robust framework for understanding the anomalous Hall effect through the Berry-phase concepts [5]. This perspective

predicts that some specific magnetic states such as spin liquids and antiferromagnets trigger a anomalous Hall effect even in the absence of net spin magnetization [72–76]. While observed a spontaneous Hall effect in spin liquid states [77], the intriguing aspect is the absence of a zero-field anomalous Hall effect in antiferromagnets.

Here I introduce empirical evidence of large anomalous Hall conductivity in Mn_3Sn, an antiferromagnet without magnetization. Mn_3Sn has a hexagonal Ni_3Sn-type structure with space group $P6_3/mmc$ as shown in Fig.1.13 (a) [78, 79], and Mn spins order like noncollinear 120-degree spin texture at the Neel temperature of $T_N \sim 420K$ [Fig.1.13 (b)]. In this magnetic phase, an anomalous Hall conductivity of approximately $20\,\Omega^{-1}\,cm^{-1}$ at room temperature and over $100\,\Omega^{-1}\,cm^{-1}$ at 100 K were observed, being consistent with one in ferromagnetic metals as shown in Fig.1.13 [80].

Of particular note is the chiral antiferromagnetic state inherent in Mn_3Sn, indicating an extremely weak ferromagnetic moment of about $0.002\mu_B/Mn$ [78, 81]. Therefore, the switching of the direction of Hall effect with magnetic fields, as small as a few hundred Oe, make much easier. Due to this flexible response of this large anomalous Hall effect is useful for a various applications, including spintronics: i.e. a development of memory devices that generate almost no extra electric field.

1.5 Motivation

The purpose of this thesis is to develop novel intermetallic compounds, focusing on exotic transport properties such as anomalous Hall effect and topological Hall effect arising from new-type mechanisms. As shown in section 1.3, these transport properties has a potential of industrial applications as new magnetic materials, however, experimental investigations of them are entirely inadequate due to the limited variety of candidate compounds. The discovery of Mn_3Sn and of centrosymmetric skyrmion materials has shed light on this situation: since the restrictions on crystal structure and spin texture have been removed, the scope of material exploration has expanded, allowing for the development of devices with higher performance and stability. Recently, some of theoretical studies supporting these new mechanisms have attracted much attention, thus, further experimental verification is required. The aim of this study is to expand the materials field for the development of innovative magnetic devices based on their unique electrical conduction properties.

I also aim at obtaining higher performance materials. For instance, synthesis of new materials exhibiting a larger anomalous Hall resistance, a crystal growth of centrosymmetric skyrmion compounds, the observation of smaller size of skyrmion lattices, etc. Even if these materials cannot be directly made into magnetic devices, they are important research because the synthesis methods and mechanisms can be applied for other materials.

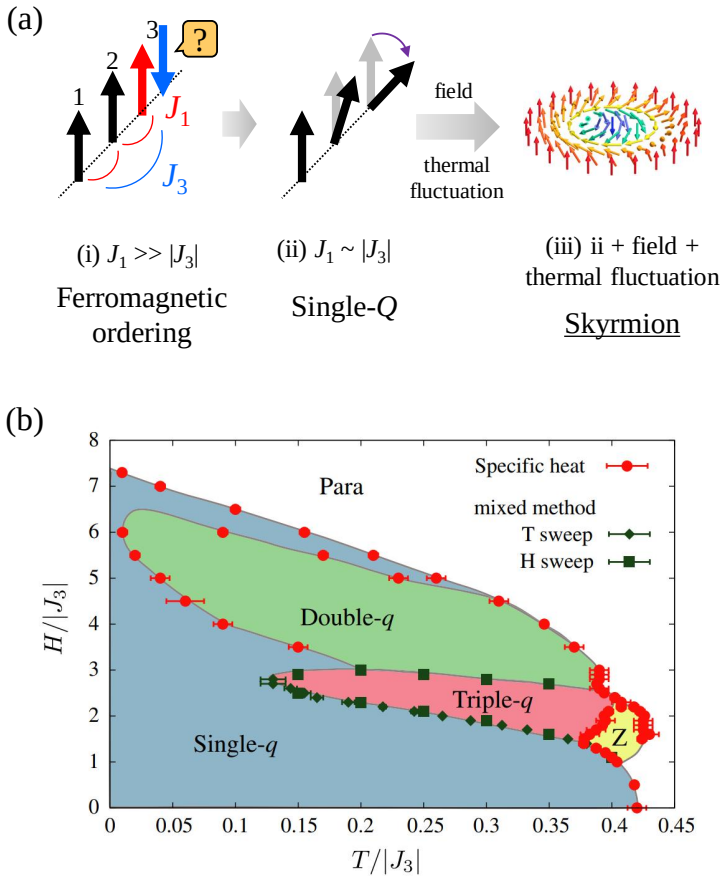

Figure 1.11: (a) Magnetic frustration due to the nearest-neighbor ferromagnetic exchange interaction J_1 and the third nearest-neigbor antiferromagnetic exchange interaction J_3. (b) Temperature-field phase diagram at $J_1/J_3 = -1/3$. The phase diagram was obtained from Monte Carlo simulations: Single-q, Double-q, Triple-q, Z, and Para corresponds to helical and conical structure, double-Q states with noncoplanar structures, the skyrmion phase, domain structures with $n_{\rm sk} = 1$ and $n_{\rm sk} = -1$ skyrmions, and paramagnetic state, respectively.

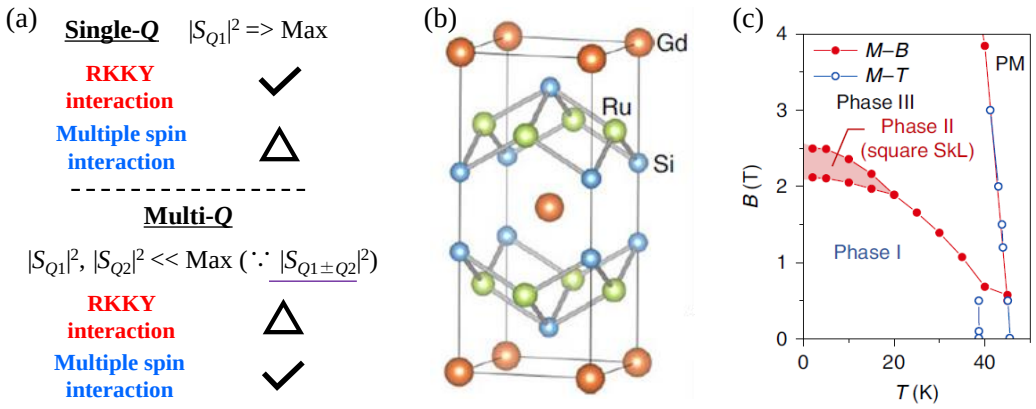

Figure 1.12: (a) The competition between RKKY interaction and multiple spin interaction in the itinerant electron system. In the single-Q state, the energy gain from the RKKY interaction is maximum (minimum from the Multiple Spin interaction), and in the Multi-Q state, the energy gain from the Multiple Spin interaction is maximum (minimum from the RKKY interaction). (b) The crystal structure and (c) the magnetic phase diagram of $GdRu_2Si_2$. In red-colored area, double-Q state (skyrmion lattice) is stabilized due to the large contribution from multiple spin interaction term.

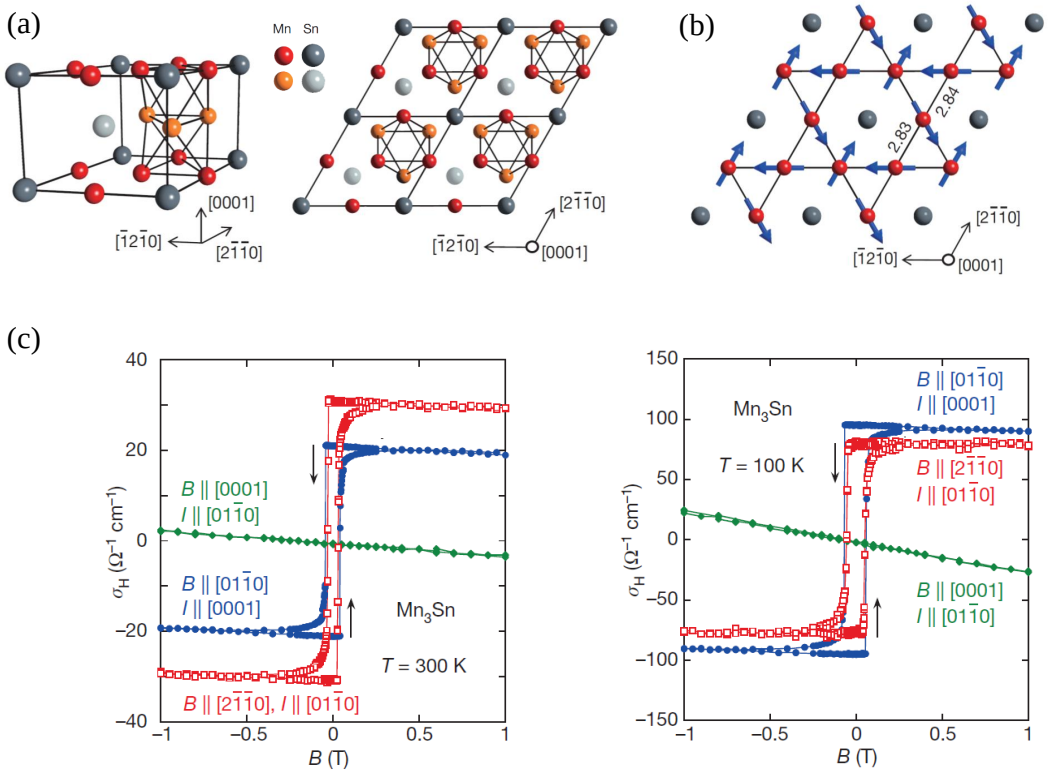

Figure 1.13: (a) The crystal structure of Mn_3Sn. The spheres colored red, orange, dark gray, and light gray indicate Mn ($z = 0$), Mn ($z = 1/2$), Sn ($z = 0$), and Sn ($z = 1/2$), respectively [80]. (b) An individual a–b plane of Mn_3Sn. Mn spins (blue arrows) form an inverse triangular spin structure, and has the local easy-axis parallel to the in-plane direction towards its nearest-neighbour Sn sites. Here, [2110], [1210] and [0001] are the a, b and c axes, respectively [80]. (c) The magnetic field dependence of Hall conductivity σ_H measured in $B \parallel$ [2110], [0110] and [0001] obtained at 300K (left) and 100K (right) [80].

Chapter 2

Experimental

In this chapter, several techniques for crystal growth and physical property measurements are noted. Details on the synthesis part of each compounds is summarized later.

2.1 Crystal growth

A major breakthrough in crystal growth technology came with the discovery of the electrical transistor by John Bardeen and Walter Houser Brattain at Bell Telephone Laboratories (US) in 1947. Since then, the focus of electronics technology development has shifted from vacuum tubes to transistors, and with this shift, several crystal growth methods centered on semiconductors such as Si and Ge were established. In solid state physics, crystal growth techniques play a crucial role in understanding the unique behavior of electrons. Here I will describe the crystal growing methods I have been working on.

2.1.1 Solid state method

Solid state reaction is one of the most widely used method for chemical synthesis from a mixture of solid reagents. In this method, the mixture of reagents with high melting point (higher than 1000 °C for typical inorganic compounds) is grinded, pelletized and subsequently heated to high temperature to proceed the chemical reaction. Since diffusion of the sample accelerates the reactions, temperature and reaction time play a crucial role to obtain a high purity sample. For example, repeating the steps of grinding, pelletizing, and annealing is effective to improve the sample quality.

Figure.2.1 (a) shows the process of a solid state reaction. In this reaction, starting materials of A and B are grinded to small particles as a and b. To proceed the reaction, particles a are required to move into material B area, adjacent to particles b, and react chemically. The movement of such particles is called diffusion, especially through solids, which is called solid-state diffusion. These two processes, *diffusion* and *reaction* are critical elements for a solid state reaction.

The solid-state diffusion length of particles a is described as $l \sim \sqrt{D_{\mathrm{a}} t}$ as shown in Fig.2.1 (b). Here, heating time t is proportional to l^2, thus a long reaction time is required to obtain a sufficient diffusion length. In general, possible solid-state diffusion paths include (i) through gaps in the crystal, (ii) through defects in the crystal, and (iii) through the grain surface. The larger the mobility of particles (atoms or ions), the greater the diffusion coefficient $D_{\mathrm{a(b)}}$. Furthermore, the diffusion coefficient is thermally activated as in $D = D_0 \exp(\Delta H / kT)$.

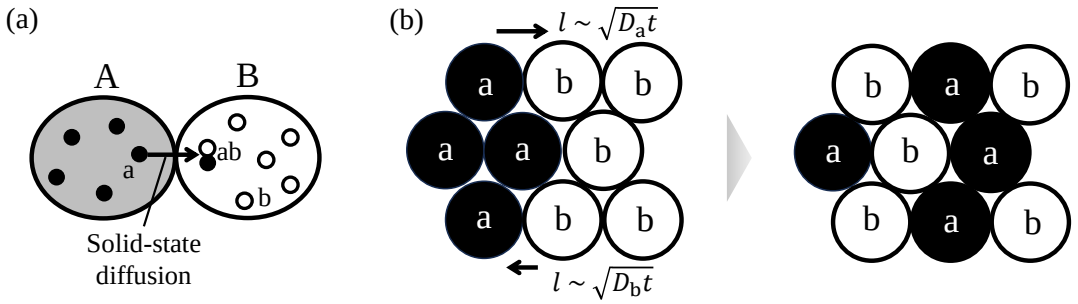

Figure 2.1: The process of a solid state reaction. (a) More than two inorganic chemicals are diffused and reacted, respectively. (b) The solid-state diffusion length increases in proportion to the square root of the heating time.

2.1.2 Flux method

Flux is a substance added to a material to lower the melting point. Single crystals can be obtained by transferring a mixture of the target compounds and flux in a crucible, raising the temperature to dissolve the target compounds to the melted flux, and then slowly cooling for recrystallization. Since the quality and size of the single crystal strongly depends on the type and ratio of starting compounds (flux) and heating process, optimization of each condition is required to obtain good crystals. Incidentally, when the flux is the same as the element in the target material, it is called the self-flux method.

The flux method has the advantages of (i) growing high-quality single crystals and (ii) growing crystals at temperatures lower than the melting point of starting materials. On the other hand, there are disadvantages such as a long time required for crystal growth. However, the flux method can overcome these disadvantages by combining with other synthesis methods. For example, by using the Bridgman furnace, in which the inside of the furnace moves vertically, efficient crystal growth can be achieved using a temperature gradient as shown in Fig.2.2. In addition, combining with the high-pressure method described below is expected to significantly shorten the crystal-growth time.

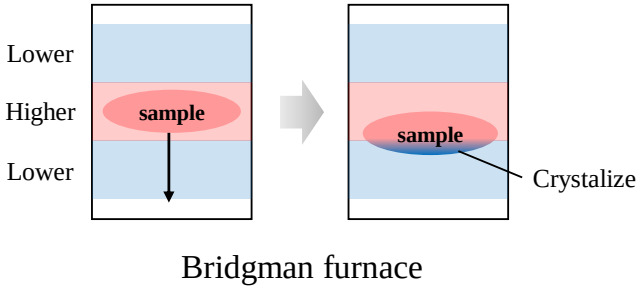

Figure 2.2: The schematics of a Bridgman furnace. Higher and lower temperature part corresponds to red and blue region, respectively.

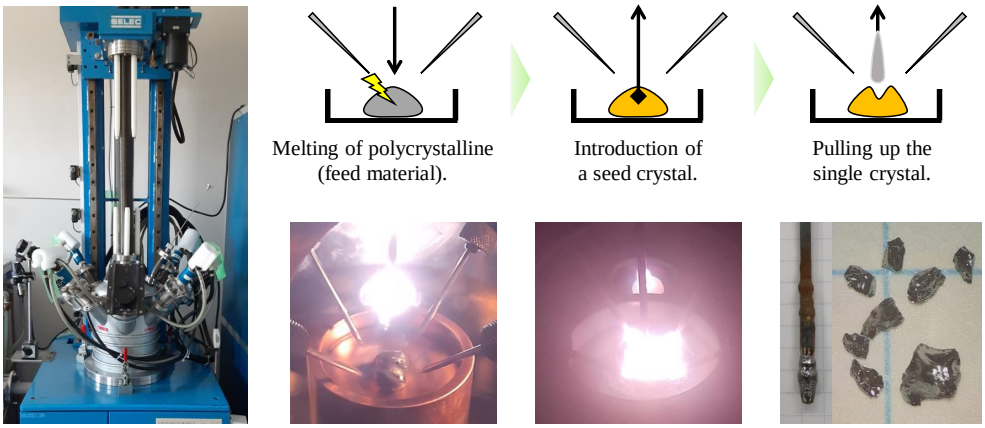

Figure 2.3: The photo and schematics of CZ method. The discharges from four directions can uniformly melt the polycrystalline (feed material). Single crystals can be obtained by crushing the pulled sample rod as depicted in the right photo.

2.1.3 Czochralski (CZ) method

The Czochralski (CZ) method grows large bulk single crystals by pulling the melted polycrystalline compounds upward under a temperature gradient as shown in Fig.2.3. To melt a feed material, arc discharge or high frequency induction is used as the heating method. The former can apply to the crystal growth for various types of intermetallic compounds using a tetra arc furnace equipped with multiple discharge needles. On the other hand, the latter can grow crystals from a large amount of feed materials in a crucible, being applied as a basic production method for a single crystal of silicon and other materials.

To obtain high-quality crystals in the CZ method, optimization of growth conditions such as temperature distribution in the furnace, gas flow, temperature gradient near the solid-liquid interface, crystal pulling and rotation speed, and necking are required. In addition, since an uniform composition distribution in crystals is necessarily to improve a homogeneity of crystals, a congruent growth is generally employed in which a composition matches between the solid and liquid phases. The CZ method is a potent method for a single crystal growth in intermetallic compounds, whereas is challenging and profound due to the many parameters involved in synthesis.

2.1.4 Floating zone (FZ) method

The FZ method produces single crystals by slowly cooling the molten polycrystalline rods (seed rod and feed rod) as shown in Fig.2.4 (a). In this method, a grounded part of both rods are heated and melted using halogen lamp light focused by ellipsoidal mirrors. The solvent is supported by surface tension and moved slowly downward without sagging. Finally, as the molten section is slowly cooled, crystals gradually precipitate on the seed rod. The crystal growth condition can be optimized by controlling the speed of rod movement, rotation and gas flow. Especially, necking is an important technique to reduce the number of crystals and to grow larger sizes. Unlike the CZ method, FZ method does not come in contact with foreign substances, thus

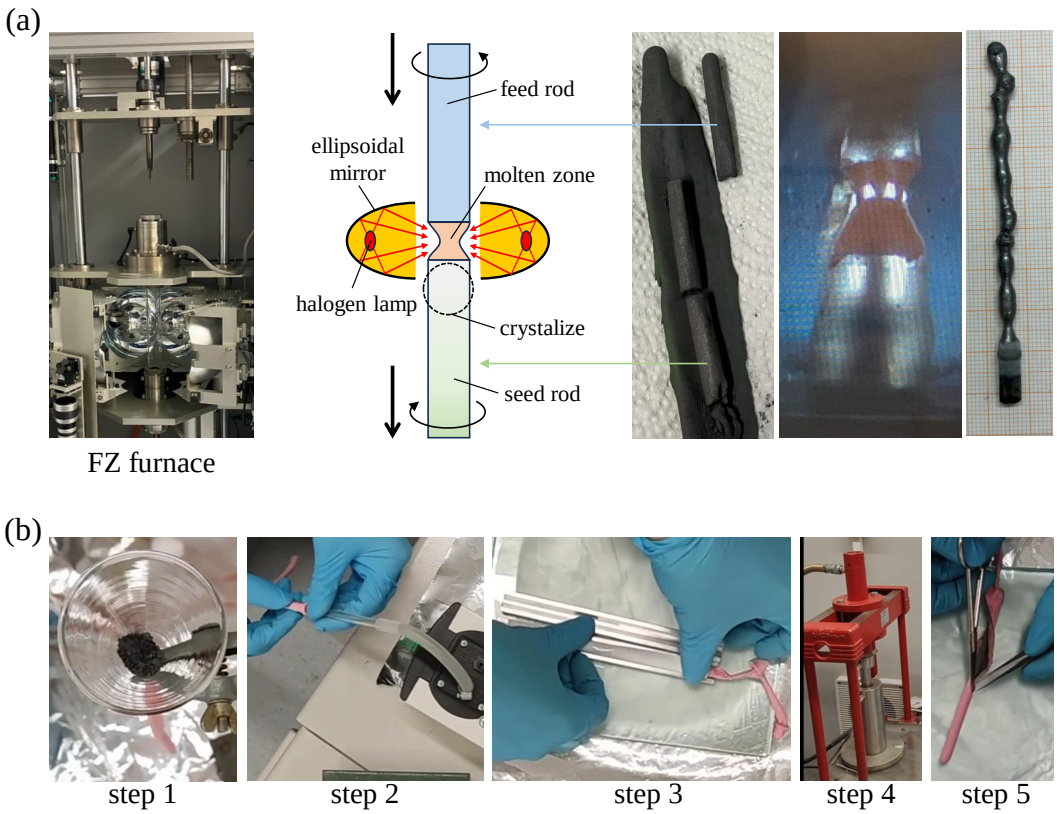

Figure 2.4: (a) The photo and schematics of FZ method. The focused light from a halogen lamps locally heat the grounded part of a seed rod and a feed rod to melt the sample and proceed crystal growth. (b) The preparation steps of sample rods.

producing high-purity single crystals. On the other hand, the instability of the solvent under the influence of gravity makes it difficult to grow large single crystals.

Although the FZ method is highly suitable for growing single crystals, the preparation is difficult because sample rods are soft and brittle. Figure 2.4 (b) shows the preparation steps of both rods. The following describes each step in detail.

step 1: Grind the mixture of regents (or pre-reacted compounds) elaborately, and then transfer it to rubber tube using a funnel. The rubber tube should be wiped with ethanol, as powder may adhere to the inner surface.

step 2: Put cotton into the rubber tube and it is evacuated using a diaphragm pump. The cotton prevents the grinded powder from sucked into the pump. Also, rub the rubber tube lightly to avoid remaining air.

step 3: After sufficient evacuation is achieved, tie off the end of the rubber tube and set it in aluminum tools, followed by fixing with tape.

step 4: Press into rod shape at around 700 bar using a hydrostatic press.

step 5: Using tweezers and scissors, carefully open the rubber tube and remove a sample rod. The rod is divided into two pieces for a seed rod and a feed rod and subsequently set in the FZ furnace. At this time, the rods can be annealed and sintered to make them denser.

2.1.5 High pressure method

The diffusion is one of the most important factor for solid state reaction as discussed in the previous section. Under high pressure, the particles are more likely to come into contact with each other and diffusion is accelerated, thus synthesis proceeds rapidly and is generally completed in a few hours. High-pressure synthesis is also the most impactive methods in the development of new compounds, because products with metastable denser structures at high temperatures can be obtained at room temperature by rapidly cooling. On the other hand, unstable compounds may be produced under ambient pressure, making it difficult to evaluate physical properties.

My affiliation, NIMS is one of the world's leading institute in high-pressure synthesis technology, and some call it the Mecca of high-pressure synthesis. In NIMS, there are several types of high-pressure synthesis apparatus such as multi type, belt type, etc as shown in Fig.2.5 (a). Multi-anvil type apparatus, mainly used in my synthesis, can apply cubic stable pressure of 1.5-6.0 GPa repeatably using cemented carbide (WC-Co) anvils. Figure 2.5 (b) displays schematics of the high-pressure synthesis method. The sample is heated by flowing a high current through anvils to a carbon heater, and temperature is monitored by incorporating thermocouples inside a pyrophyllite cell. In general, the sample is encapsulated within an outer capsule made of Au, Pt, and Ta, while intermetallic compounds are synthesized without a capsule, or using an inner capsule of BN to prevent the sample from reacting with the outer capsule.

The high-pressure synthesis, impactive and convenient method, has the disadvantage of making it difficult to start up the high-pressure apparatus. The Walker-type one, on the other hand, overcomes the disadvantage by separating the sample space from the press By using a mobile pot as shown in right panel of Fig.2.5 (a), high-pressure synthesis can be performed anywhere a press is available. However, for practical use, the synthesis system needs to be set up with pressure and temperature calibrations, which requires preeminent expertise. The Walker-type apparatus in the photo belongs to Prof. Takagi group in Max Planck Institute for Solid State Research (MPI-KFK), and was set up by Dr. Isobe with his colleges in MPI-KFK.

2.2 X-ray technique

X-ray is a electromagnetic waves with wavelengths of about 1 pm - 10 nm, which is sometimes called Röntgen ray after Wilhelm Röntgen discovered it in 1895. It is both an electromagnetic wave and a type of radiation, and its name comes from "X," a mathematical "unknown number," as named by Röntgen.

2.2.1 Bragg's law

Two types of x-ray, continuous and characteristic x-ray are generated using bremsstrahlung and fluorescence, respectively, by accelerated electron colliding with the target. The former has the property of white light with a continuous distribution of wavelengths, while the latter has the property of monochromatic light that is observed as sharp peaks on the spectrum and has a large

(a)

Multi type HP

Belt type HP

Walker type HP (MPI)

(b)

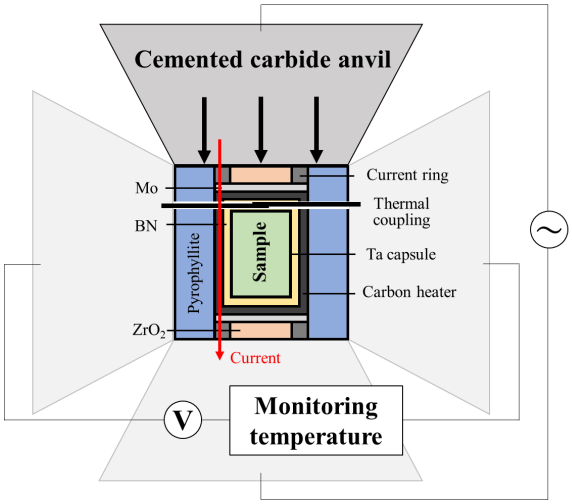

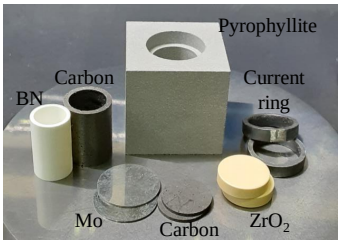

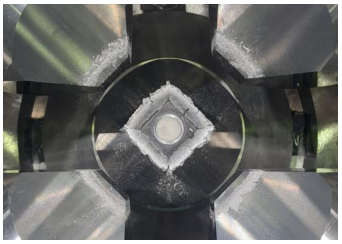

Figure 2.5: (a) Several types of high pressure apparatus. They has their own advantages, and different compounds can be synthesized despite the same pressure applied. (b) The schematics of the high-pressure synthesis method. (c) The photos of various tools used in high pressure synthesis. A pyrophyllite cell collapses after applying pressure.

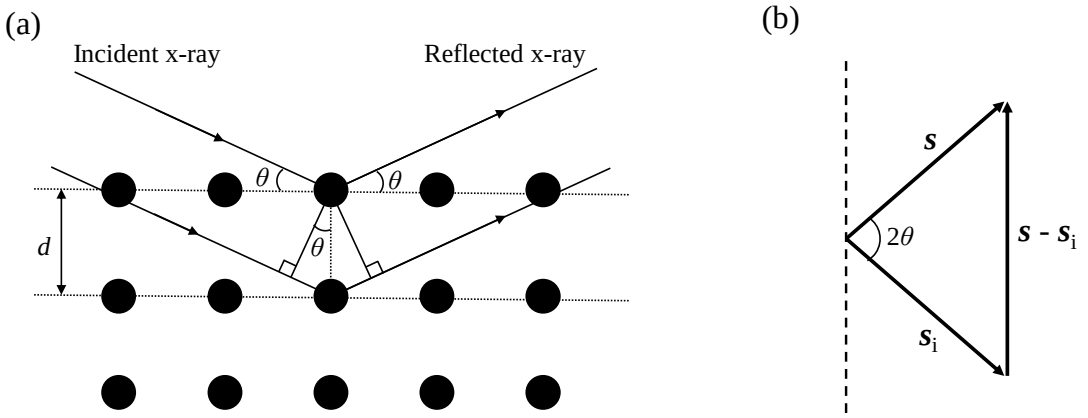

Figure 2.6: (a) The photo and schematics of FZ method. The focused light from a halogen lamps locally heat the grounded part of a seed rod and a feed rod to melt the sample and proceed crystal growth. (b) The preparation steps of sample rods.

intensity at a specific wavelength. The wavelength of characteristic x-ray depends on metals used as the target (Cu, Mo, Ag, Co, Fe, W, etc.). In general, wave diffraction and interference, observed by incident waves with wavelengths comparable to the distance of the grating pitch is applicable to studying periodic structure of materials. Therefore, the x-ray is employed to determine the crystal structure since the wavelength of x-ray corresponds to the distance of each elements in solids (a few Å). When x-rays enter to the reflecting surfaces separated by planes spacing d at an angle of θ, the scattered x-rays have an optical path difference of $2d\sin\theta$ as shown in Fig.2.6 (a). If the difference is a multiple of the wavelength, the scattered x-rays are enhanced by interference and a large reflection is expected. This system is called Bragg's law and described as

$$2d\sin\theta = n\lambda. \tag{2.1}$$

Next, let us consider the Bragg's law on a reciprocal space. The reciprocal space is represented by three independent basis reciprocal vectors $\boldsymbol{b}_1$, $\boldsymbol{b}_2$, and $\boldsymbol{b}_3$ and is defined by

$$\boldsymbol{b}_1 = \frac{\boldsymbol{a}_2 \times \boldsymbol{a}_3}{V}, \tag{2.2}$$

$$\boldsymbol{b}_2 = \frac{\boldsymbol{a}_3 \times \boldsymbol{a}_1}{V}, \tag{2.3}$$

$$\boldsymbol{b}_3 = \frac{\boldsymbol{a}_1 \times \boldsymbol{a}_2}{V}, \tag{2.4}$$

$$V = \boldsymbol{a}_1 \cdot (\boldsymbol{a}_2 \times \boldsymbol{a}_3), \tag{2.5}$$

for three independent basis real vectors $\boldsymbol{a}_1$, $\boldsymbol{a}_2$, and $\boldsymbol{a}_3$. From these definition, the relationship between reciprocal vectors and real vectors is expressed as

$$\boldsymbol{a}_i \cdot \boldsymbol{b}_j = \delta_{ij}. \tag{2.6}$$

In general, reciprocal vectors are described as

$$\boldsymbol{G} = h\boldsymbol{b}_1 + k\boldsymbol{b}_2, + l\boldsymbol{b}_3, \tag{2.7}$$

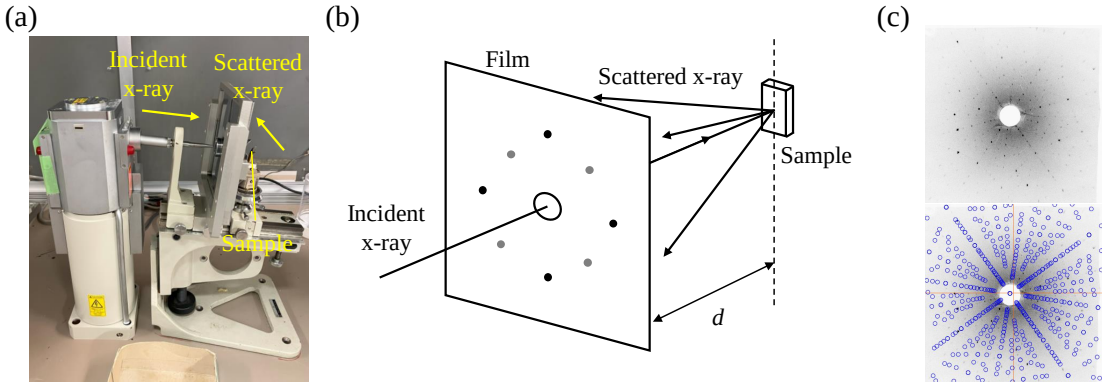

Figure 2.7: (a) The photo of Laue photograph apparatus. (b) The schematic of back-scattering Laue method. (c) Laue pattern and analysis process.

using the Miller index h, k, and l, whose direction is perpendicular to (hkl) planes, and length is equal to the reciprocal of spacing of (hkl) planes.

The x-rays incident on and reflected from a certain Miller plane are represented by an unit vector $\boldsymbol{s}_i$ and $\boldsymbol{s}$ as shown in Fig.2.6 (b). Then the scattering vector $\boldsymbol{s} - \boldsymbol{s}_i$ is perpendicular to the reflecting surface, i.e., the Miller plane (hkl), and its length is $2\sin\theta$. Here, the length of the reciprocal vector G is the reciprocal of spacing d of (hkl) planes, expressed as

$$|\boldsymbol{G}| = \frac{1}{d} = \frac{2\sin\theta}{\lambda} = \left|\frac{\boldsymbol{s} - \boldsymbol{s}_i}{\lambda}\right|. \tag{2.8}$$

Since both $\boldsymbol{G}$ and $\boldsymbol{s} - \boldsymbol{s}_i$ point the same direction along perpendicular to (hkl) planes, Eq.3.5 is transformed to

$$\boldsymbol{G} = \frac{\boldsymbol{s} - \boldsymbol{s}_i}{\lambda}. \tag{2.9}$$

As Eq.2.9 implies, the scattering vector is associated with the reciprocal vector.

2.2.2 Laue method

The Laue method is one of the most useful way to determine the crystal symmetry and axial directions by taking Laue photographs using continuous x-rays. Figure2.7 (a) and (b) shows the Laue photograph apparatus and its schematic, respectively. The continuous x-rays incident on a sample through a film are scattered on certain Miller planes, and detected on the film as Laue spots. Figure 2.7(b) shows the back-scattering Laue method, where the film is on the incident x-ray side, whereas the transmission Laue method is utilized for observing the scattered x-rays transmitted through the sample. The former can be applied for various samples, and the latter is suitable for measuring high transmission or thin samples. Also common to both, the scattering intensity can be improved by polishing the sample surface. The crystal symmetry and axial directions of samples can be determined by checking the correspondence between Laue spots and Miller plane reflection from the obtained Laue photograph, as shown in Fig.2.7 (c). Although one analysis method is to use a Greninger/Leonhardt chart, recently more convenient free analysis software (X-ray Laue Backscattering Pattern Simulator) is widely used [Fig.2.7 (c) bottom photo].

Table 2.1: Relationships between interplanar spacing, lattice constant, and Miller indices for each crystal system.

Monoclinic	$\frac{1}{d^2} = \frac{1}{\sin^2\beta}\left(\frac{h^2}{a^2} + \frac{k^2\sin^2\beta}{b^2} + \frac{l^2}{c^2} - \frac{2hl\cos\beta}{ac}\right)$
Orthorhombic	$\frac{1}{d^2} = \frac{h^2}{a^2} + \frac{k^2}{b^2} + \frac{l^2}{c^2}$
Tetragonal	$\frac{1}{d^2} = \frac{h^2+k^2}{a^2} + \frac{l^2}{c^2}$
Cubic	$\frac{1}{d^2} = \frac{h^2+k^2+l^2}{a^2}$
Hexagonal	$\frac{1}{d^2} = \frac{4}{3}\left(\frac{h^2+hk+k^2}{a^2} + \frac{l^2}{c^2}\right)$

2.2.3 Diffractometer method

In the diffractometer method, characteristic x-rays are adopted to study crystal structure of powder samples. Figure 2.8 (a) and (b) display a Powder x-ray diffraction (PXRD) machine, MiniFlex (Rigaku), and a schematic of diffractometer method, respectively. The diffraction process is shown as following. At first, the incident x-rays pass through a solar slit (S1) and a divergent slit (DS) to extract parallel components of x-rays and narrow them down. Then, the x-rays enter to the sample and are scatted, followed by passing through a scattering slit (SS), solar slit (S2), and receiving slit (RS) to exclude the secondary diffraction and unnecessary components. Finally, the extracted scattered x-rays are detected. During the PXRD measurements, the sample rotates on a goniometer and a detector revolves around a center of the goniometer while satisfying the Bragg's law. In other words, when the sample rotatesθ, the detector revolves 2θ.

Since a x-ray wavelength λ is given in the diffractometer method, the spacing of the Miller plane, $d = \lambda/\sin\theta$, where the Bragg reflection occurs is obtained by observing the Bragg peaks and its angle θ. Here, d is associated to a lattice constant via Miller indices, as shown in Table 2.1. Therefore, the lattice constant is calculated by determining the Miller indices corresponding to each Bragg peak. For example, in the case of a cubic system, the Bragg angle is expressed using the Miller indices as

$$\sin\theta = \frac{\lambda}{2d} = \frac{\lambda\sqrt{h^2+k^2+l^2}}{2a}. \tag{2.10}$$

From Eq.2.10, the Bragg peak appears at the smallest angle when $h^2 + k^2 + l^2$ has the smallest value.

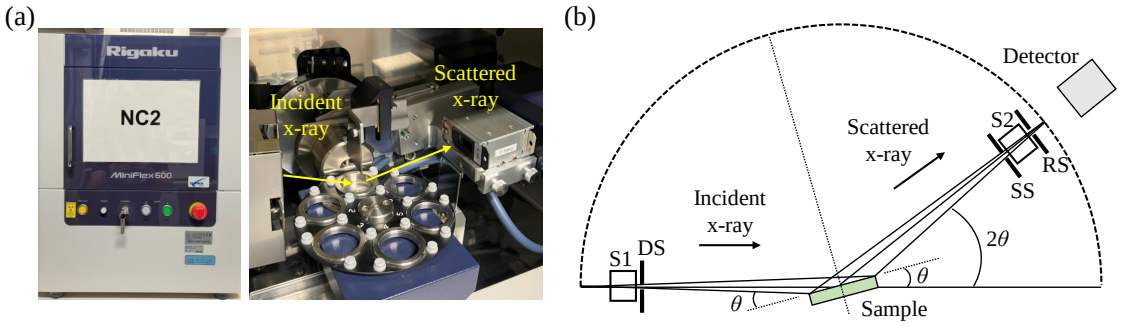

Figure 2.8: (a) The photos of a PXRD machine, MiniFlex, and its inside view. (b) The schematics of diffractometer method.

2.3 Physical property measurements

To determine the chemical and physical properties and performance changes of synthesized samples, various measurements are carried out as following.

2.3.1 Magnetic measurements

Magnetic measurements are performed by a pull-put method using a SQUID magnetometer MPMS3 (Quantum Design, Inc.) as depicted in Fig.2.9 (a). In this method, when a magnetized sample is passed through a single-turn pickup coil as shown in Fig.2.9 (b), the spatial distribution of the magnetic flux Φ along z-axis direction generated around the pickup coil is described as

$$\Phi(z) = -\frac{\mu_z}{2}\left[\frac{z^2}{(R^2+z^2)^{3/2}} - \frac{1}{(R^2+z^2)^{1/2}}\right]. \tag{2.11}$$

Simultaneously, an induced electromotive force is generated in the coil, transferred via the flux transformer to the SQUID (Superconducting Quantum Interference Devise), and then output as a voltage

$$V(z) = C\Phi(z) = -\frac{C\mu_z}{2}\left[\frac{z^2}{(R^2+z^2)^{3/2}} - \frac{1}{(R^2+z^2)^{1/2}}\right], \tag{2.12}$$

proportional to the magnetic flux. Here, C is the calibration factor depending on the device. By subjecting the acquired voltage so called a SQUID curve to fitting to Eq.(2.11), the exact value of magnetization can be obtained. The MPMS utilizes a second-derivative coil combined with a single-turn pickup coil to remove the effects of spatially uniform magnetic fields, such as geomagnetism and fluctuations in the applied magnetic field, as magnetic noise. Figure 2.9 (c) displays schematics of a second-derivative coil and a waveform of SQUID curve obtained by the second-derivative coil.

The measurement requires the preparation of a straw to be inserted inside the chamber of the MPMS. Generally, for powder samples, the sample is wrapped in plastic film, inserted into the straw, and then fixed within the straw. For single crystal samples, use a quartz rod instead of a straw to fix the sample with varnish. The MPMS3 in Fig.2.9 (a) has a measurement temperature range of 1.8 to 350 K (350 to 1000 K: using oven mode) and a magnetic field range of -7 to 7 T.

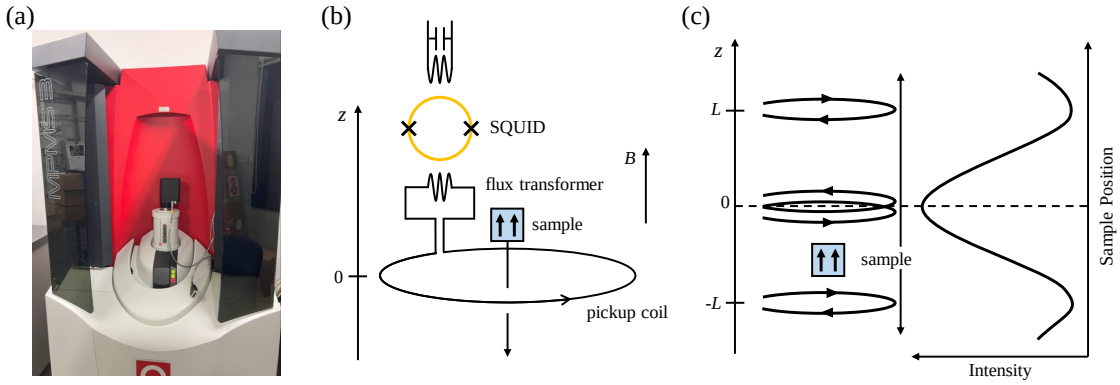

Figure 2.9: (a) A photo of MPMS3. (b) The schematics of pull-out method and a single-turn pickup coil. The process where a magnetized sample passes through the pickup coil and is detected as a signal through the SQUID is represented. (c) The second-derivative coil and a waveform of SQUID curve obtained by the second-derivative coil.

2.3.2 Heat capacity measurements

Heat capacity measurements are carried out by a relaxation method using a PPMS (Quantum Design Inc.) as depicted in Fig.2.10 (a). In the relaxation method, first of all, consider the case in Fig.2.10 (b) where the sample, sample stage, and the heat bath with $T = T_0$ are in contact through a material with thermal conductivity of κ. Here, the sample and sample stage are regarded as one unit due to a good thermal contact each other. When the temperature on the sample side is increased to T_s by slightly heating with a heater, and wait enough until settle into equilibrium state, heat conduction equation is expressed as

$$C\frac{dT_s(t)}{dt} = -\kappa(T_s(t) - T_0) + W, \tag{2.13}$$

where C represents the heat capacity of a sample and a sample stage. Then, the heater is turned off again from the equilibrium state ($W = 0$), and the sample side temperature (T_s) relaxes to the heat bath side temperature (T_0) as shown in Fig.2.10 (c)). The temperature variation during the relaxation process, the sample temperature T_s is given as

$$T_s(t) = T_0 + (T_s - T_0)\exp\left(\frac{\kappa}{C}t\right), \tag{2.14}$$

by solving the heat conduction equation using the initial condition $T = T_s(0)$ at $t = 0$. In this way, the relaxation constant ($\tau = C/\kappa$) can be determined from the measurements, and the heat capacity of the sample and sample stage is acquired from the value of thermal conductivity κ.

Typically, in the heat capacity measurements, APIEZON N (H), a grease with high thermal conductivity, is used to fix the sample on the stage. When fixing the sample to the stage, the wire is very easy to break, therefore the pack is set on a special tool as displayed in Fig.2.10 (b) and a diaphragm pump is used to hold the stage. In addition, a sample heat capacity is obtained by subtracting one of sample stage, heater, and thermometer (addenda measurements) from the total one. The PPMS in Fig.2.10 (a) has a measurement temperature range of 1.8 to 350 K and a magnetic field range of −9 to 9 T.

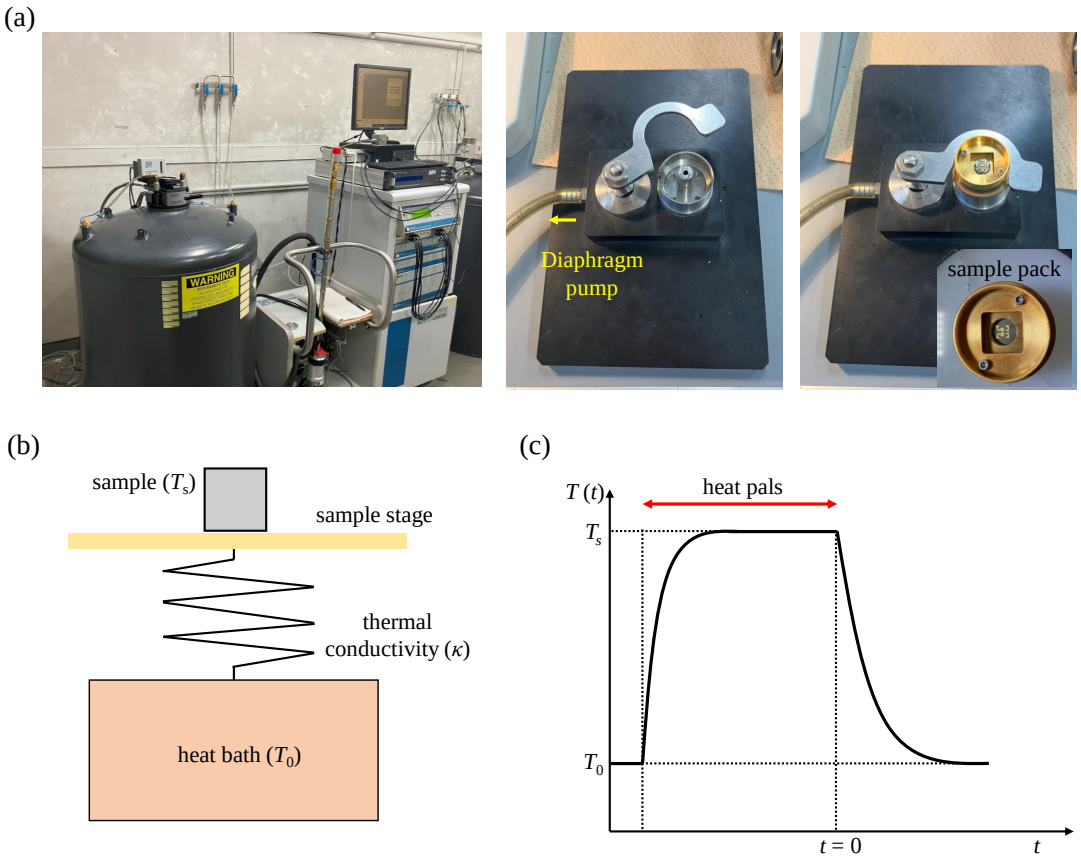

Figure 2.10: (a) A photo of PPMS and sample pack for heat capacity measurements. Set a sample on the stage while fixing the stage with a diaphragm pump. (b) The system in the sample pack. (c) The time dependence of system temperature.

2.3.3 Electrical resistivity measurements

Longitudinal resistivity (ρ_{xx}) and Hall resistivity (ρ_{yx}) were measured using a four-prove technique in transport option of a PPMS. The four-prove method consists of current and voltage terminals, and the former (I_+, I_-) and latter (V_+, V_-) are contacted with a sample as shown in the Fig.2.11 (a). Although current is applied to the sample, almost no current flows to the voltage terminal side due to the high input impedance of the voltmeter. Therefore, the sample resistance can be accurately measured without lead wire resistance and contact resistance. In addition, the row voltage data includes a thermal electromotive force V_T generated by the temperature gradient of the sample and an offset voltage V_0 of the measurement system. To remove these contributions, the data should be measured while reversing the current, such as

$$V_+ = RI + V_T + V_0, \tag{2.15}$$

$$V_- = -RI + V_T + V_0, \tag{2.16}$$

for the forward current flow and the reverse current flow, respectively. By dividing the difference between the two obtained by the applied current value, the electrical resistance R is calculated to

with V_+ as the voltage when the current is applied in the forward direction and V_- as the voltage when the current is applied in the reverse direction. Dividing the difference of these voltage values by the applied current value, the electrical resistance R is calculated to be

$$R = \frac{V_+ - V_-}{2I}. \tag{2.17}$$

Under a magnetic field, the itinerant electrons responsible for conductivity are exposed to the Lorentz force $q(\boldsymbol{v} \times \boldsymbol{B})$, leading a Hall voltage perpendicular to the direction of current flow. Such a Hall effect, which is proportional to the magnetic field, is called a normal Hall effect. On the other hand, that caused by the magnetization M of the sample and that caused by the topological properties of topological insulators and skyrmions are called abnormal Hall effect and topological Hall effect, respectively. These are observed in the Hall resistivity measurement as the total Hall resistance described as

$$R_H = R_0 + R_A + R_T, \tag{2.18}$$

where R_H, R_0, R_A, and R_T are the Hall coefficients of the observed Hall resistance, normal Hall effect, anomalous Hall effect, and topological Hall effect, respectively. They can be classified into their respective components by measuring the the magnetic field dependence of longitudinal resistance and magnetization.

In the resistivity measurements, Au wires are reinforced with silver paste for electrical contacts on the sample as displayed in Fig.2.11 (b). To eliminate mixing of ρ_{xx} and ρ_{yx}, the magnetic field dependence measurements are carried out in positive and negative fields, and experimental signals ρ_{xx}^{exp} and ρ_{yx}^{exp} are symmetrized and antisymmetrized to obtain true ρ_{xx} and ρ_{yx}, respectively, as following equations

$$\rho_{xx}(H) = \frac{\rho_{xx}^{exp}(H) + \rho_{xx}^{exp}(-H)}{2}, \tag{2.19}$$

$$\rho_{yx}(H) = \frac{\rho_{yx}^{exp}(H) - \rho_{yx}^{exp}(-H)}{2}. \tag{2.20}$$

The temperature and magnetic field ranges that can be measured are the same as for heat capacity measurements.

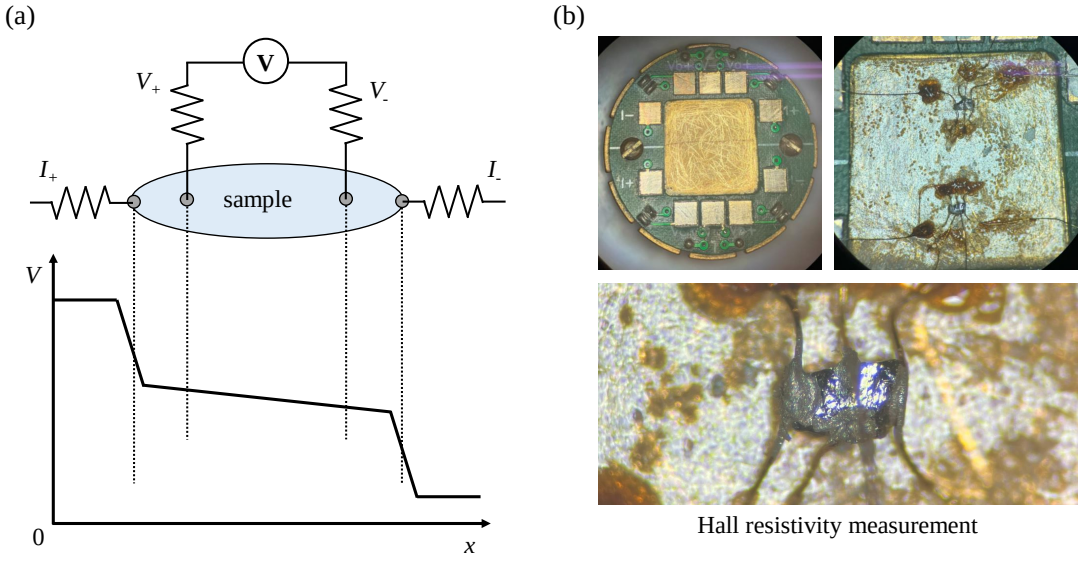

Figure 2.11: (a) The schematics of four-prove resistivity measurements. When measuring Hall resistivity, the voltage terminal should be perpendicular to the current. (b) The photos of sample pack for AC transport option and a sample preparation. The samples are fixed on the pack using tape and vanish.

Chapter 3

Crystal growth of centrosymmetric skyrmion magnets

In this chapter, I summarize the crystal growth of Gd-based intermetallic compounds, synthesis of new materials, and their physical properties as a good candidate of centrosymmetric skyrmion compounds. Recently, starting with Gd_2PdSi_3, a number of centrosymmetric skyrmion compounds have been reported. On the other hand, there are only a few examples of actual materials, and there is still potential for more experimental verification and discussion of changes in the physical properties of each compound. I have been working on material synthesis and physical property measurements with the aim of 1) development of new materials and 2) clarifying the effects of substitution effects on the magnetic phase diagram and Hall resistivity through elemental substitutions of previous compounds Gd_2PdSi_3 and $GdRu_2Si_2$. The magnetism of these skyrmion compounds is attributed to the RRKY interaction of Gd ions, and this RRKY interaction varies depending on the distance between two Gd ions. Therefore, changes in the distance between ions due to elemental substitutions are expected to affect the electrical conductivity associated with magnetism and magnetic structure. Here, as an example, the relationship between the RKKY interaction and the distance of each Gd ion in $Gd_3Os_4Al_{12}$ is shown in Fig.3.1. This result can be estimated in a simplified manner from

$$\mathcal{H}_{\mathrm{RKKY}} = -9\pi \frac{J^2}{\epsilon_F} \left(\frac{N_e}{N} \right)^2 S(r) \boldsymbol{S_1} \cdot \boldsymbol{S_2}, \tag{3.1}$$

$$S(r) = \left[-\frac{\cos(2k_F r)}{r^3} + \frac{\sin(2k_F r)}{r^4} \right], \tag{3.2}$$

where $k_F = 3.5888\mathrm{nm}^{-1}$ is Fermi wavenumber. Futhermore, the RKKY interaction is induced by the hybridization of localized spins and itinerant electrons, and is therefore responsive to a band structure near the Fermi surface. In Gd_2PdSi_3 and $GdRu_2Si_2$, the $4d$ orbitals of Pd and Ru contribute significantly to the electrical conductivity. Thus, RKKY interaction can be controlled through a change in the band structure by substituting these elements with $3d$ or $5d$ elements. Based on this background, in this study, I have focused on elemental substitution except Gd cite which is responsible for magnetism.

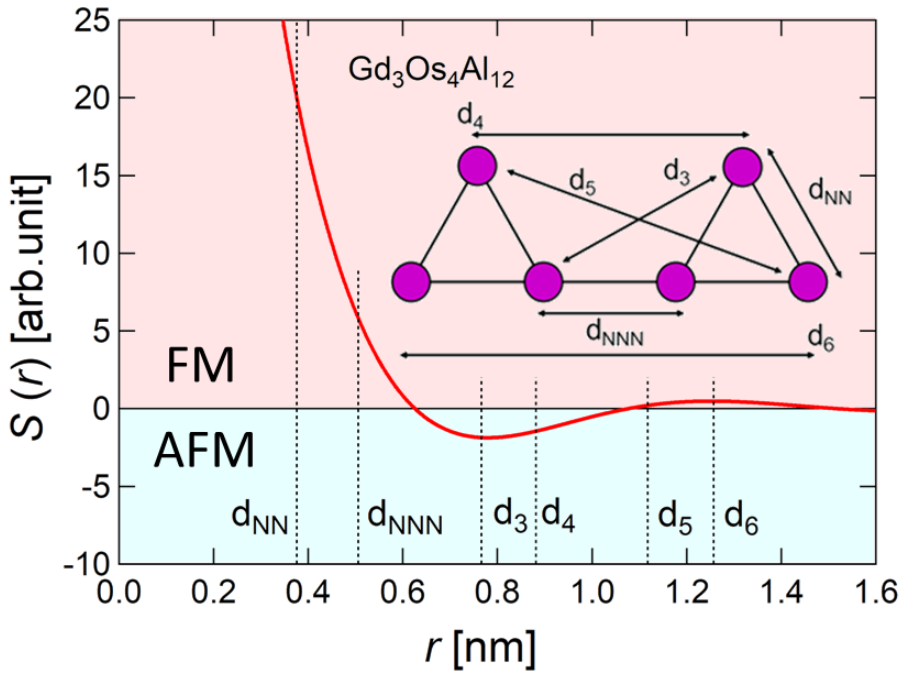

Figure 3.1: The calculated RKKY interaction as a function of distance of two Gd ions.

3.1 Exploring the magnetic phase diagram and unusual Hall resistivity suppression in centrosymmetric $GdOs_2Si_2$ single crystal

In this section, I focus on $GdOs_2Si_2$ [60, 82], an osmium-substituted variant of $GdRu_2Si_2$. While the magnetic properties of $GdOs_2Si_2$ remain unresolved, it shares the centrosymmetry and layered structure stacking along the c-axis with $GdRu_2Si_2$. Given slight variations in lattice constants and energy levels in the $4d$ and $5d$ electron bands between $GdOs_2Si_2$ and $GdRu_2Si_2$, one can reasonably anticipate differences in the nature of the Gd-spin interaction in these two compounds. Consequently, the magnetic phase diagram of $GdOs_2Si_2$ may also exhibit some alterations. I have meticulously summarized my measurements of $GdOs_2Si_2$ single crystals, including electrical resistivity, magnetization, and specific heat capacity. These results were compiled into a temperature-field phase diagram and juxtaposed with the phase diagram obtained for $GdRu_2Si_2$. The results show that there is a new magnetic phase in $GdOs_2Si_2$, which has not been observed before, and that the Hall resistivity is significantly suppressed there.

3.1.1 Experimental

A single crystal was grown by the Czochralski (CZ) method using a tetra-arc furnace from a mixture of Gd, Os, and Si metals with a stoichiometric composition under an Ar atmosphere of approximately 75 kPa. Although I expect single crystals can be grown by the floating zone method as well, the Os-based evaporation products generated during the crystal growth process are toxic. Therefore, the CZ method (tetra-arc furnace) was used this time to confine them. The ingot containing the crystal was annealed at 900 ° C for one week to improve its homogeneity

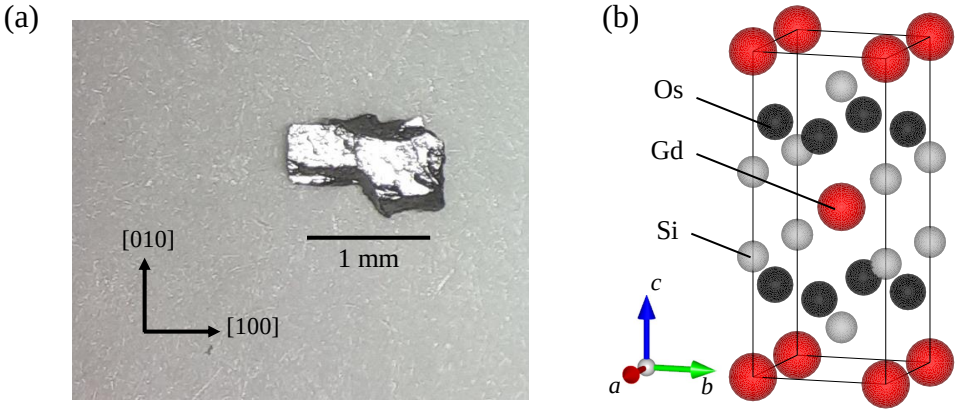

Figure 3.2: (a) A single crystal of $GdOs_2Si_2$. The arrows show the directions of the crystallographic axes and the bar indicates the 1 mm scale. (b) Crystal structure of $GdOs_2Si_2$. The line-drawing box illustrates the tetragonal unit cell.

and relieve possible structural distortions. The crystal separated from the ingot [Fig.3.2 (a)] was confirmed to be $GdOs_2Si_2$ with a $ThCr_2Si_2$-type structure with body-centered tetragonal symmetry ($I4/mmm$, #139), using Laue X-ray diffraction. The crystal axes were determined using the same Laue method. The lattice constants were a = 4.1549(2) Åand c = 9.8117(8) Å, which were slightly shorter and considerably longer than those of $GdRu_2Si_2$ [a = 4.164(2) Å, c = 9.616(5) Å] [60], respectively.

I conducted measurements of magnetic, thermal, and transport properties across a temperature range spanning from 2 K to 300 K, as well as varying magnetic fields (H), utilizing a single crystal sample. Initially, a slender plate-shaped crystal with approximate dimensions of 1.1 mm × 0.50 mm × 0.23 mm was chosen for the study. Additionally, to explore sample dependence, another crystal underwent similar investigations. A SQUID magnetometer, specifically the MPMS3 model from Quantum Design Inc., was utilized to collect magnetic data. The temperature-dependent magnetization (M) was recorded under field cooling conditions, and the magnetic susceptibility was calculated as $\chi = M/H$. To determine the specific heat capacity (C_p), the heat relaxation method was employed, with a magnetic field applied parallel to the c-axis. This measurement setup employed a commercially available system, specifically the PPMS model from Quantum Design Inc.

For the assessment of longitudinal resistivity (ρ_{xx}) and Hall resistivity (ρ_{yx}) (equal to $-\rho_{yx}$), a magnetic field parallel to the c-axis was applied using the transport option of the PPMS system. To secure the gold wires onto the crystal, silver paste was utilized, with the distance between the voltage terminals of the crystal set at 0.35 mm for ρ_{xx} and 0.38 mm for ρ_{yx} (for the first crystal). Throughout these measurements, an excitation current of 20 mA was passed along the crystal's [100] direction.

3.1.2 Results and discussion

Figure 3.3 displays the χ-T curves for $\mu_0 H$ = 1 T with $\mu_0 H$//[100], [110], and [001]. Each curve exhibits Curie-Weiss behavior at high temperatures, and a clear peak at T_1 = 26.6 K

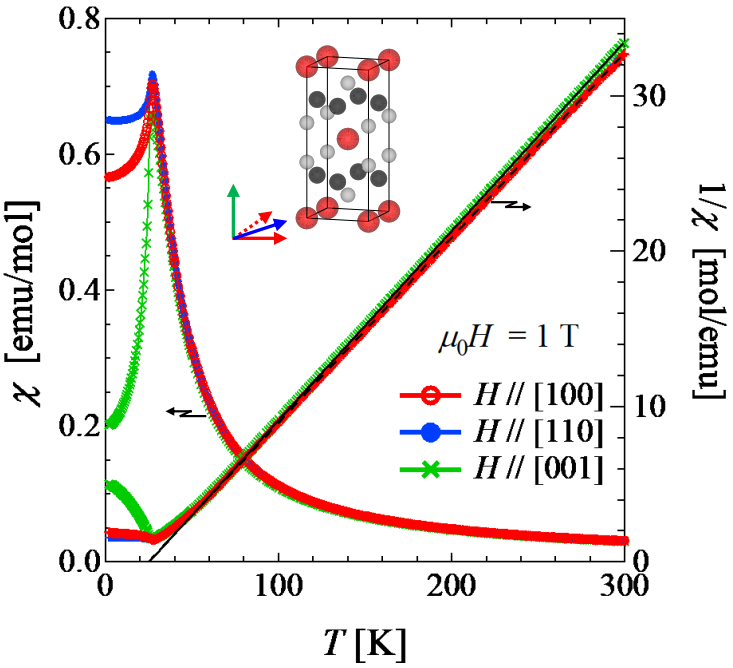

Figure 3.3: Temperature dependence of magnetic susceptibility under a magnetic field of 1 T along [100], [110], and [001]. The solid black line represents the Curie-Weiss fitting. The inset shows the crystal structure of $GdOs_2Si_2$. All measurements were carried out using the single crystal shown in this photograph.

indicates the antiferromagnetic ordering of the Gd^{3+} ions. The Curie constant C and Weiss temperature θ_W were estimated from the linear temperature dependence of the inverse magnetic susceptibility above 100 K. For $\mu_0 H$//[100] and $\mu_0 H$//[110], C was determined to be 8.39 emu K mol^{-1} and θ_{rmW} to be +25.0 K, while for $\mu_0 H$//[001], C was found to be 8.20 emu K mol^{-1} and θ_W to be +25.5 K. The calculated effective magnetic moment from the Curie constant was 8.18 μ_B for $\mu_0 H$//[100] and [110], and 8.10 μ_B for $\mu_0 H$//[001], in agreement with the theoretical value of μ_{eff} = 7.94 μ_B for Gd^{3+} ions. These results suggest that the $4f$ electrons of Gd^{3+} ions are well localized, while the 5d electrons of Os ions behave as itinerant and Pauli paramagnetic. Similar behavior has been reported in $GdRu_2Si_2$ [62]. Despite the antiferromagnetic ordering, similar to $GdRu_2Si_2$ [83], the dominant interaction between Gd^{3+} ions is considered to be ferromagnetic because the Weiss temperature is positive. Additionally, the paramagnetic state is almost isotropic, but the magnetic susceptibility below T_1 is highly anisotropic, with the susceptibility for $\mu_0 H$//[001] significantly lower than that for $\mu_0 H$//[100] or [110]. This suggests that the Gd^{3+} moment is ordered along the c-axis, as observed in $GdRu_2Si_2$ [83].

Figure 3.4 illustrates the temperature dependence of χ curves (left) and their differentials $d\chi/dT$ curves (right) measured at various magnetic fields below 40 K. For the case of H//[001] as shown in Fig.3.4 (a), distinct features labeled as T_1 (arrow), T_2 (triangle), and T_3 (diamond) were observed at different temperatures, corresponding to the peak positions in the $d\chi/dT$ curves. While the change at T_1 seems relatively smaller compared to the more pronounced peak-like changes at T_2 and T_3 in the differential curves, it becomes evident from the data at $\mu_0 H$ = 2.4 T and 3 T that T_1 and T_2 are indeed clearly separated at elevated magnetic fields. T_2 displays a more pronounced decrease than T_1 as the magnetic field increases from 25 K (at $\mu_0 H$ = 1 T) to 6 K (at 3 T). Moreover, an anomaly emerges around 13 K at $\mu_0 H$ = 2 T (T_3), which fades as the magnetic field is further increased.

Regarding the situation where H//[100], a minimum of two distinct changes were identified, as portrayed in Fig.3.4 (b). Although the overall profile of alterations appears to display a more gradual and uniform trend, qualitatively similar associations with temperature and magnetic field can be observed. For the sake of convenience, I label the temperatures corresponding to these distinctive changes as T_4 and T_5.

The upper portion of Fig. 3.5 (a) illustrates the isothermal magnetization curve and its derivative curve obtained at 1.8 K while applying a magnetic field perpendicular to the crystal's c-plane (H//[001]). Within this depiction, the magnetization process demonstrates swift alterations at specific magnetic field strengths: $\mu_0 H_1$ = 2.5 T, $\mu_0 H_2$ = 2.8 T, and $\mu_0 H_3$ = 3.2 T, along with a gradual kink manifesting at $\mu_0 H_4$ = 6.5 T. These variations manifest more prominently within the differential curves. Notably, the transformations at H_1, H_2, and H_3 exhibit hysteresis in response to the magnetic field, underscoring their connection with first-order phase transitions. Conversely, the absence of noticeable hysteresis is evident at H_4, where the magnetization of Gd^{3+} ions achieves saturation at a value of 7 μ_B.

The outcomes of the measurements capturing magnetic transitions driven by varying temperatures and magnetic fields are presented in the lower section of Fig.3.5 (a). Notably, all transition fields designated as H_1, H_2, H_3, and H_4 shift towards lower magnetic field strengths as the temperature increases. Specifically, H_3 diminishes around 10 K, while H_1 either merges with H_2 or vanishes entirely around 20 K. As for H_4, it becomes progressively less distinguishable at elevated temperatures and is indiscernible beyond 20 K. This behavior can be attributed to the fact that, as elucidated later, the phase boundaries above 20 K align nearly perpendicular to the temperature axis.

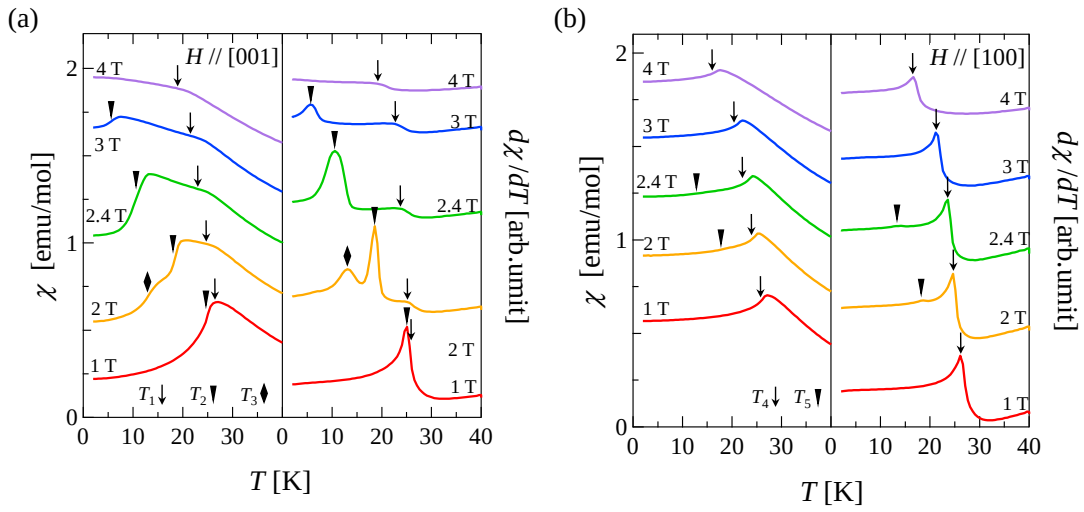

Figure 3.4: Temperature and field dependence of χ and its derivative (dχ/dT) for $GdOs_2Si_2$ measured with a magnetic field aligned along (a) [001] and (b) [100] directions. The arrows and different symbols denote characteristic magnetic transition temperatures: T_1, T_2, and T_3 for H//[001], and T_4 and T_5 for H//[100]. The data have been shifted for clarity.

At the upper section of Fig.3.5 (b), I present the M-H and dM/dH-H curves at 1.8 K, considering an external magnetic field aligned with H//[100]. When examining the H//[100] configuration, distinct anomalies are observed in the dM/dH curve at specific magnetic fields: $\mu_0 H_5$ = 1.1 T, $\mu_0 H_6$ = 2.5 T, $\mu_0 H_7$ = 5.7 T, and $\mu_0 H_8$ = 6.8 T. Notably, the anomaly at H_5 exhibits hysteresis. Moreover, a broader peak anomaly is noticeable in the dM/dH curve at H_6. In contrast, a well-defined peak manifests at H_7, positioned just slightly below the saturation field H_8. This peak's prominence increases with rising temperature, as illustrated in the lower portion of Fig.3.5 (b). With increasing temperature, these critical fields shift towards lower magnetic field values.

The phase diagram for H//[001] (left) and H//[100] (right) was established based on χ-T and M-H measurements, as illustrated in Fig.3.6. The diagram features notable points such as T_1, T_2, T_3, H_1, H_2, H_3, and H_4, along with T_4, T_5, H_5, H_6, H_7, and H_8. In the H//[001] phase diagram, it is evident that four distinct magnetic phases (I, II, II', and III) exist before reaching saturation, contingent upon temperature and magnetic field conditions. The overall structure of this phase diagram closely resembles that of $GdRu_2Si_2$ [84], except for the possible inclusion of the phase II'.

To better understand the magnetic structure, Hall resistivity measurements were performed, and the results are shown in Fig.3.7. Clear changes are observed at H_1, H_2, H_3, and H_4, indicating a robust interaction between the local moment of Gd^{3+} and the conduction electrons. The magnetic field dependence is similar to that of $GdRu_2Si_2$ [58], except for the phase II'. In particular, the sharp increase in ρ_{yx} observed in the phase II' closely resembles the topological Hall effect observed in the double-Q square skyrmion lattice state of $GdRu_2Si_2$.

On the other hand, ρ_{yx} just above H_2 converges to an extrapolated value obtained from the slope of ρ_{yx} in phase I. Consequently, the characteristic aspect of $GdOs_2Si_2$ is the II' phase, representing a magnetic state with an undisclosed spin configuration. Recent theoretical studies

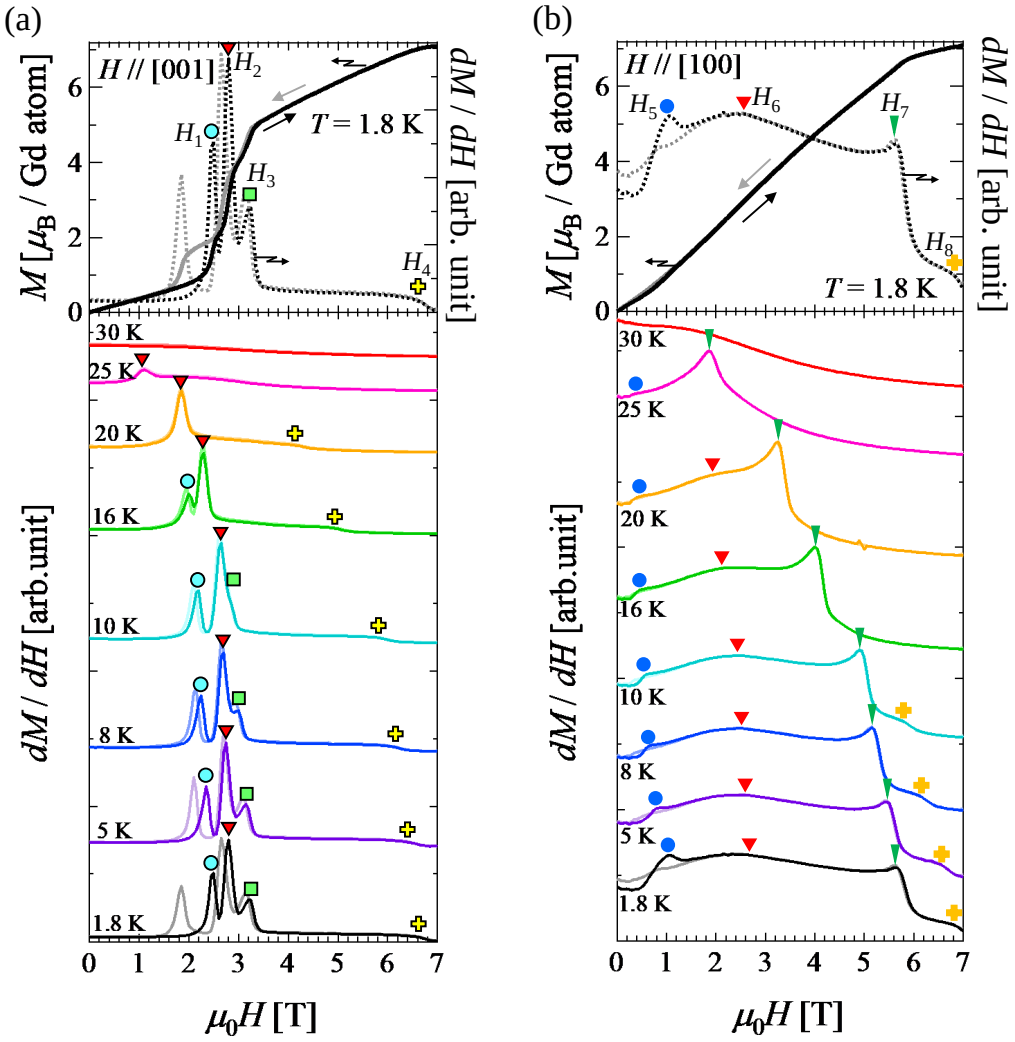

Figure 3.5: Isothermal magnetization curve (left axis) and its derivative dM/dH (right axis) measured at 1.8 K, with increasing and decreasing magnetic fields up to 7 T applied (a) parallel to [001] and (b) parallel to [100]. The symbols represent critical fields: H_1, H_2, H_3, and H_4 for H//[001] and H_5, H_6, H_7, and H_8 for H//[100]. The thermal evolution of dM/dH is shown at the bottom. The data have been shifted for clarity.

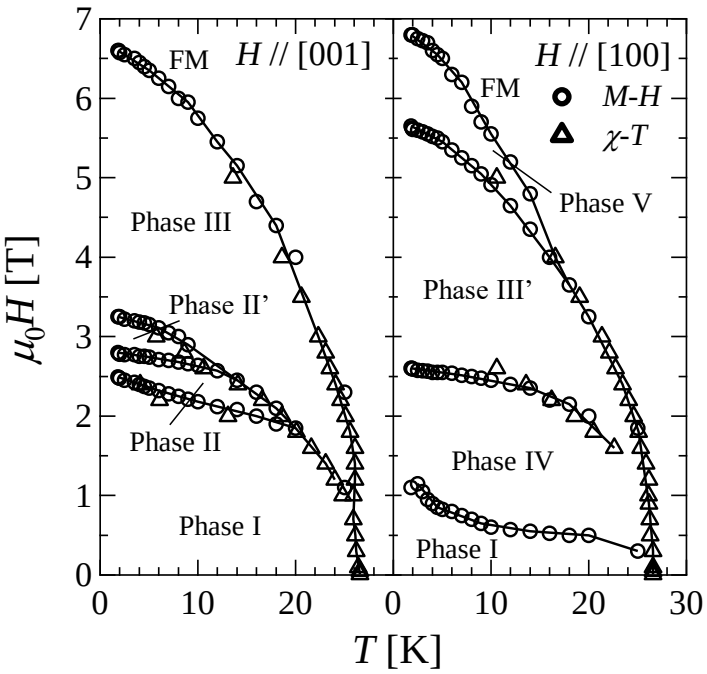

Figure 3.6: The magnetic field-temperature phase diagram for $GdOs_2Si_2$, with the magnetic field applied parallel to [001] (left) and [100] (right), based on magnetic measurements.

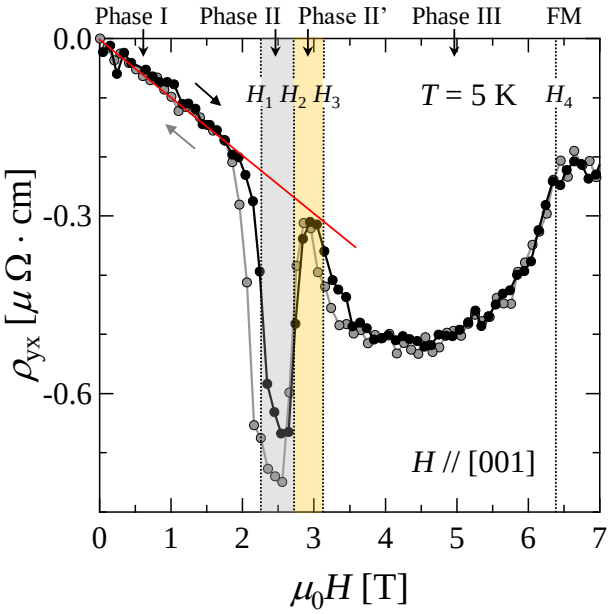

Figure 3.7: Magnetic field dependence of ρ_{yx} at 5 K for H//[001] and I//[100]. The black and gray curves represent ρ_{yx} with increasing and decreasing magnetic fields, respectively. The gray and yellow regions correspond to the phases II and II ' , respectively.

have suggested the existence of a topologically trivial double-Q state in the immediate vicinity of the double-Q square lattice state [85]. The phase II' observed here may reflect such a state, but further microscopic techniques are needed to accurately evaluate the exact magnetic structure.

In the study for H//[100], the existence of four magnetically ordered phases is suggested, namely phases I, III', IV, and V, which are qualitatively similar to those reported for $GdRu_2Si_2$ [84]. In $GdRu_2Si_2$, these phases are associated with anisotropic double-Q states (screw + sinusoidal), anisotropic double-Q states associated with a double-Q square vortex lattice, single Q-screw states, and single Q-fan states [84]. While it remains to be confirmed whether these states directly apply to $GdOs_2Si_2$, it is suggested that phase I of $GdOs_2Si_2$ extends closer to the boundary of the paramagnetic region and is potentially more stable than phase I of $GdRu_2Si_2$ [84]. In contrast, phase V only exists in the high-field part of the phase diagram and ceases well below the zero-field antiferromagnetic transition temperature. This persists even when the magnetic field is no longer small, continuing almost up to the zero-field transition temperature. The differences in these quantitative changes are likely attributed to variations in the strength of the magnetic interaction between the respective Gd^{3+} moments in $GdRu_2Si_2$ and $GdOs_2Si_2$.

The temperature dependence of C_p at zero magnetic field is shown in Fig.3.8 (inset), where a distinct λ-type anomaly is observed at T_1. Since the isostructural nonmagnetic compounds usually used to separate the lattice contribution from the C_p data were not available, I attempted to analyze the data using the Einstein and Debye models: $C_p = \gamma T + C_E + C_D$. In this equation, the first term represents the conduction electron contribution and γ is the Sommerfeld coefficient. The second and third terms correspond to the phonon contribution according to the Einstein and Debye models and are given by:

$$C_E = 3n_E R \frac{x e^x}{(e^x - 1)^2}, \tag{3.3}$$

and

$$C_D = 9n_D R \left(\frac{T}{\theta_D}\right)^3 \int_{D_0}^{\theta} \frac{y^4 e^y}{(e^y - 1)^2}, \tag{3.4}$$

where $x = \theta_E/T, y = \theta_D/T, \theta_E$ and θ_D are the Einstein and Debye temperatures, respectively. The scale factors n_E and n_D correspond to the number of vibrational modes per formula unit for the Einstein and Debye models, respectively, so I applied the constraint $n_E + n_D = 5$. Fitting using these equations yielded $\gamma = 24.4(9)$ mJ mol^{-1}, $n_E = 2.44(5)$, $n_D = 2.55(5)$, $\theta_E = 142(2)$ K, and $\theta_D = 609(9)$ K.

Furthermore, the magnetic specific heat (C_{mag}) of $GdOs_2Si_2$ was obtained by subtracting the contributions of conduction electrons and lattice vibrations from the C_p data, as shown in Fig.3.8. The behavior of C_{mag} decreases rapidly as the temperature passes T_1. A broad hump then appears, and eventually, C_{mag} approaches zero in the low-temperature limit. Similar humps have been observed in other Gd compounds in the temperature range below the magnetic transition temperature [86]. It has been argued that a peak like this appears at approximately 1/4 of magnetic transition temperatures, based on a mean-field model, originating from the splitting of the Gd^{3+} ground-state multiplet due to an internal field [87–89].

It is important to note that in the ρ_{xx} vs T measurements, negative magnetoresistance, indicative of magnetic precursor effects, was observed above T_1 (discussed later). However, the broad peak of C_{mag} at high temperatures, characteristic of the magnetic precursor effect [90, 91], was not clearly observed. The calculated magnetic entropy $S_{mag} = 15.7$ J mol^{-1} K^{-1} is slightly smaller than the theoretical value $R\ln(2J+1) = 17.3$ J mol^{-1} K^{-1} ($J = 7/2$). This discrepancy

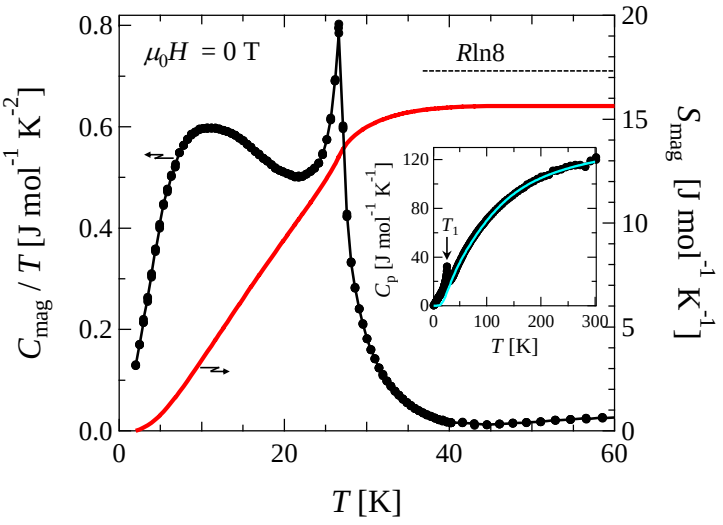

Figure 3.8: Temperature dependence of magnetic specific heat (C_{mag}) and magnetic entropy at μ_0H = 0 T. The inset displays the C_p-T data and the fitting curve (solid blue light line) obtained using the Einstein and Debye formula.

may have been due to the limited temperature range in the analysis, which may have affected the fitting process.

Temperature dependence of electrical resistivity is presented in Fig.3.9. The ρ_{xx} vs T curves exhibit anomalies at characteristic temperatures of T_1, T_2, and T_3, which correspond to the temperatures determined in the magnetization measurements. At μ_0H = 0 and 1 T, ρ_{xx} decreases as the temperature is lowered below T_1. However, at $\mu_0H \geq 2$ T, a significant change in the temperature dependence of ρ_{xx} is observed. Specifically, at μ_0H = 2 T, ρ_{xx} experiences an abrupt increase near T_2 during cooling, followed by a subsequent decrease with further cooling. For $\mu_0H \geq 2.4$ T, ρ_{xx} shows a weak kink at T_1 and a subsequent slight increase, followed by a further increase below T_2. Interestingly, as shown in the inset of Fig.3.9, a negative magnetoresistance is observed not only below T_1 but also at high temperatures, specifically below 40 K. This finding suggests the presence of the magnetic precursor effect, a phenomenon observed in isostructural Gd-based compounds [91, 92].

3.1.3 Conclusion

This study presents the results obtained from investigating $GdOs_2Si_2$ using a single crystal, leading to the construction of a magnetic phase diagram along H//[100] and H//[001], revealing notable similarities with the phase diagram of $GdRu_2Si_2$. Of particular interest is the distinct Hall resistivity anomaly observed in phase II, reminiscent of the topological Hall effect seen in the skyrmion state of $GdRu_2Si_2$. This intriguing parallel suggests the potential occurrence of skyrmion formation in phase II of $GdOs_2Si_2$. Additionally, my investigation unveils an unrecognized phase (phase II') absent in $GdRu_2Si_2$. The appearance of this phase coincides with a distinct recovery pattern in the Hall resistivity, implying a significant shift in the spin structure. In-depth understanding of the complex magnetic configurations in $GdOs_2Si_2$ could be facilitated by future endeavors involving advanced microscopic techniques like resonant X-ray diffraction

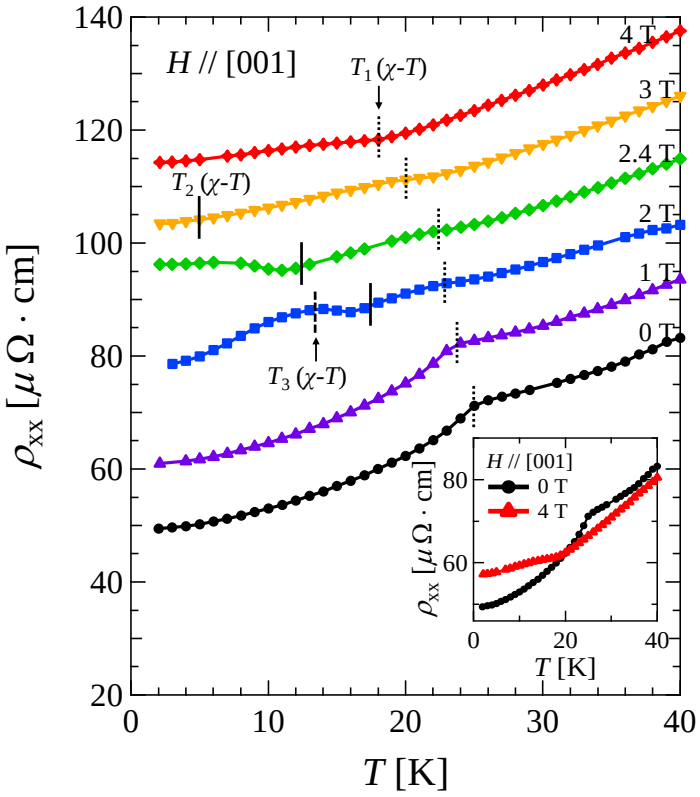

Figure 3.9: Temperature dependence of C_{mag}/T below 40 K under various magnetic fields. The magnetic transition temperatures at T_1, T_2, and T_3 determined from χ-T measurements are indicated by dotted, solid, and dashed lines, respectively. The data have been shifted for clarity.

measurements and the direct observation of possible skyrmions through electron microscopy.

3.2 The topological Hall effect in Gd_2NiSi_3 with triangular lattice

Gd_2PdSi_3 has a layered structure with triangular lattice of Gd^{3+} ions, and dominant RKKY interaction among nearest-neighbor Gd^{3+} ions is antiferromagnetic, thus this system exhibit magnetic frustration. Due to this frustration, a variety of temperature- and magnetic field-dependent magnetic phase diagrams including a skyrmion phase with topological Hall effect has been reported in Gd_2PdSi_3 [53]. From the similarity to Gd_2PdSi_3, an Ni-substituted intermetallic compound, Gd_2NiSi_3 is expected to show skyrmion phase and topological Hall effect; some theoretical studies suggest the emergence of skyrmions in frustration system [44, 49]. Although there have been reports on the synthesis and properties of powder samples of Gd_2NiSi_3 [93, 94], no reports on single crystals growth and physical properties have been reported. Here, I succeeded in growing a single crystal of Gd_2NiSi_3 by the floating zone method for the first time, and report the results of structural and physical property measurements of the single crystal sample.

3.2.1 Experimental

Single crystals of Gd_2NiSi_3 were grown by optical floating zone (OFZ) method under argon pressure. First, a stoichiometric mixture of reagents, Gd, Ni, and Si was melted in the mono-arc furnace under reduced pressure in argon atmosphere. The obtained polycrystalline sample identified as Gd_2NiSi_3 by powder x-ray diffraction measurements was subsequently grinded, transferred to rubber forms, evacuated, and pressed into rod shape at around 700 bar. The rod divided into two pieces was installed in a high-pressure high-temperature optical floating zone furnace (Model HKZ, SciDre GmbH, Dresden), followed by a growth under 30 bar argon pressure. The growth velocity was between 10 and 20 mm/h. Finally, the gray and shiny single crystals were obtained by crashing the product as depicted in Fig.3.10 (b). In this furnace, crystals can be grown under positive Ar pressure, which prevents decomposition and evaporation of materials at high temperatures and enables stoichiometric synthesis. The OFZ method was used in this experiment because crystal growth in a tetra-arc furnace requires maintaining negative pressure inside the furnace, which leads to increased evaporation of materials with low vapor pressure.

The crystallographic data of selected single-crystal sample [Fig.3.10 (a)] were acquired using Rigaku XtaLab mini II diffractometer, utilizing Mo K_α radiation. Furthermore, the crystal axial direction was determined using Laue reflection method, and obtained Laue photo is shown in Fig.3.10 (c).

Magnetic susceptibility and magnetization measurements were carried out in a temperature range of 1.8 K to 300 K, as well as magnetic field ($\mu_0 H$) range of 0 T to 7 T using SQUID magnetometer (MPMS3, Quantum Design, Inc.). Longitudinal resistivity (ρ_{xx}) and Hall resistivity (ρ_{yx}) were measured using four-prove method in transport option of the PPMS (Quantum Design Inc.). To eliminate mixing of ρ_{xx} and ρ_{yx}, measurements were performed in positive and negative fields and experimental signals ρ_{xx}^{exp} and ρ_{yx}^{exp} were symmetrized and antisymmetrized to obtain true ρ_{xx} and ρ_{yx} respectively: i.e., $\rho_{xx}(B) = (\rho_{xx}^{exp}(B) + \rho_{xx}^{exp}(-B))/2$, and $\rho_{yx}(B) = (\rho_{yx}^{exp}(B) - \rho_{yx}^{exp}(-B))/2$. Au wires were reinforced with silver paste for electrical contacts on the crystal, and an excitation current of 50 mA and magnetic field were applied along a-axis and c-axis direction of the crystal, respectively.

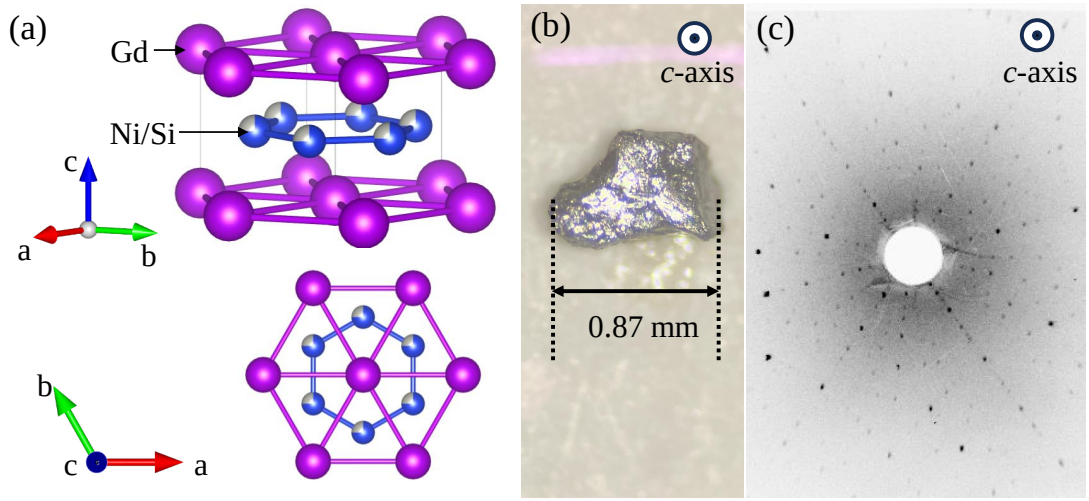

Figure 3.10: (a) Schematic representation of the crystal structure of Gd_2NiSi_3, displaying its hexagonal structure ($P6/mmm$). (b) Photograph and (c) the Laue photo depicting a Gd_2NiSi_3 sample grown by OFZ method. The vertical direction of the paper represents the c-axis.

3.2.2 Results and discussion

The χ–T curves for zero-field cooling (ZFC) and field cooling (FC) at H = 0.1 T for $H \parallel$ [0001] are shown in Fig.3.11. Both ZFC and FC susceptibility have a clear peak at T_N = 13.6 K, indicating that local magnetic moments of Gd^{3+} ions order antiferromagnetically at T_N, while the ZFC and FC curves start to diverge below T_f = 10.3 K. This difference between ZFC and FC at T_f becomes insignificantly small under magnetic field of 1 T (see the inset of Fig.3.11).

In the paramagnetic region above 50 K, reciprocal susceptibility follows the Curie-Weiss low $1/\chi = (T-\theta_W)/C$ (Fig.3.12), where C and θ_W are the Curie constant and Weiss temperature. Their values are estimated to C = 7.90 emu K mol^{-1} and θ_W = +11.3 K, assuming the linear function. The positive value of θ_W denotes the presence of a ferromagnetic exchange interaction in the systems. The effective moment is calculated from the Curie constants to be μ_{eff} = 7.95 μ_B, which well agree with μ_{eff} = 7.94 μ_B of the theoretical value for Gd^{3+} ion. Thus, the $4f$ electrons of Gd^{3+} ions are localized, while the $3d$ electrons from Ni ions are itinerant causing Pauli paramagnetic behavior. The similar behavior has been reported in previous study on Gd_2NiSi_3 [93,94] and Gd_2PdSi_3 [51,52]. Note that the Weiss temperature is positive despite the antiferromagnetic ordering, as in the case of Gd_2PdSi_3, $Gd_3Ru_4Al_{12}$, and $GdRu_2Si_2$ [55,62,93], implying Gd_2NiSi_3 is highly expected to emerge a skyrmion lattice.

Table 3.1: Gd-based skyrmion intermetallics and their Weiss temperatures.

	Gd_2NiSi_3	Gd_2PdSi_3 [93]	$Gd_3Ru_4Al_{12}$ [55]	$GdRu_2Si_2$ [62]
θ_W	**+11.3 K**	+14.3 K	+63.8 K	+43 K

Isothermal magnetization curve at 2 K for $H \parallel$ [0001] and its differential curve are shown in Fig.3.13 (a), exhibiting slight anomaly at H_c = 1.2 T, and this anomalous behavior can be

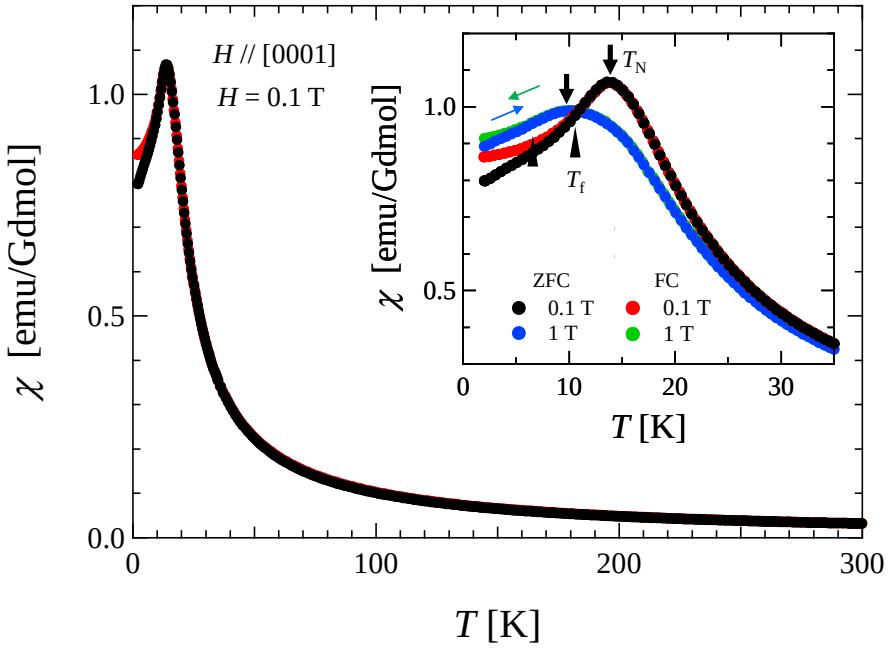

Figure 3.11: The temperature dependence of magnetic susceptibility under magnetic field of 0.1 T along [0001] direction. Black and red curves exhibit ZFC and FC data, respectively. The inset shows the magnetic dependence of χ-T behavior.

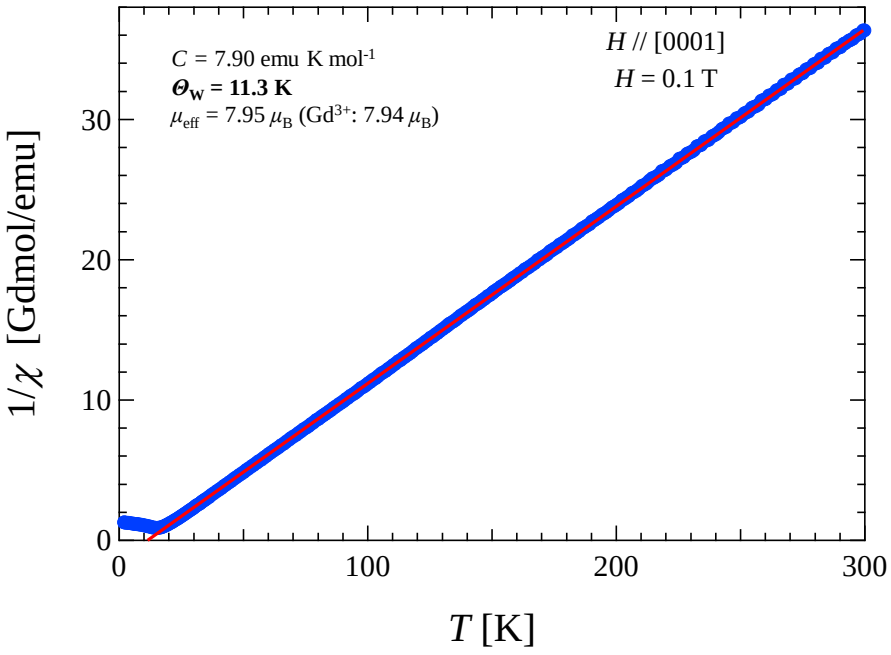

Figure 3.12: The reciprocal susceptibility as a function of temperature under 0.1 T. Blue curve exhibits obtained data and red line indicates Curie Weiss fitting over 50 K.

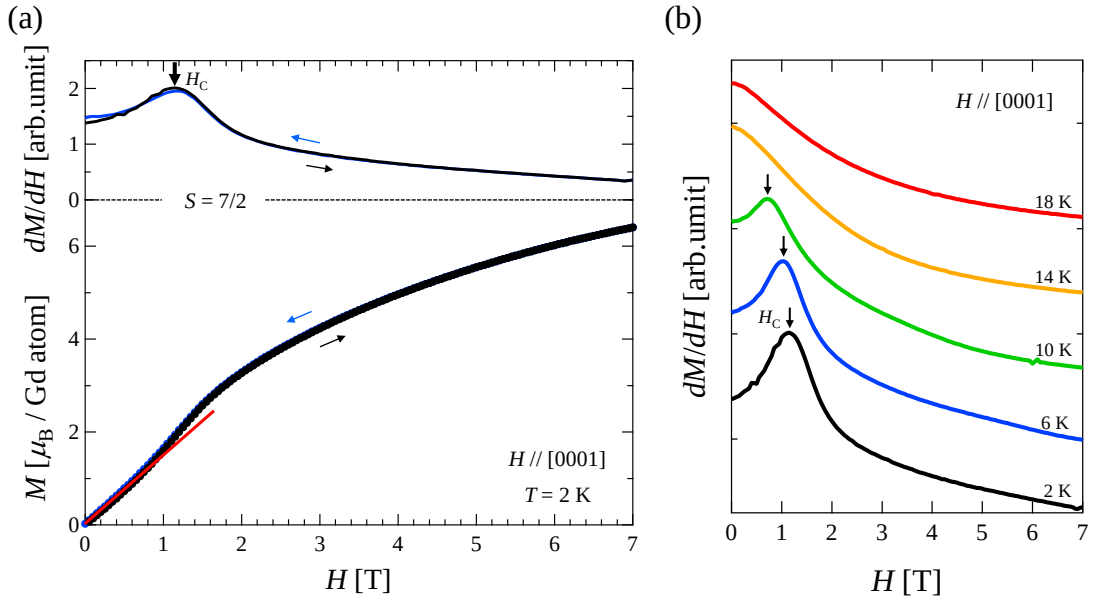

Figure 3.13: (a) Isothermal magnetization and differential curves at T = 2 K (H || [0001]). Black and blue color corresponds to the magnetic-field sweeping direction, increasing and decreasing, respectively. The temperature dependence of differential magnetization along [0001] direction. More pronounced anomaly in H_c is observed in differential curves.

more clearly seen by extrapolation line (red line) or in the differential curve. The magnetization process show isotropic behavior regardless of the sweep direction of the magnetic field. Since the magnetization curve reaches 7 μ_B, the maximum magnetization for Gd^{3+} ions, nothing anomalous will occur any more at higher fields than 7 T. The field-induced transitions occur also at other temperatures as shown in Fig.3.13 (b). The transition fields (H_c) shift to lower fields with increasing temperature, and disappears above approximately 10 K.

The phase diagram for H || [0001] is depicted by plotting T_N, and H_c, as shown in Fig.3.14. It is classified into 3 magnetic phases, depending on temperature and magnetic field. The overall structure of the phase diagram is quite similar to that of Gd_2PdSi_3 [52], and Phase X corresponds to the phase in which a skyrmion lattice and topological Hall effect are observed [53]. The phases I and II likely correspond to the a certain ellipticity of the spin-spiral structure, and a fan-like or a transverse conical structure, respectively [53]. To give a further discussion what magnetic structure is emerged in each phase, I apply the Hall resistivity measurements.

Field-dependent Hall resistivity ρ_{yx} at 2 K is shown in Fig.3.15 (a). It shows drastic changes at H_c, suggesting strong coupling between the Gd^{3+} local moments and conducting electrons. This field dependency is similar to that of Gd_2PdSi_3, and considering that a skyrmion lattice tends to greatly enhance ρ_{yx}, the phase X may indicate skyrmion phase. In addition, topological Hall resistivity ρ_{yx}^{T}, considered as a good probe for the existence of skyrmions or related topological spin textures is extracted by subtracting the normal Hall resistivity ρ_{yx}^{N} and anomalous Hall resistivity ρ_{yx}^{A} determined from magnetization measurements, as shown in Fig.3.15 (b). ρ_{yx}^{T} exhibits a pronounced anomaly in Phase X, with a clear topological Hall effect observed. The anomaly is sharply suppressed in Phases I and II, suggesting that both phases are not skyrmion

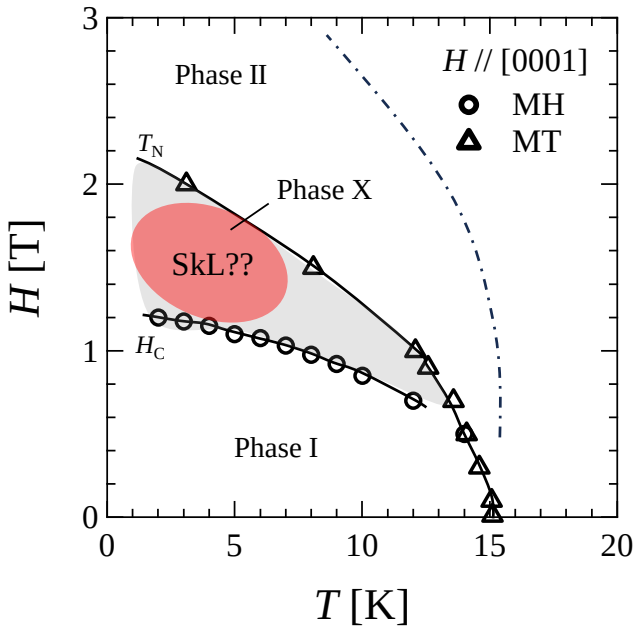

Figure 3.14: The magnetic field-temperature phase diagram of Gd_2NiSi_3 along $H \parallel [0001]$. Circles and triangles corresponds to anomalies for MH and MT measurements (H_c and T_N), respectively. The red area (Phase X) is highly expected to skyrmion phase due to the similarity to Gd_2PdSi_3.

or topological spin structure, as discussed above.

The temperature dependent longitudinal electrical resistivity, ρ_{xx} indicates minimum and maximum values at T_{min} and T_{max} under zero-field as shown in Fig.3.16. The resistivity just below T_{min} sharply increases, while it slightly decreases below T_{max}. The T_{min} behavior is gradually collapsed by increasing magnetic field and completely suppressed at 7 T. Besides, T_{max} also get blurry. It is important to mention that a negative magnetoresistance indicative of the magnetic precursor effect above T_{min} was observed. However additional measurements to confirm the characteristic feature of the magnetic precursor effect [52], such as a broad peak in C_{mag} at higher temperatures is required.

3.2.3 Conclusion

Temperature dependence of magnetic susceptibility χ and longitudinal resistivity ρ_{xx}, and field dependence of magnetization M and Hall resistivity ρ_{yx} were measured along $H \parallel [0001]$, using a single crystal of Gd_2NiSi_3, to establish a magnetic phase diagram. The phase diagram is quite similar to Gd_2PdSi_3, suggesting that the skyrmion lattice is realized on the Gd^{3+} triangular lattice in Phase X. Field dependence of Hall resistivity and topological Hall resistivity ρ_{yx}^{T} also shows the similarity with that of Gd_2PdSi_3, supporting the existence of the triangular skyrmion lattice. In addition, longitudinal resistivity exhibits characteristic feature of the magnetic precursor effect. These similarity will lead to a further understanding of the existence conditions of a skyrmion lattice.

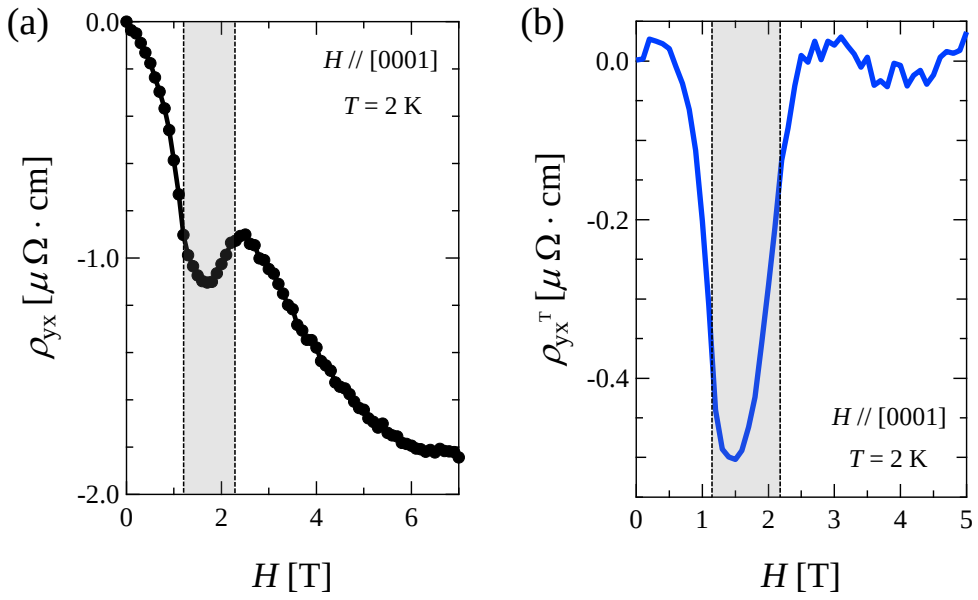

Figure 3.15: (a) Hall resistivity and as a function of magnetic field along [0001] direction. The gray region corresponds to the area expected skyrmion phase (Phase X). (b) The topological Hall resistivity by subtracting normal and anomalous Hall term, respecting to $\rho_{yx} = \rho_{yx}^{N} + \rho_{yx}^{A} + \rho_{yx}^{T}$

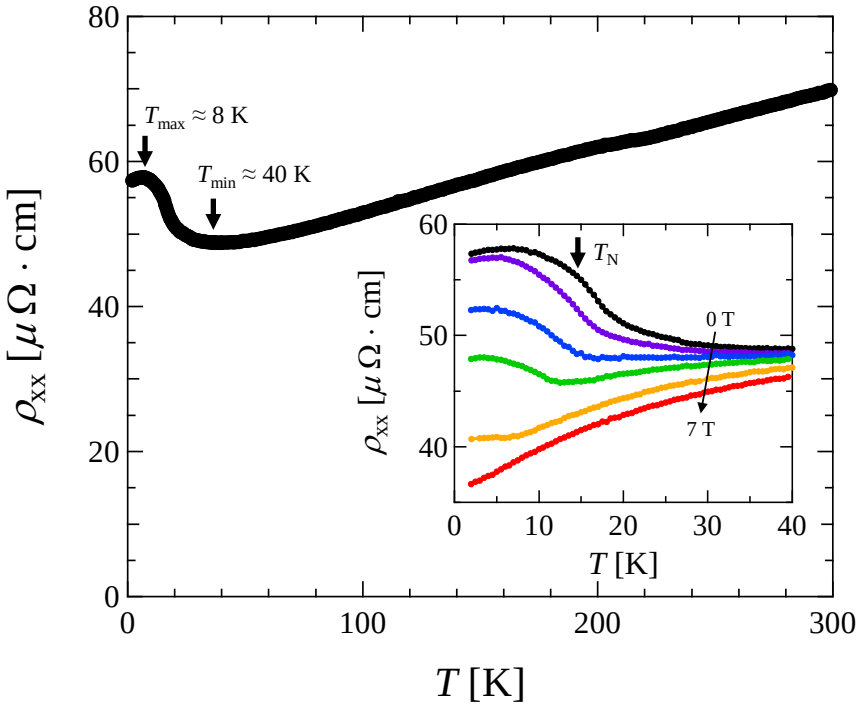

Figure 3.16: The temperature dependence of longitudinal resistivity (ρ_{xx}) The inset exhibits magnetic field dependence of ρ_{xx} below 40 K.

3.3 High-pressure synthesis and magnetic properties of $Gd_2Rh_3Al_9$ with a distorted honeycomb lattice

The majority of magnetic skyrmions recently discovered in material systems with inversion symmetry are found in layered compounds [51–56, 95, 96]. This is because multiple propagation vectors are energetically equivalent and become degenerate due to rotational operations. For instance, the single-Q magnetic state in Gd_2PdSi_3 [51–53] and $Gd_3Ru_4Al_{12}$ [54–56, 95, 96] exhibits triple degeneracy on a triangular lattice, which facilitates the formation of triangular skyrmion lattices. Similarly, in $GdRu_2Si_2$ [57–59, 83, 84], square skyrmion lattices emerge due to quadruple degeneracy on the square lattice. Consequently, multi-Q states demonstrate enhanced stability in lattices with high rotational symmetry.

While the high rotational symmetry of layered structures suggests the stabilization of skyrmion lattices, skyrmion lattices have also been observed in distorted lattices. For example, tetragonal $EuAl_4$ exhibits a structural transition to an orthorhombic lattice at low temperatures. This transition results in Eu^{2+} layers breaking their four-fold rotational symmetry, yet a rhombic skyrmion lattice still emerges [66]. Additionally, theoretical studies have been conducted on the effects of orthorhombic distortion on skyrmion stabilization [97]. Experimental verification is needed to support these theoretical findings.

In this chapter, my emphasis lies in the quest for intermetallic compounds featuring distorted crystal structures, aiming to uncover potential magnetic skyrmions. A notably auspicious candidate in this context is a Gd-based intermetallic compound of $Y_2Co_3Ga_9$-type, wherein Gd takes the place of Y, existing within a subtly distorted honeycomb lattice. This suggests its viability as a host material for magnetic skyrmions [98–100]. As a stride towards this objective, I synthesized $Gd_2Rh_3Al_9$ by substituting Rh for Co and Al for Ga. This paper provides an account of the synthesis of this $Gd_2Rh_3Al_9$ compound of $Y_2Co_3Ga_9$-type, detailing its crystal structure, essential magnetic properties, and electrical conduction behavior. The findings provide insights into the characteristics of this compound and its potential as a platform for investigating distinct magnetic states.

3.3.1 Experimental

Polycrystals and single crystals of $Gd_2Rh_3Al_9$ were synthesized using the Al self-flux method under high-pressure and high-temperature conditions. The raw materials, Gd, Rh, and Al, were combined in a molar ratio of 2:3:9.9 and encapsulated within a BN capsule. This assembly was then enclosed in an outer capsule made of Ta. The entire capsule arrangement was placed within a multi-anvil high-pressure apparatus (CTF-MA1500P; C&T Factory Co., Ltd., Tokyo, Japan) and subjected to heating at 1600 °C for 1 hour. Subsequently, a gradual cooling process occurred over 2 hours, reaching 900 °C, while maintaining a pressure of 6 GPa. The high-pressure synthesis method was adopted because the expensive Rh powder was not applicable to synthesis methods such as the FZ and CZ methods, which require a large amount of starting materials. I believe that the FZ and CZ methods can be used to grow $Gd_2Rh_3Al_9$ crystals in the same way, given the fact that $Gd_2Rh_3Al_9$ powder samples can be synthesized by arc-melting method.

Following the heating steps, rapid cooling procedures brought down the capsule's temperature to below 100 °C in less than 30 seconds. Subsequently, the pressure was methodically released over a 2-hour period. The resulting product comprised gleaming grey crystals clustered at the lowermost section of the BN capsule, alongside a polycrystalline segment that formed in

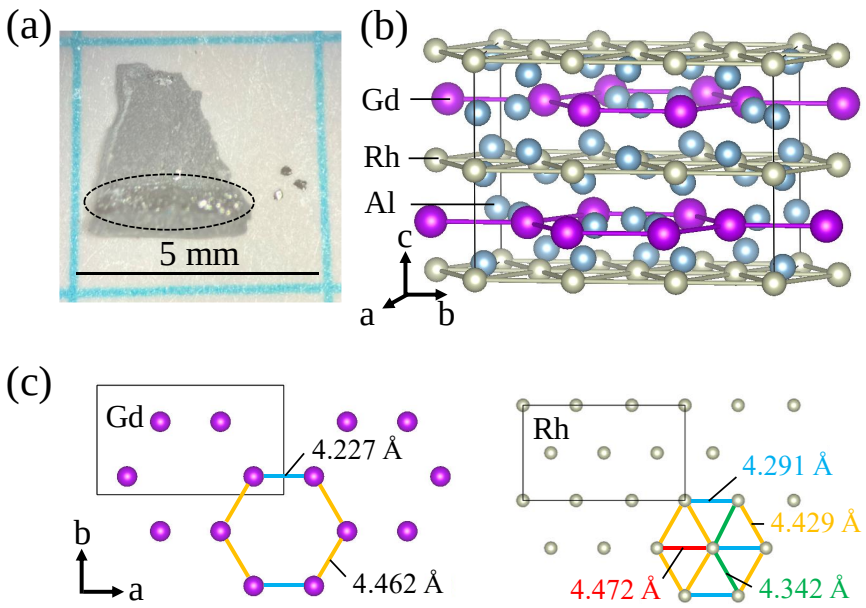

Figure 3.17: (a) Photograph depicting a $Gd_2Rh_3Al_9$ sample synthesized under high pressure. The dotted ellipse delineates a clustered area of single crystals formed at the bottom of the BN capsule. Adjacent to the sample are crystal fragments detached from this area. The region above the dotted area is polycrystalline. (b) Schematic representation of the crystal structure of $Gd_2Rh_3Al_9$, displaying its orthorhombic structure (*Cmcm*). (c) View of the didstorted Gd-honeycomb lattice and Rh-triangular lattice from the c-axis direction. The numbers indicate interatomic distances, revealing slight distortions from the ideal lattice.

the major region of the sample. The crystals from the former category underwent physical fragmentation, yielding minute crystals akin to single domains, with dimensions not exceeding 0.2 mm [Fig.3.17 (a)]. Maintaining high-pressure conditions was essential in this synthesis. Without such conditions, achieving the desired chemical phase would not have been possible.

Crystallographic data were obtained from a carefully selected crystal, which had been polished and cleaned to eliminate any potential residue of Al flux. These data were analyzed using a Rigaku XtaLab mini II diffractometer, employing Mo K_α radiation. The crystal structure was elucidated using a dual-space algorithm approach (SHELXT) [101], and further refinement was conducted utilizing a full-matrix least-squares technique with SHELXL [102]. The refinement process was managed through the Olex graphical user interface. The comprehensive results obtained from this intricate process are meticulously compiled and documented in Tables 3.2 and 3.3.

Additionally, we conducted Scanning Electron Microscope-Energy Dispersive X-ray Spectroscopy (SEM-EDX) measurements on a polished surface of the selected specimen, mounted on carbon tape as shown in Fig3.18. This analysis, performed using a TESCAN Vega-e SBU scanning electron microscope equipped with EDS and operating at an accelerating voltage of 15 kV, yielded the elemental ratio Gd:Rh:Al = 1.73(4):3.10(4):9.17(5). These results indicate that the ratio of Gd is slightly lower than the stoichiometry of $Gd_2Rh_3Al_9$, as further detailed in Table

Table 3.2: Crystallographic parameters and refinement details of a single crystal of $Gd_2Rh_3Al_9$

Empirical formula	$Gd_2Rh_3Al_9$
Formula weight	866.05
Temperature	293(2) K
Wavelength	0.71073 Å(Mo K_α)
Space group	$Cmcm$
Unit cell dimensions	a = 13.0538(4) Å, b = 7.6455(3) Å, c = 9.5117(3) Å
Volume	949.29(6) Å^3
Z	4
Density (calculated)	6.060 g cm^{-3}
Absorption coefficient	19.649 mm^{-1}
F_{000}	1520
Crystal size	$0.066 \times 0.056 \times 0.024$ mm^3
2θ for data collection	3.0710 - 30.4550 °
Index ranges	$-16 \leq h \leq 18, -10 \leq k \leq 10, -13 \leq l \leq 13$
Reflections collected	7294
Independent reflections	793 [R(int) = 0.0313]
Completeness to θ = 25.242°	100 %
Absorption correction	multi-scan
Max. and min. transmission	1.000 and 0.738
Data/restraionts/parameters	793/0/42
Goodness-of-fit on F^2	1.064
Final R indices [$I > 2\sigma(I)$]	R_1 = 0.0147, wR_2 = 0.0285
R indices (all data)	R_1 = 0.0178, wR_2 = 0.0291
Extinction coefficient	0.00068(3)
Largest diff. peak and hole	1.088 and −0.721 e Å^{-3}

3.4. However, we believe this discrepancy is more likely attributable to instrumental precision issues rather than a significant deviation from the intended stoichiometry.

Magnetic susceptibility (χ) and isothermal magnetization (M) measurements were carried out across a temperature range spanning from 2 K to 300 K, employing magnetic fields up to 70 kOe. These analyses were performed using a SQUID magnetometer MPMS3 (Quantum Design, Inc.). To assess specific heat capacity (C_p) and direct current electrical resistivity (ρ), I employed a relaxation method and a four-probe technique, respectively. These experimental procedures were conducted utilizing a PPMS (Quantum Design Inc.).

It is important to emphasize that due to the constrained dimensions of the single-domain-like crystals, it was not feasible to perform assessments of physical properties along a specific crystal direction within my measurement apparatus. Consequently, with the exception of the structural study, all measurements were conducted using polycrystalline samples. Powder X-ray diffraction (XRD) analysis, the pattern of which is provided in the Fig.3.19, identified a small amount of RhO_2 as an impurity in the polycrystalline sample. However, given that RhO_2 is nonmagnetic and exhibits metallic electrical conductivity within our measurement temperature

Table 3.3: Atomic coordinates and equivalent isotropic displacement parameters (U_{eq}; 10^{-3} Å^2) and anisotropic displacement parameters (U_{ij}; 10^{-3} Å^2) as measured by X-ray diffraction on a single-crystal $Gd_2Rh_3Al_9$ at 293 K.

Site	WP [a]	Occp.	x	y	z	U_{eq} [b]
Gd	8g	1	0.65998(2)	0.83145(2)	1/4	5.69(6)
Rh1	8e	1	0.67087(2)	1/2	1/2	4.55(7)
Rh2	4b	1	1/2	0	1/2	4.58(8)
Al1	8f	1	1/2	-0.1279(2)	0.0067(3)	6.7(3)
Al2	8g	1	0.60687(9)	0.44226(14))	1/4	7.2(2)
Al3	16h	1	0.83185(6)	0.66700(11)	0.42572(9)	6.24(16)
Al4	8f	1	1/2	0.33228(14)	0.54338(12)	8.6(2)
Site	U_{11}	U_{22}	U_{33}	U_{23}	U_{13}	U_{12}
Gd	6.00(10)	5.95(9)	5.12(8)	0	0	0.51(7)
Rh1	3.76(15)	5.11(14)	4.77(13)	-0.37(11)	0	0
Rh2	4.44(19)	4.56(18)	4.73(16)	0.89(15)	0	0
Al1	4.5(8)	9.1(8)	6.5(7)	0	0	0
Al2	7.5(6)	8.2(5)	5.9(5)	0	0	-1.1(4)
Al3	5.2(4)	6.9(4)	6.6(3)	-0.5(3)	0.5(3)	-0.3(3)
Al4	4.2(6)	6.1(5)	15.6(5)	0.1(5)	0	0

[a] Wyckoff positions

[b] U_{eq} is defined as one third of the trace of the orthogonalized U_{ij} tensor. The anisotropic displacement factor exponent takes the form $-2\pi^2[h^2a^{*2}U_{11} + \ldots + 2hka^*b^*U_{12}]$.

range, we concluded that the intrinsic properties of $Gd_2Rh_3Al_9$ are not significantly affected by the presence of RhO_2.

3.3.2 Results and discussion

The crystal structure of $Gd_2Rh_3Al_9$ was confirmed by XRD analysis to possess a $Y_2Co_3Ga_9$-type structure ($Cmcm$, #63), akin to $Gd_2Co_3Al_9$ [103]. The Gd-honeycomb layers are aligned along the c-axis (Fig.3.17 b). Within the intralayer structure, the hexagons constituting the honeycomb network display subtle contractions along the a-axis. These hexagons are comprised of edges with two distinct bond lengths, measuring 4.227 Å and 4.429Å, respectively (Fig.3.17 c, left side). Similarly, the triangles formed by Rh in the subsequent layers exhibit distortions, encompassing four isosceles triangles and eight non-equilateral triangles within the unit cell (Fig.3.17 c, right side). These minor deviations may stem from the overall structure of the orthorhombic crystal, which exhibits a slight departure from trigonal or hexagonal symmetry.

The temperature-dependent behavior of χ under H = 1 kOe is depicted in Fig. 2a. The inverse of χ conforms well to the Curie-Weiss law, represented by $1/\chi = (T - \theta_W)/C$, for temperatures exceeding 50 K. The Curie constant, C, is calculated to be 7.973(5) emu K mol^{-1}. The corresponding effective moment, p_{eff} = 7.984(2)μ_B, closely aligns with the anticipated value of 7.94 μ_B for free Gd^{3+} ions with S = 7/2. The Weiss temperature, θ_W, is determined to be -32.0(1) K, indicating that the predominant interaction between the magnetic moments of Gd^{3+}

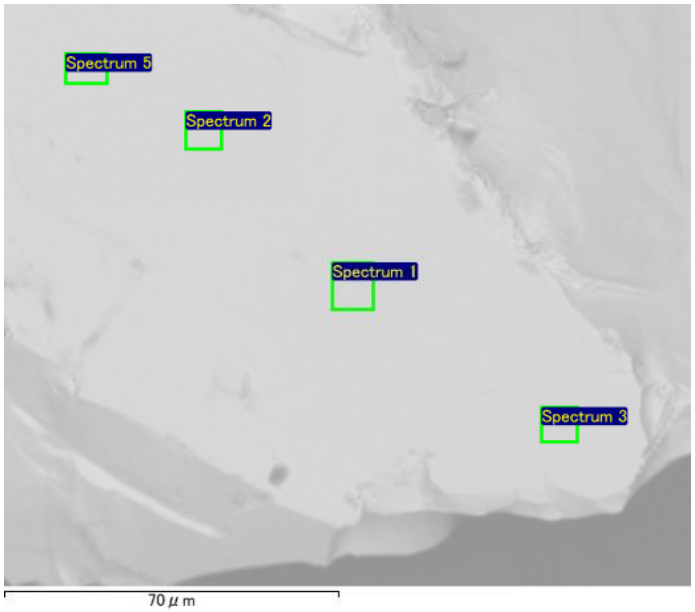

Figure 3.18: SEM image of the selected specimen with the marked area where EDX measurements were performed.

Table 3.4: Crystallographic parameters and refinement details of a single crystal of $Gd_2Rh_3Al_9$

Atomic [%]	Spectrum 1	Spectrum 2	Spectrum 3	Spectrum 5*	**Average**
Gd	1.727	1.742	1.680	1.787	**1.73(4)**
Rh	3.106	3.156	3.069	3.070	**3.10(4)**
Al	9.167	9.102	9.251	9.143	**9.17(5)**
Total	14	14	14	14	

* Spectrum 4 was accidentally skipped.

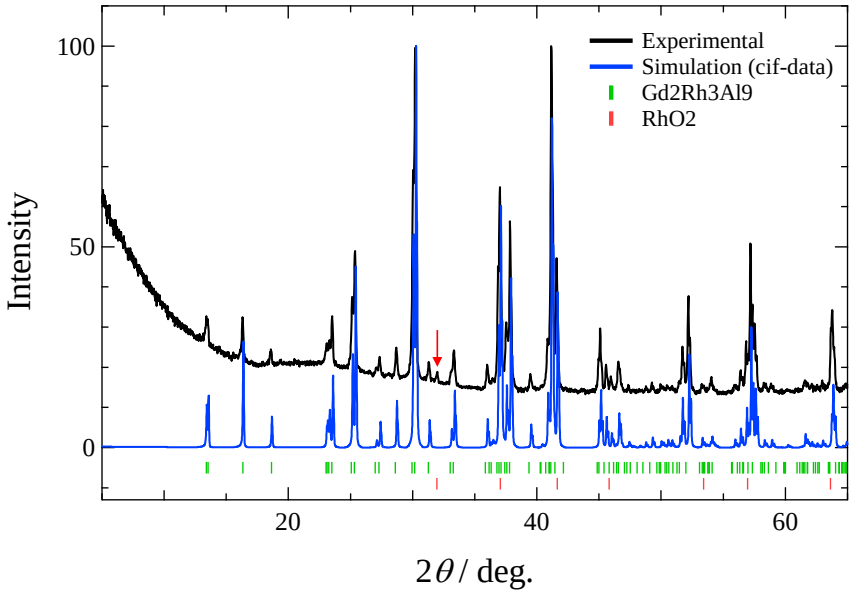

Figure 3.19: Powder XRD diffraction pattern for the polycrystalline $Gd_2Rh_3Al_9$ used in this study. The simulation curve (blue) utilizes data obtained from the single crystal structural analysis.

ions is of an antiferromagnetic nature.

Upon lowering the temperature, a magnetic transition manifested at T_1 in the χ vs T measurements, followed by another distinctive anomaly indicating an additional magnetic transition at a lower temperature, labeled as T_2. Notably, consecutive peaks were discerned at T_1 = 13.6 K and T_2 = 4.1 K at H = 100 Oe. These transition temperatures exhibited minor shifts towards the lower temperature range with the progressive increase of the magnetic field, extending up to H = 70 kOe, as illustrated in Fig.3.20. Considering T_1 as a representative of a long-range antiferromagnetic transition temperature, the corresponding frustration parameter $|\theta_W|/T_1$ was calculated to be 2.34. This value aligns with the range (typically 1-3) often reported for Gd-based intermetallic compounds known to accommodate skyrmions [98–100]. However, the negative θ_W observed here is in considerable contrast to the positive θ_W (20-64 K) reported for other Gd-based intermetallic compounds [98–100].

Figure 3.21 (a) illustrates the isothermal M curves acquired within the temperature range of 2 K to 20 K. Notably, two distinct anomalies are prominently observed at approximately H_1 = 15 kOe and H_2 = 30 kOe. These anomalies are clearly depicted in the differential curves of M at 2 K, as showcased in the inset of Fig.3.21. The anomaly at H_1 materializes below T_1, while the anomaly at H_2 emerges beneath T_2. This observation indicates that the former anomaly is linked to the antiferromagnetic structure formed at T_1, while the latter pertains to the magnetic arrangement existing below T_2. The M value of 4.2 μ_B recorded at 70 kOe under 2 K equates to approximately 60% of the saturation moment exhibited by spins with S = 7/2. However, it is noteworthy that no distinctive step-like anomalies accompanied by magnetic hysteresis, commonly observed in skyrmion compounds [96, 98–100], were discerned in this case. The complex phase diagram depending on magnetic field and temperature derived from MT and MH measurements is shown in Fig.3.21 (b).

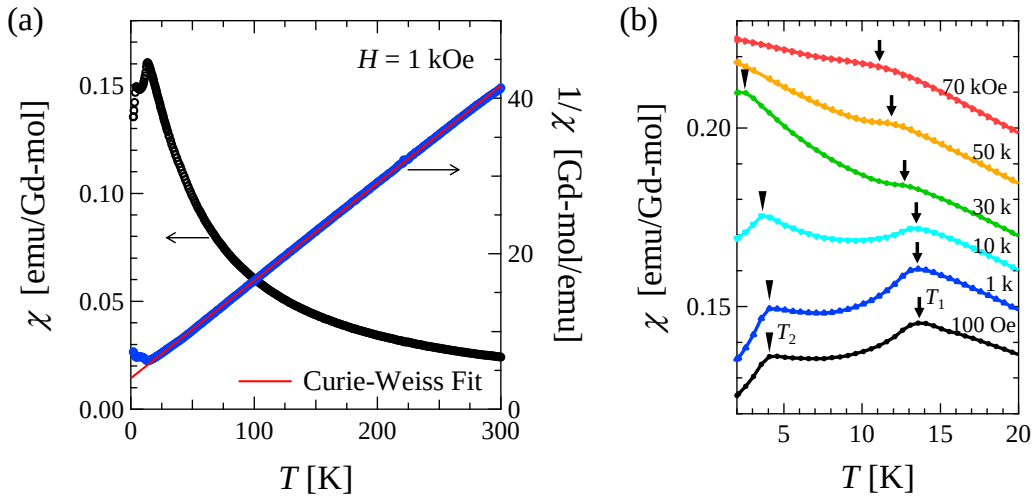

Figure 3.20: (a) Temperature dependence of χ and $1/\chi$ under H = 1 kOe. The solid red line represents the Curie-Weiss fit for the data above 50 K. (b) χ below 20 K under several magnetic fields ranging from 100 Oe to 70 kOe. Arrows and triangular symbols indicate the anomalies at T_1 and T_2, respectively.

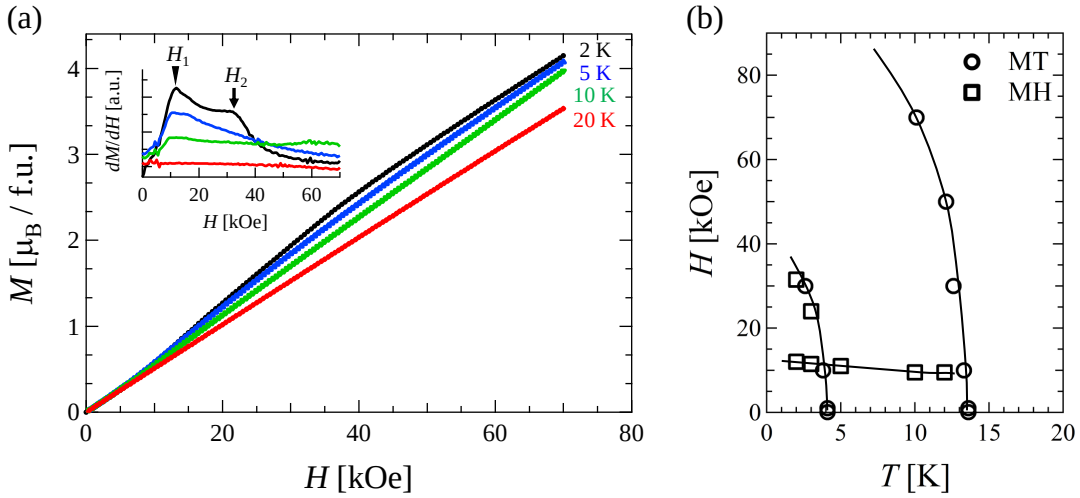

Figure 3.21: (a) Isothermal M curves below 20 K. The inset shows the differential of M ($\mathrm{d}M/\mathrm{d}H$) at each temperature. Arrows within the inset highlight transition points. (b) The magnetic field-temperature phase diagram for $Gd_2Rh_3Al_9$, which is constructed based on the data from our magnetic measurements.

The temperature-dependent behavior of C_p is investigated under magnetic fields of 0 and 70 kOe, as depicted in Fig.3.22 (a). The C_p/T data at zero-field reveals magnetic transitions corresponding to T1 and T2. Notably, the peak associated with T1 shifts towards lower temperatures with the increment of magnetic fields, extending up to 70 kOe. The inset of Fig. 3.22 (a) illustrates a plot of C_p/T versus T^2, wherein a linear fitting is applied based on the equation $C_p/T = \gamma + \beta T^2$. Here, γ represents the electronic specific heat coefficient, and β is a constant associated with the Debye temperature θ_D. The data above T_1 are subjected to fitting, effectively circumventing the influence of the magnetic phase transition. The Sommerfeld coefficient γ is ascertained to be 328 mJ mol^{-1} K^{-2}. While this value surpasses those observed in other Gd-based intermetallic compounds, it remains comparable to the reported value of 500 mJ mol^{-1} K^{-2} in $Gd_2Co_3Al_9$ [103]. The Debye temperature θ_D is calculated to be 168 K based on the estimated β.

The inset of Fig. 5 shows the zero-field ($H = 0$ Oe) C_p curve and lattice contribution calculated from the Einstein-Debye function, which exhibits great fitting for temperatures exceeding 40 K except in the noisy region (250-300 K) due to the sample-fixing grease. The fitting function is described as follows:

$$C_p = \gamma T + 3n_E R\frac{x^2e^x}{(e^x-1)^2} + 9n_D R\left(\frac{T}{\theta_D}\right)^3\int_0^{\theta_D/T}\frac{y^4e^y}{(e^y-1)^2}\mathrm{dy}. \tag{3.5}$$

Here, the first term represents a conduction electron contribution, where γ is the Sommerfeld coefficient. The second and third terms correspond to a phonon contribution following Einstein's and Debye's models, respectively. In the equations, $x = \theta_E/T$, $y = \theta_D/T$, in which θ_E and θ_D are the Einstein and Debye temperatures, respectively. The numbers of Einstein models (n_E) and Debye oscillations (n_D) are constrained by $n_E + n_D = 14$ (the number of atoms per formula unit).

In this case, proper fitting is observed with the following parameters: $\gamma = 16.7(17)$ mJ mol^{-1} K^{-2}, $n_E = 3.1(1)$, $\theta_E = 148(3)$ K, $n_D = 10.9(1)$, and $\theta_D = 493(3)$ K. The estimated γ and θ_D are much smaller and larger, respectively, than those reported for the isostructural compound $Gd_2Co_3Al_9$ ($\gamma = 500$ mJ mol^{-1} K^{-2}, $\theta_D = 187$ K) [103]. Previous studies on $Gd_2Co_3Al_9$ relied solely on the approximate formula $C_p/T = \gamma + \beta T^2$ to estimate these values, potentially making it challenging to accurately isolate the contribution from the magnetic transition. This discrepancy underscores the critical role of fitting methods in precisely determining thermodynamic parameters.

To better understand the magnetic properties, the magnetic specific heat divided by T (C_{mag}/T) and magnetic entropy (S_{mag}), by subtracting lattice contribution from C_p, are shown in Fig.3.22 (b). The C_{mag}/T data at zero-field reveals magnetic transitions corresponding to T_1 and T_2. Notably, the peak associated with T_1 shifts towards lower temperatures with the increment of magnetic fields extending up to 70 kOe. The S_{mag} in zero field estimated by integrating the C_{mag}/T data with respect to T reaches 96.6 % of the expected value Rln8 for S= 7/2 and saturates to Rln8 at around 50 K.

Figure 3.23 illustrates the temperature-dependent behavior of ρ under zero magnetic field and at 70 kOe. Both curves depict a sudden decline just below T_1, likely attributed to the influence of the antiferromagnetic ordering process. While a distinctive hump in the ρ curve has been observed during the transition to a skyrmion phase in $GdRu_2Si_2$ [62], no such anomaly is evident in $Gd_2Rh_3Al_9$. The compound's residual resistivity ratio (RRR) is calculated to be 5.1, implying either a contribution from grain boundary scattering of the polycrystalline sample [104], or that the sample quality may not be at optimal levels.

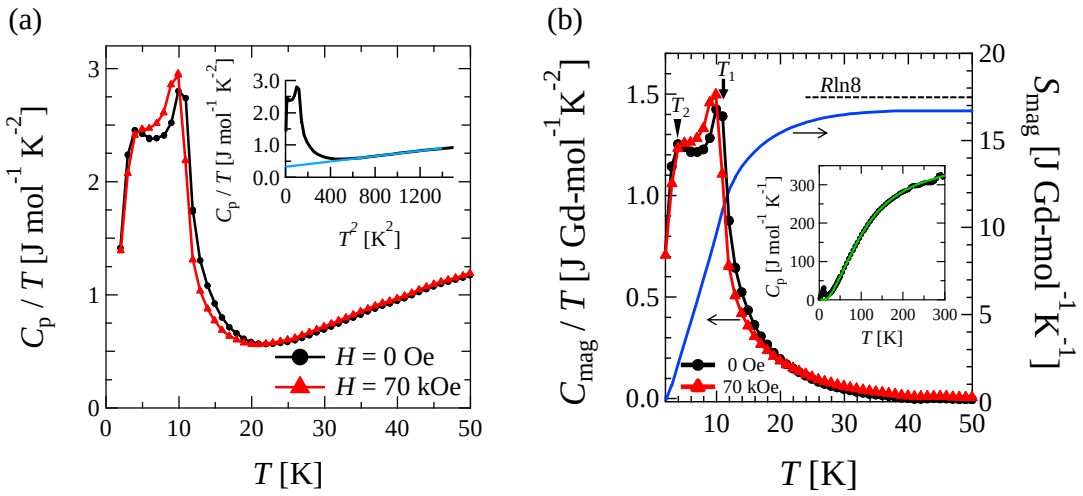

Figure 3.22: (a) Temperature dependence of C_p/T under H = 0 and 70 kOe. Transition temperatures, T_1 and T_2, are indicated by an arrow and a triangular symbol, respectively. The inset displays the C_p/T vs. T^2 plot, with the blue line denoting the outcome of linear fitting. (b) Temperature dependence of C_{mag}/T under H = 0 Oe (black) and 70 kOe (red), and magnetic entropy (blue line). Transition temperatures, T_1 and T_2, are indicated by an arrow and a triangular symbol, respectively. The inset displays the C-T plot, with the green line denoting the fitting by the Einstein-Debye formula.

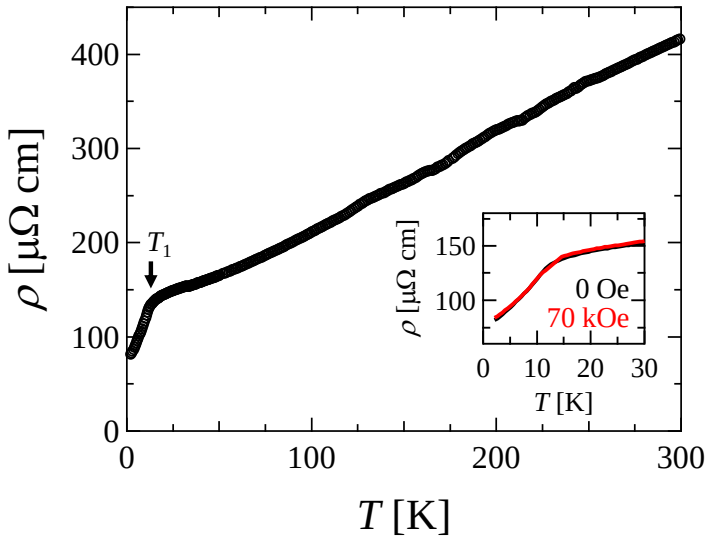

Figure 3.23: Temperature dependence of ρ below 300 K under zero magnetic field. The inset shows the ρ curves under H = 0 and 70 kOe.

3.3.3 Conclusion

I have achieved a significant milestone in synthesizing the Gd-based intermetallic compound $Gd_2Rh_3Al_9$ through high-temperature and high-pressure synthesis. Crystal structure analysis revealed an orthorhombic structure characterized by a distorted Gd-honeycomb network. A comprehensive study of the temperature-dependent behavior of χ, M, C_p, and ρ, in polycrystalline samples revealed sequential antiferromagnetic transitions occurring at T_1 = 13.6 K and T_2 = 4.1 K. These transitions are attributed to the antiferromagnetic interaction between the magnetic moments of Gd^{3+} (S = 7/2) located within the distorted honeycomb layer. The established magnetic phase diagram shows complex temperature and magnetic field dependence, suggesting a various magnetically ordered states.

However, my study did not provide evidence for the existence of a skyrmion phase in this compound. This may be attributed, at least in part, to the significantly stronger antiferromagnetic interactions compared to other Gd-based skyrmion materials. Nevertheless, the data on the magnetic and transport properties of $Gd_2Rh_3Al_9$ obtained in this study offer valuable insights into the intricate behavior of Gd-based intermetallic compounds and their potential as hosts for unique magnetic phases. Furthermore, conducting detailed measurements using single crystals is imperative to further explore the possibility of forming a skyrmion phase in this compound. This remains a subject for future research.

Chapter 4

Anomalous Hall effect in a noncollinear antiferromagnet

4.1 Large anomalous Hall conductivity observed in the cubic-lattice antiferromagnet Mn_3Sb with kagome lattice

The anomalous Hall effect, typically observed in ferromagnetic metals, can also manifest in certain noncollinear antiferromagnetic materials. However, studying the cubic kagome antiferromagnet Mn_3X (X =Ir, Pt, Rh), which was theoretically predicted to exhibit the anomalous Hall effect, has proven challenging due to the extremely small measured values. In this study, I validate these theoretical predictions by successfully measuring a remarkable anomalous Hall conductivity in the cubic kagome antiferromagnet Mn_3Sb, reaching up to $308\,\Omega^{-1}$ cm^{-1}. Combining these results with those obtained from the hexagonal kagome antiferromagnet Mn_3Z (Z =Sn, Ge), my findings contribute to a comprehensive understanding of the anomalous Hall effect in noncollinear antiferromagnetic materials, leading to further advancements in the research on the functions and control of cluster multipoles.

4.1.1 Experimental

Materials preparation

Referring to the binary phase diagram of Mn-Sb, it is evident that only Mn_2Sb and $Mn_{1.1}Sb$ are stable, with no other binary alloys present [105]. Therefore, it is believed that cubic Mn_3Sb did not exist until its synthesis by Yamashita et al. using a high-pressure method in 2003 [106, 107]. In this study, I successfully synthesized cubic Mn_3Sb under similar conditions. Furthermore, I expanded the synthesis pressure range up to 15 GPa and successfully synthesized hexagonal Mn_3Sb.

I synthesized cubic Mn_3Sb under high-pressure conditions (6 GPa, 850 °C) using a multianvil press (CTFMA1500P, C&T Factory, Tokyo, Japan). Furthermore, employing a Kawai-type press at Gakushuin University (UHP1000, Sumitomo Heavy Industries, Ltd., Tokyo, Japan), I expanded the synthesis pressure range up to 15 GPa and successfully synthesized hexagonal Mn_3Sb (15 GPa, 1000 °C). The samples were sintered polycrystals, and no single crystals were obtained.

The starting materials used for the synthesis of both cubic and hexagonal Mn_3Sb were 10 wt.% excess Mn powder (99.9%, Aldrich) and Sb powder (99.9%, Rare Metal). The Mn powder

was pretreated in a hydrogen atmosphere, but it was not possible to completely remove MnO in my laboratory. The Sb powder was used as purchased from the manufacturer without any prior heat treatment. Although a small amount of MnO was detected in the samples, I considered the effect on the physical property measurement to be small since MnO is a Néel temperature 116 K antiferromagnetic material that is electrically insulating and does not have magnetic order at room temperature [108].

Finely ground powders of both alloys were utilized in synchrotron x-ray diffraction (XRD) experiments at temperatures ranging from 100 to 400 K. The XRD measurements were conducted using a large Debye-Scherrer camera at the BL02B2 beamline at SPring-8, Sayo, Japan [109,110]. The synchrotron XRD wavelength used was either 0.42026 or 0.77598 Å, and it was calibrated using CeO_2 as the standard material. The difference in wavelength was not based on any scientific rationale but rather on practical considerations I encountered. The synchrotron XRD data were analyzed using the Rietveld method [111] with RIETAN-FP software [112].

Magnetic and transport properties measurements

The direct-current magnetic susceptibilities of the alloys were measured using a superconducting quantum interference device magnetometer (MPMS, Quantum Design, San Diego, CA, USA). The measurements were performed in the temperature range of 2–550 K using an oven (300–550 K) and an applied magnetic field of 1 T, under both zero-field-cooled (ZFC) and field-cooled (FC) conditions. Isothermal magnetization loops were collected at different temperatures within the magnetic field range of ±1 T. The electrical resistivity (ρ_{xx}) and Hall resistivity (ρ_{xy}) of a polycrystalline material were measured as a function of temperature and magnetic field using a conventional lowfrequency alternating-current four-probe method in a 4He variable temperature insert with a superconducting magnet. Au wires were spot welded and reinforced with silver paste for electrical contacts on the plate-shaped material. To ensure accurate measurements, both positive and negative magnetic fields were applied to eliminate any mixing of ρ_{xx} and ρ_{xy}. The experimental signals, ρ_{xx-exp} and ρ_{xy-exp}, were symmetrized and antisymmetrized to obtain the true ρ_{xx} and ρ_{xy}, respectively. Specifically, $\rho_{xx}(H) = [\rho_{xx-exp}(H) + \rho_{xx-exp}(-H)]/2$, and $\rho_{xy}(H) = [\rho_{xy-exp}(H) - \rho_{xy-exp}(-H)]/2$.

Theoretical calculations

First-principles calculations of cubic Mn_3S and its related materials were carried out using the projector augmentedwave method within the Vienna *abinitio* Simulation Package (VASP) [113]. The calculations employed the generalized gradient approximation (GGA) of density-functional theory with the Perdew-Burke-Ernzerhof exchange functional [114]. Structure optimizations were performed using an $8 \times 8 \times 8$ uniform k-point grid, and Gaussian broadening with a width of 0.1 eV was applied. The final electronic structure was obtained using tetrahedron methods. Maximally localized Wannier functions [115,116] were then constructed using the WANNIER90 program package [117]. The anomalous Hall conductivity was calculated based on the Berry curvature [5] of the energy bands derived from the tight-binding model using the Wannier functions [75,118,119].

The intrinsic anomalous Hall conductivity was determined using the Berry curvature method. Initially, the maximally localized Wannier functions (MLWFs) were generated using the WANNIER90 program code [117], utilizing the energy bands obtained from *abinitio* calculations for

Table 4.1: Atomic positions, occupancies, and thermal displacement parameters of cubic and hexagonal Mn_3Sb obtained using synchrotron XRD

Mn_3Sb	Atom	Site	x	y	z	Occupancy	B_{iso} (Å^2)
Cubic[a]	Mn	3c	0	0.5	0.5	1	0.491(4)
	Sb	1a	0	0	0	1	0.366(5)
Hexagonal[b]	Mn	6h	0.16117(13)	0.322235 (= 2x)	0.5	1	0.503(18)
	Sb	2d	0.33333	0.66667	0.5	1	0.184(16)

[a] Space group: Pm-3m (No. 221). a = 3.99744(1)Å, V = 63.8773(4)Å^3, and Z = 1. D_{cal} = 7.461 g/cm^3; Residuals: R_{wp} = 7.18%, R_p = 5.23%, S = 2.33; Mass fractions of Mn_3Sb, MnO, Mn_2Sb, and Sb were 0.897, 0.067, 0.023, and 0.013, respectively; Sample temperature was 296 K.
[b] Space group: $P6_3/mmc$ (No. 194). a = 5.63434(9)Å, c = 4.53434(6)Å, V = 124.661(3)Å^3, and Z = 2. dcal = 7.635g/cm^3; Residuals: R_{wp} = 10.94 %, R_p = 8.14%, S = 1.60; Mass fractions of Mn_3Sb and MnO other than unknown phase were 0.943 and 0.057, respectively; Sample temperature was 300 K.

the experimental structure. A total of 144 energy bands located above EF-8 eV were employed as input for WANNIER90, where EF represents the Fermi energy. The s, p, and d projectors were utilized for all atoms. To ensure disentanglement [117], the energy range from EF-8 to EF+1.8 eV was selected as the frozen energy region. Subsequently, a tight-binding model was constructed based on the MLWFs. The Berry curvature was then computed for this tight-binding model, employing an adaptive k-point mesh of up to $200 \times 200 \times 200$. The specific configuration of the adaptive k-point mesh [117] chosen was $5 \times 5 \times 5$.

4.1.2 Results

Crystal structure

I investigated the crystal structures of Mn_3Sb in cubic and hexagonal phases using synchrotron XRD data and Rietveld refinement methods. The results are shown in Figs.4.1 (a) and (b). First, I focused on the analysis of the cubic Mn_3Sb. Based on the structural model of Mn_3Sb synthesized under high-pressure conditions reported in 2003 [106], I attempted to refine the structure using a cubic-ordered model (Pm-3m). I also examined a disordered model, such as that observed in $Mn_{2.8}Ir_{1.2}$ (Pm-3m) [120], but in this study, analysis using a perfectly ordered model was found to be optimal. Ultimately, the analysis proceeded with a complete occupancy for each site of Mn and Sb atoms. The obtained structural parameters yielded reasonable values, as summarized in Table 4.1. A structural image of the cubic Mn_3Sb was drawn based on these results and is presented as an inset in Fig.4.1 (a).

In this study, it was not possible to directly reference past models for hexagonal Mn_3Sb as there were no examples available. Therefore, structural models of Mn_3Sn and Mn_3Ge were referred to Refs. [121–123]. In previous studies of the hexagonal model ($P6_3/mmc$), structures with disorders, including antisite disorder, were observed. However, during the preliminary analysis of my sample, the degree of disorder was estimated to be quite small. Therefore, in the final analysis, an ordered structure model with no antisite disorder was assumed, and all element occupancy factors were set to 1. Despite this assumption, I believe that reasonable results were

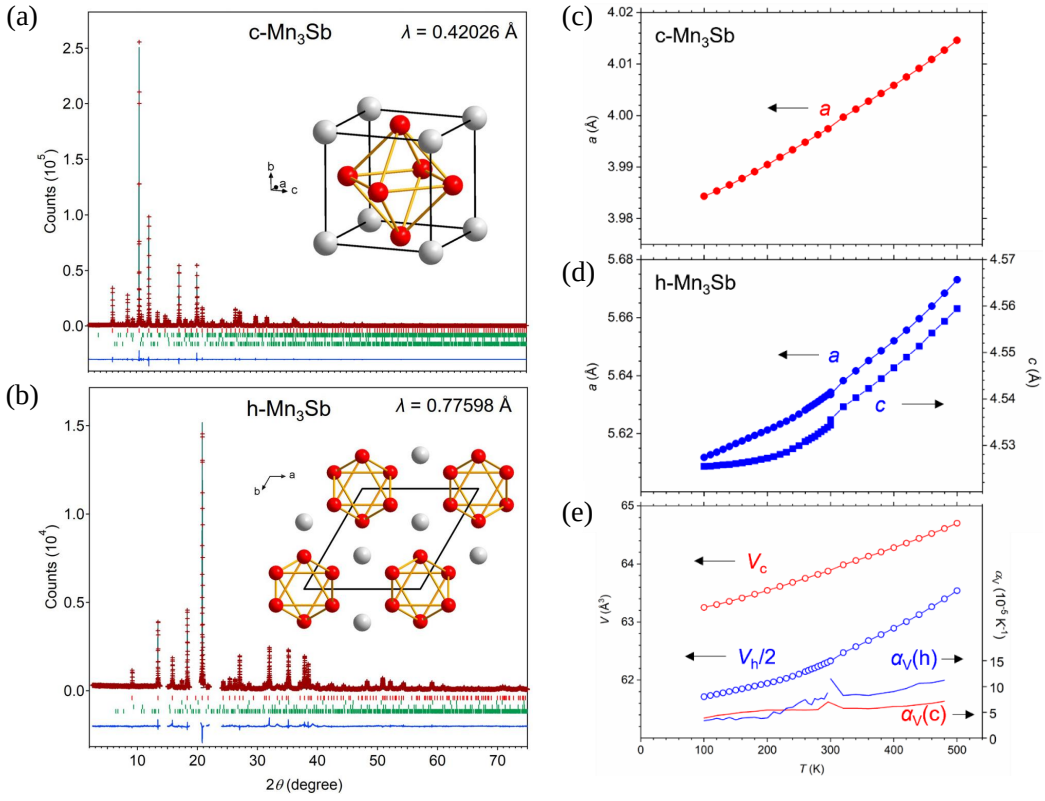

Figure 4.1: Synchrotron XRD patterns of (a) cubic and (b) hexagonal Mn_3Sb at room temperature, showing observed (crosses) and calculated (solid red lines) patterns. Differences are shown as solid blue lines at bottom. Bragg reflections are indicated by vertical ticks, with upper row representing main phase reflections (red) and lower row representing impurity phase reflections (green). Impurity phases include MnO (6.7 wt.%), Mn_2Sb (2.3 wt.%), and Sb (1.3 wt.%) for cubic Mn_3Sb, and MnO and unidentified phases for hexagonal Mn_3Sb. Unit cells are shown as insets, with Mn and Sb denoted by red and gray balls, respectively. (c)–(e) Temperature dependence of the lattice parameters (a and c) and volume (V) of the cubic (Pm-$3m$) and hexagonal ($P6_3/mmc$) unit cells of Mn_3Sb obtained using synchrotron XRD. Error bars are smaller than each symbol. Coefficient of thermal expansion (α_V) is calculated from the V data.

obtained. Therefore, I conclude that hexagonal Mn_3Sb has the same type of structure as Mn_3Sn and Mn_3Ge, and the degree of disorder in the arrangement of elements can be quite small. The x-ray diffraction pattern of the analyzed hexagonal Mn_3Sb is shown in Fig.1(b), and detailed crystallographic data are presented in Table I. A structural image drawn based on the parameters obtained here is also shown as an inset figure.

In addition, synchrotron XRD patterns were collected at various temperatures ranging from 100 to 500 K to investigate the temperature dependence of the structural properties of Mn_3Sb in cubic and hexagonal phases. However, no changes in symmetry or additional features were observed. Only monotonic changes in the structural parameters were observed in response to temperature variations [Fig.4.1 (c)-(e)]. Magnetic measurements taken at high temperatures, which will be discussed later, suggested signs of thermal decomposition above 400 K. However, even at temperatures above 400 K, the synchrotron XRD studies did not observe complete decomposition.

Magnetization

I investigated the magnetic properties of both cubic and hexagonal Mn_3Sb. Figure 4.2 (a) shows the temperature dependence of the magnetic susceptibility of cubic Mn_3Sb at an applied magnetic field of 1 T. As the magnetic transition temperature exceeded 300 K, I employed the oven mode of MPMS3 for the measurements. However, I were unable to determine the precise transition temperature due to the partial decomposition around 450 K. This phenomenon has been reported in prior studies [124]. Therefore, I could only conclude that the magnetic transition temperature of cubic Mn_3Sb was higher than the thermal decomposition temperature of 450 K. Similarly, the magnetic transition temperature of hexagonal Mn_3Sb could not be precisely determined due to the partial decomposition [Fig.4.2(b)]. I just found that the magnetic transition temperature was higher than the thermal decomposition temperature of approximately 420 K. The remarkable upturn observed at high temperatures may be attributed to the formation of MnSb, which is FM and has a Curie temperature of ~550 K [125, 126].

In the cubic Mn_3Sb, a divergence between the ZFC and FC curves was observed at temperatures below 25 K. This divergence may indicate the formation of magnetic domains related to the thermal history. However, more precise studies are necessary to accurately assess this possibility.

Figures 4.2 (c) and (d) summarize the results of measuring the magnetic field dependence of the magnetization of cubic and hexagonal Mn_3Sb at various temperatures, respectively. The magnetization of cubic Mn_3Sb shows hysteresis loops from low temperatures to room temperature, but the magnitude is quite small, with a residual magnetization ($\mu_0 H = 0$) of about 0.004 μ_B/Mn at 300 K. Therefore, it is not FM or ferrimagnetic, but rather close to characteristics of antiferromagnetism. It is thought that a slight spontaneous magnetization was observed because the AFM cancellation was not complete. On the other hand, the magnetic field dependence of the magnetization of hexagonal Mn_3Sb is very linear regardless of temperature and behaves like typical antiferromagnetism. The measurement result of hexagonal Mn_3Sb is qualitatively different from that of Mn_3Sb with the same crystal structure, showing a small residual magnetization and hysteresis loop.

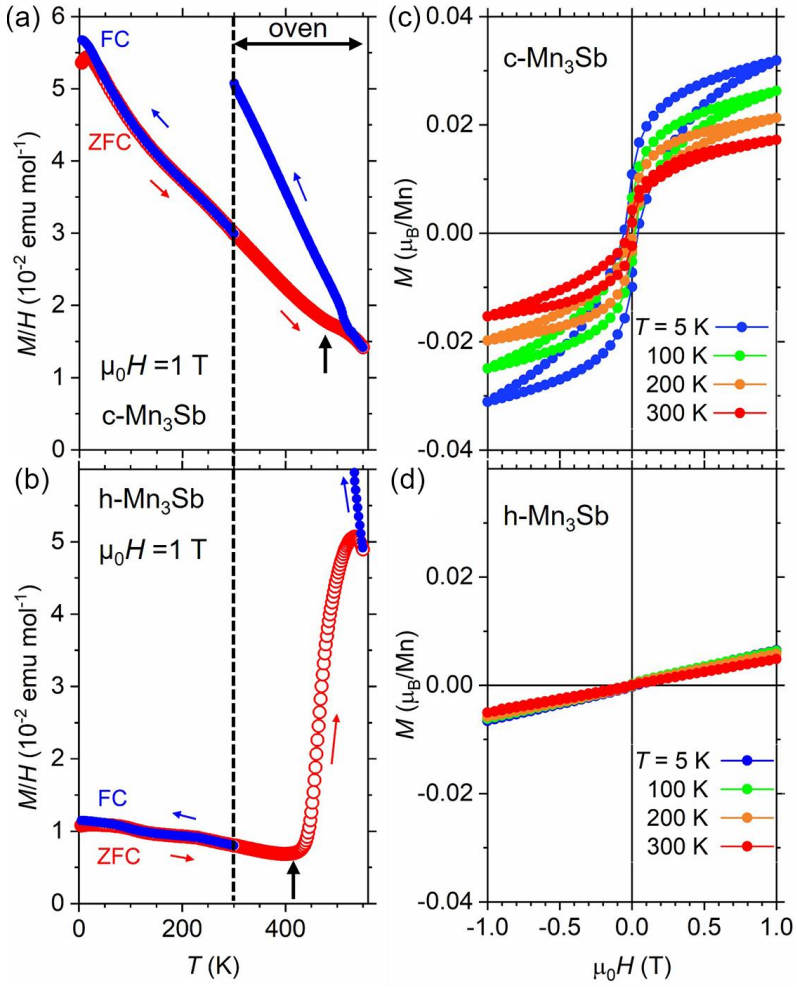

Figure 4.2: (a) Temperature dependence of magnetic susceptibility measured at $\mu_0 H$ = 1 T. (b) Isothermal magnetization curves at various temperatures for cubic Mn_3Sb. (c) Temperature dependence of magnetic susceptibility and (d) isothermal magnetization curves for hexagonal Mn_3Sb. Measurements were carried out using oven mode of MPMS3 for temperatures above 300 K. Black arrow denotes temperature at which Mn_3Sb partially decomposes into Mn_2Sb and Mn.

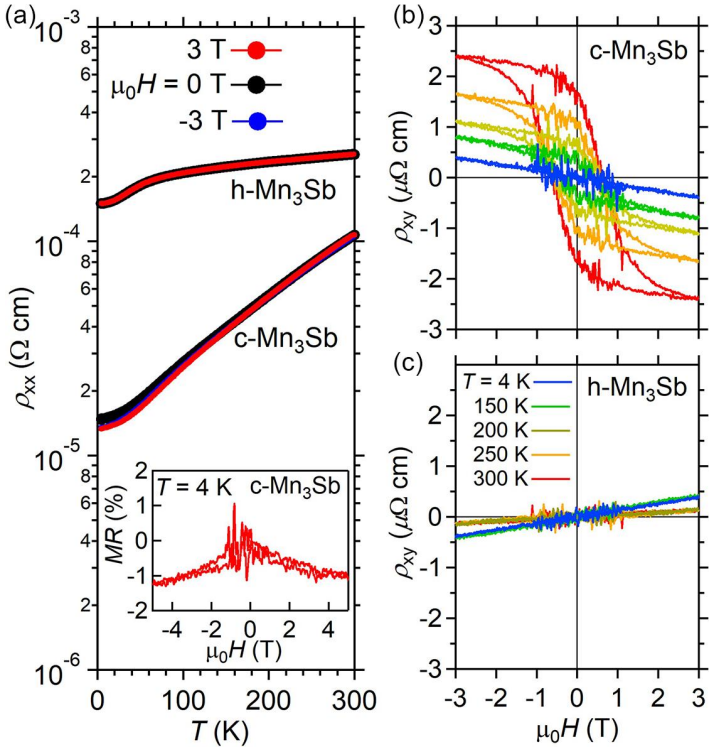

Figure 4.3: (a) Temperature dependence of electrical resistivity of cubic and hexagonal Mn_3Sb under various magnetic fields. Inset shows magnetoresistance of cubic Mn_3Sb at 4 K. (b) Hall resistivity of cubic and (c) hexagonal Mn_3Sb at various temperatures.

Transport properties

Figure 4.3 (a) shows the temperature dependence of ρ_{xx} for Mn_3Sb with both cubic and hexagonal structures. Both materials exhibit metallic conduction behavior from 4 to 300 K at $\mu_0 H = 0$ and ± 3 T, despite being sintered bulk materials. The resistivity at room temperature is relatively low, at around 1×10^{-4} cm, and decreases further as the temperature decreases. Therefore, the impact of grain boundaries and impurities is quite small in the longitudinal direction. Little magnetic field dependence is observed for hexagonal Mn_3Sb, whereas slight magnetic field dependence is observed for cubic Mn_3Sb at low temperatures. The measurement results at 4 K, defined by the magnetic resistivity, $\mathrm{MR}(H) = 100 \times [\rho_{xx}(H) - \rho_{xx}(0)/\rho_{xx}(0)]$, are also presented in the figure. Even at $\mu_0 H = 4$ T, the maximum change observed is only -1‰, suggesting that the suppression of spin fluctuations in an external magnetic field has only a minor effect on the decrease in magnetic resistivity.

The results of measuring the Hall resistivity at several typical temperatures for cubic and hexagonal Mn_3Sb are shown in Figs.4.3 (b) and (c), respectively. Clear AHE was observed in cubic Mn_3Sb. Since sintered samples were used for both measurements, the dependence on crystal orientation could not be studied. However, at 300 K, the absolute value of the Hall resistivity at zero magnetic field ($\mu_0 H = 0$) was as large as 1.68×10^{-6} cm, which is comparable to that of a FM material [5, 127]. Although a direct comparison is difficult due to the difference

in measurement conditions (not single-crystal measurements), the value observed in hexagonal Mn_3Sb and Mn_3Ge ($1 \sim 4 \times 10^{-6}$ cm) is similar [80, 128–131]. In addition, in the measurement of hexagonal Mn_3Sb, which has the same crystal structure as hexagonal Mn_3Sn and Mn_3Ge, no AHE was observed at either low or room temperature [Fig.4.3 (c)]. Therefore, the AHE in cubic Mn_3Sb is particularly noteworthy. Furthermore, the AHE of cubic Mn_3Sb decreases monotonically with a decrease in sample temperature and is almost eliminated in the measurement at 4 K. Such thermal behavior of AHE is usually not observed in FM materials, indicating that the observed AHE reflects the inherent properties of cubic Mn_3Sb.

Magnetic structure

The magnetic structure of cubic Mn_3Sb was initially determined by Ryzhkovskii et al. using neutron diffraction in 2011 [124]. However, a subsequent Mössbauer study contradicted the originally proposed collinear AFM spin structure [132]. Instead, the noncollinear triangular AFM model on the kagome lattice, proposed for Mn_3X(X = Ir, Pt, Rh), was considered [133–135]. In 2020, the magnetic structure model for cubic Mn_3Sb was revisited, and the triangular AFM model was reintroduced based on neutron-diffraction experiments [136]. Despite the limited clarity in determining the magnetic structure through symmetry analysis of powder neutron-diffraction data [137], further experimental progress remains challenging. In this study, I reevaluate the proposed magnetic structure models using first-principles calculations.

Table 4.2 presents the results of theoretical calculations for the possible magnetic structure models of cubic Mn_3Sb. The collinear AFM model demonstrated in the initial neutrondiffraction experiment was not stable, and the noncollinear AFM structure, as observed in the isostructural cubic Mn_3X(X = Ir, Pt, Rh), was found to be the most energetically stable. These theoretical results are consistent with the revisited neutron-diffraction experiments [136]. After optimizing the crystal structure, the numerical results were similar, and the noncollinear AFM model was once again suggested to be the most energetically stable. Attempts were also made to predict the magnitude of magnetization per unit cell using this magnetic structure model. However, technical challenges prevented an accurate quantitative evaluation of the magnitude of magnetization.

The proposed magnetic structure in this study is supported by a combination of experimental evidence from neutron diffraction [136], symmetry analysis [137], Mössbauer spectroscopy [132], first-principles calculations, and magnetization measurements. The nearly coplanar triangular magnetic structure, as shown in the inset of Fig.4.4, is highly likely to be the most probable configuration. This magnetic structure model is also consistent with the model observed in Mn_3Ir [120, 138]. It is important to note that the magnetic structure of hexagonal Mn_3Sb was not investigated in this study due to a technical difficulty caused by the limited sample quantity (<10 mg) available for experimental studies.

4.1.3 Discussion

The Hall conductivity (σ_{xy}) of cubic Mn_3Sb was determined after removing the applied magnetic field (> 1 T) using the equation $\sigma_{xy} = -\rho_{xy}/(\rho_{xy}^2+\rho_{xx}^2)$, where ρ_{xy} is -1.68×10^{-6} cm and ρ_{xx} is 1.07×10^{-4} cm (at 300 K with $\mu_0 H = 0$). The calculated value of σ_{xy} is 146 Ω^{-1}cm^{-1}, which is significantly larger than the room-temperature values of Mn_3Sn (20 Ω^{-1}cm^{-1}) [80] and Mn_3Ge (60 Ω^{-1}cm^{-1}) [128,129] (see Table 4.3), but comparable to the maximum value of Mn_3Sn (130 Ω^{-1}cm^{-1} at 50 K) and approximately 40% of the maximum value of Mn_3Ge (380 Ω^{-1}cm^{-1}

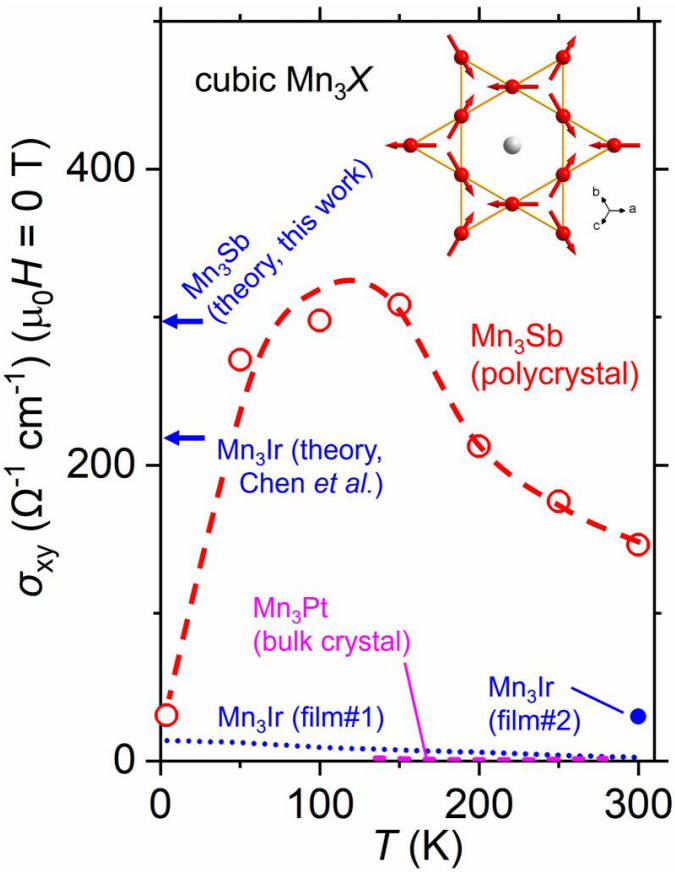

Figure 4.4: Temperature dependence of σ_{xy} in polycrystalline cubic Mn_3Sb. Data used for comparison with other isostructural materials were obtained from Refs. [75, 139, 140] for Mn_3Ir and from Ref. [141] for Mn_3Pt, but unfortunately, experimental data could not be obtained for Mn_3Rh [142]. Inset figure is a schematic of noncollinear AFM structure proposed for Mn_3Sb.

Table 4.2: Relative total energies (eV/cell) calculated within the GGA+SOC scheme for cubic Mn_3Sb

Cubic Mn_3Sb	a(Å)	$M(\mu_B$/cell)	ΔE(eV/cell)
Nonmagnetic	3.997[a]	0	0
Ferromagnetic	3.997[a]	8.48	−2.08
Collinear AFM	3.997[a]	2.10	−2.47
Noncollinear AFM	3.997[a]	∼ 0	−2.57
After structure optimization:			
Nonmagnetic	3.742	0	0
Ferromagnetic	3.805	6.07	−1.46
Collineaar AFM	3.840	2.06	−1.51
Noncollinear AFM	3.909	∼ 0.04	−1.61

[a] Experimental value obtained in this study.
In noncollinear antiferromagnetic (AFM) scheme, magnetic moments are oriented triangularly within [111] plane of cubic cell, as proposed in a neutron-diffraction study [136].

below 50 K) [128, 129] (see Table 4.3). To compare the AHE of cubic Mn_3Sb with other cubic $Mn_3X(X$ = Ir, Pt, Rh) that possess the same spin structures, the σ_{xy} at zero magnetic fields ($\mu_0 H = 0$) was plotted as a function of temperature in Fig.4.4.The value of σ_{xy} increased as the temperature decreased, reaching a peak of approximately $300\,\Omega^{-1}\mathrm{cm}^{-1}$ around 150 K. This value significantly surpasses the experimental values observed for other cubic Mn_3X throughout the entire temperature range, whether they are single crystals or polycrystals. It should be noted that the data for Mn_3Sb used in this study are from polycrystalline materials, and the value of σ_{xy} may be somewhat underestimated compared to theoretical values for single-domain crystals due to angle averaging. However, the observed AHE in polycrystalline Mn_3Sb remains significant and provides valuable information about the AHE behavior in this material.

The observed discrepancy between $Mn_3X(X$ = Ir, Pt, Rh) and Mn_3Sb may potentially be attributed to differences in the magnitude of the magnetic anisotropy among these materials, as suggested by thin-film studies on Mn_3Ir [140]. However, even with some alignment of domains at a high magnetic field of 24 T to the Mn_3Ir film, the measured σ_{xy} remains significantly lower than the theoretical value, being an order of magnitude smaller [139].

It is noteworthy that the σ_{xy} of cubic Mn_3Sb gradually decreases below 150 K, unlike the behavior observed in ferromagnets [5] and hexagonal Mn_3Ge [129], which converge to a constant value in the low-temperature limit. In an attempt to elucidate this behavior, I employed the universal scaling approach proposed for magnetic metals (Fig.4.5) [129, 143]. The analysis reveals that the anomalous Hall conductivity of cubic Mn_3Sb at around room temperature exhibits a behavior that is highly consistent with the expected properties of the intrinsic AHE, which demonstrates a weak dependence on the longitudinal conductivity. However, the pronounced decrease in anomalous Hall conductivity at low temperatures deviates from universal scaling but still falls within the range of intrinsic behavior. Furthermore, I have carefully examined magnetic susceptibility data and crystal structure parameters, but I have not observed any anomalies that could suggest the causes for the pronounced decrease in σ_{xy} at low temperatures. Additionally, it is worth noting that a significant decrease in σ_{xy} at low temperatures has also been observed

Table 4.3: Comparison of experimentally observed anomalous Hall effects at 298-300 K in cubic Mn_3X and hexagonal Mn_3Z materials. The second-to-last column quantifies the anomalous Hall conductivity relative to the material's magnetization.

Materials	Space group	T_N (K)	$\lvert\sigma_{xy}\rvert$ ($\mu_0 H = 0$) (Ω^{-1} cm^{-1})	$M(\mu_0 H = 0)$ (μ_B ion^{-1})	$\lvert\sigma_{xy}\rvert/M_r$ ($10^3\ \Omega^{-1}$ cm$^{-1}\mu_B^{-1}$ ion)
Mn_3Ir	$Pm\text{-}3m$	960 ± 10	2.6/30	0.01	0.3
Mn_3Pt	(Cubic)	473	1.5	0.0003	5
Mn_3Rh		853			
Mn_3Ga		400	0	0	
Mn_3Sb*		> 450	146	0.0032	46
Mn_3Sn	$P6_3/mmc$	430	20	0.003	6.7
Mn_3Ge	(Hexagonal)	380	60	0.007	8.6
Mn_3Ga		470 ± 10	17	0.07	0.2
Mn_3Sb*		> 400	0	0	

* This work

in Mn_3Sn, which is associated with amagnetic structure transition. However, neutron-diffraction studies of cubic Mn_3Sb by Ryzhkovski et al. did not detect any indications of different magnetic features emerging at 77 K [124, 136]. The underlying cause of the decrease in σ_{xy} at low temperatures remains unclear based on my present investigation.

In this study, the anomalous Hall resistivity and remanent magnetization showed continuous variations with temperature (Figs.4.2, 4.3), without displaying any abrupt changes. To summarize the temperature-dependent behaviors, the anomalous Hall conductivity per remanent magnetization was plotted against temperature, as depicted in Fig.4.6. $|\sigma_{xy}|/M_r = 46000(\Omega^{-1}\text{cm}^{-1}\mu_B^{-1}$ ion) near room temperature, gradually increased with decreasing temperature, reaching a maximum at around 150 K, and then exhibited a slow decrease at lower temperatures. No clear abrupt change can be observed, and the underlying reason for the decrease in σ_{xy} at low temperatures still remains unclear. Further analysis of the anomalous Hall conductivity at low temperatures will be necessary in future studies.

The experimental values of σ_{xy} obtained in this study quantitatively agree with the theoretical values calculated from the Berry curvature using the Wannier function for the cubic kagome antiferromagnet Mn_3Sb, as indicated by the arrow in Fig.4.4. It should be noted that the data presented in Fig.4.4 are angle-averaged values in polycrystals, which may result in some underestimation compared to theoretical values for single-domain crystals due to angular averaging. Nevertheless, the agreement between the experimental and theoretical values provides strong evidence for the presence of a significant anomalous Hall effect in the cubic Mn_3Sb material.

It is worth mentioning that when the same method is applied to the cubic kagome antiferromagnet Mn_3Ir, it accurately reproduces the previously reported theoretical values (the band dispersion for Mn_3Ir is also essentially identical to the previous report, as shown in Fig.4.7) [118]. Moreover, a comparative analysis of the calculated Fermi energy dependence of σ_{xy} between cubic Mn_3Sb and cubic Mn_3Ir (Fig.4.8) reveals that σ_{xy} is nearly identical at the Fermi level for both materials. However, the behavior of σ_{xy} in Mn_3Ir exhibits a sharp transition as the

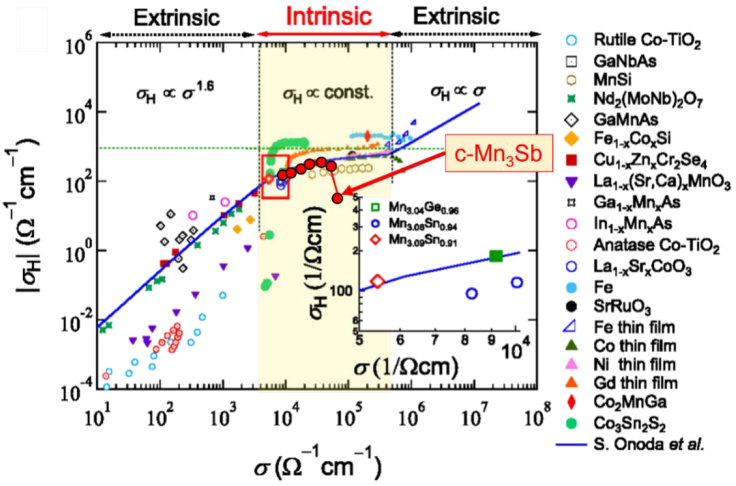

Figure 4.5: Universal scaling relation between the Hall conductivity (σ_H) and the longitudinal conductivity (σ) of magnetic metals (taken from reference [129]). The red circled dots in the black frame correspond to the measured points of cubic Mn_3Sb in the current study. The leftmost data point represents the measurement taken at a temperature of 300 K. As the temperature decreases, the data point moves toward the right. The rightmost measurement point, taken at 5 K, is considerably far from the theoretical curve.

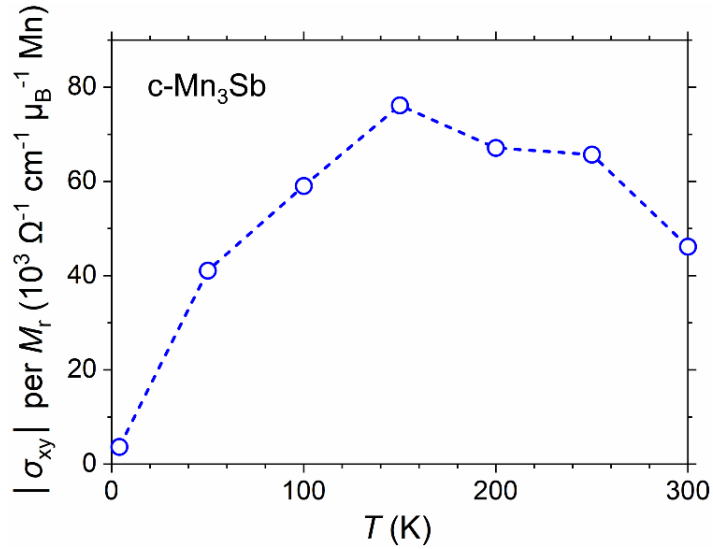

Figure 4.6: Temperature dependence of the Hall conductivity normalized by the remanent magnetization of cubic Mn_3Sb.

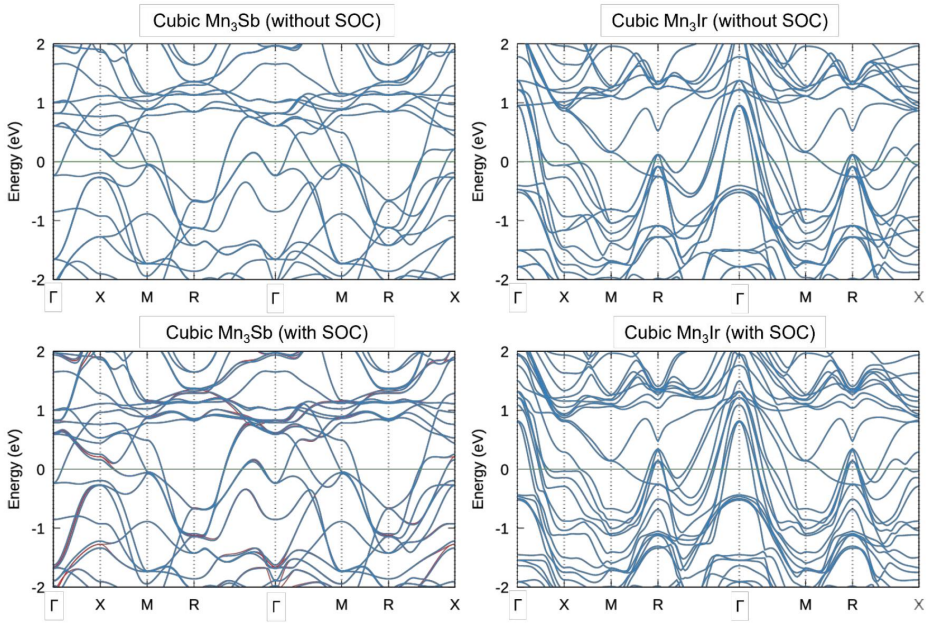

Figure 4.7: Band structures of cubic Mn_3Sb (left) and Mn_3Ir (right) are shown. The upper and lower panels show the band structures calculated with and without SOC, respectively. The spin moments of Mn atoms are assumed to be non-collinear. The results for Mn_3Ir are in close agreement with those in the literature [10]. The modification of the band structure by SOC is smaller for Mn_3Sb than that for Mn_3Ir. For comparison, the band structure without SOC is shown with thin red lines in the lower left panel. At several k points, the energy bands near the Fermi energy split due to SOC. This splitting generates non-zero Berry curvature, resulting in anomalous Hall conductivity.

Fermi energy varies, while in Mn_3Sb, σ_{xy} changes gradually over a relatively wide range of energy. For instance, in the case of Mn_3Ir, it is predicted that the sign of σ_{xy} will reverse with a decrease in Fermi energy of approximately 0.04 eV. In contrast, for Mn_3Sb, the sign of σ_{xy} is expected to remain unchanged even with a decrease in Fermi energy of 0.2 eV or more. These findings suggest that the anomalous Hall conductivity of cubic Mn_3Sb exhibits greater robustness compared to cubic Mn_3Ir against various perturbations that influence the Fermi energy. This unique characteristic of cubic kagome antiferromagnet Mn_3Sb may prove advantageous for the development of novel AFM spintronic materials, as it indicates a more stable and reliable behavior of the AHE in this compound.

For comparison, I performed theoretical calculations using the same approach for Mn_3Rh and Mn_3Pt. However, the calculated values of σ_{xy} for these materials are significantly smaller than those for Mn_3Ir and Mn_3Sb (Table 4.4). Furthermore, the calculated σ_{xy} exhibits a sharp transition near the Fermi energy, indicating their susceptibility to changes in energy. These findings suggest that Mn_3Rh and Mn_3Pt are not as robust as Mn_3Sb in terms of the anomalous Hall conductivity against variations in energy.

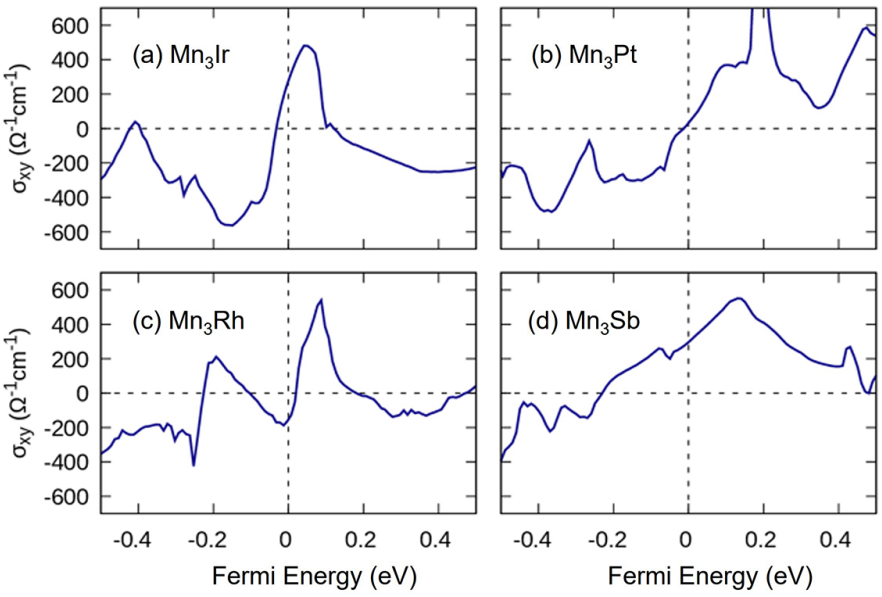

Figure 4.8: (a)–(d) Theoretical calculation of anomalous Hall conductivity for cubic Mn_3X (X = Ir, Pt, Rh, and Sb) using Wannier functions and Berry curvature.

4.1.4 Conclusion

This study has made significant progress in observing the AHE in the cubic kagome antiferromagnet Mn_3Sb. The measured anomalous Hall conductivity of up to $308\,\Omega^{-1}\text{cm}^{-1}$ in polycrystalline cubic Mn_3Sb is a remarkable achievement. This value not only agrees well with theoretical calculations based on Berry curvature but also compares favorably to experimental observations in the hexagonal kagome antiferromagnet $Mn_3Z(Z = \text{Sn, Ge})$. The absence of AHE in the hexagonal Mn_3Sb phase, although not fully understood, does not impact the conclusions drawn in this study. The primary focus of this research is on investigating the AHE in the cubic Mn_3Sb, where significant AHE behavior is observed.

I acknowledge the limitations of comparing AHE and Berry curvature fields in polycrystalline materials. While the anomalous Hall conductivity in polycrystalline materials may be underestimated compared to theoretical values for singledomain crystals due to angular averaging, it still provides important insights into the overall behavior of the AHE. Additionally, I believe Berry curvature calculations offer valuable theoretical insights and help interpret experimental results, even in polycrystalline materials.

I recognize the challenges in accurately determining the contributions of intrinsic and extrinsic factors in polycrystalline materials. The analysis of scaling relations in this study supports the presence of intrinsic AHE in cubic Mn_3Sb, exhibiting the expected behavior with a weak dependence on longitudinal conductivity (Fig.4.5). The observed decrease in anomalous Hall conductivity at low temperatures, while deviating from universal scaling, is still within the range of intrinsic behavior. Further investigations will be pursued once single-domain crystals become available to gain a more comprehensive understanding of these phenomena.

These findings demonstrate that the experimental challenges encountered in studying cubic kagome antiferromagnets, such as Mn_3Ir, Mn_3Pt, and Mn_3Rh, are not inherent limitations of

Table 4.4: Comparison of anomalous Hall effects from firstprinciples calculations in cubic Mn_3X materials.

Materials	σ_{xy} ($cm^{-1}\Omega^{-1}$) (z//[111])	σ_{xy} ($cm^{-1}\Omega^{-1}$) (z//[001])	By Zhang *et al.* [118]	By chen *et al.* [75]
Mn_3Ir	277	160	−312	218
Mn_3Pt	33	19	98	
Mn_3Rh[a]	−152	−88	−284	
Mn_3Sb	296	171		

[a]For Mn_3Rh, calculated value deviates from previous calculations. Deviation could be due to differences in lattice constants or other conditions, as calculated anomalous Hall conductivity is sensitive to position of Fermi energy, as shown in Fig.4.8 (a).

the system itself. This contributes to a deeper understanding of the AHE in both cubic kagome antiferromagnets Mn_3X and hexagonal kagome antiferromagnets Mn_3Z, advancing research on the functions and control of cluster multipoles. Furthermore, the substitution of expensive and scarce noble metals Ir, Pt, and Rh with Sb in this study showcases the potential for developing innovative noncollinear AFM spintronic materials.

Chapter 5

Conclusion

In this study, three skyrmion candidates of Gd-based intermetallic compounds and one antiferromagnet indicating large anomalous Hall conductivity are investigated. The crystal structures, magnetic properties, and transport properties based on spin textures are discussed in detail. I summarize their novel suggestions for each compounds.

5.1 Skyrmion candidates

$GdOs_2Si_2$

Single crystals of $GdOs_2Si_2$, have successfully grown using Czochralski method, which possesses centrosymmetric lattice ($ThCr_2Si_2$-type, $I4/mmm$). Based on the physical property measurements, the magnetic phase diagrams for $H \parallel [100]$ and [001] were established. They are broadly similar to that of $GdRu_2Si_2$, an isostructural compound that exhibits a square skyrmion lattice. In addition, a novel phase that does not exist in $GdRu_2Si_2$ just above the double-Q skyrmion phase in the diagram ($H \parallel [001]$) is found. The topological Hall effect observed in the skyrmion phase is completely suppressed in this new phase, which strongly suggests that it is a theoretically anticipated double-Q trivial phase. This finding emphasizes the singularity of the topological skyrmion phase in a centrosymmetric lattice system.

Gd_2NiSi_3

Single crystals of Gd_2NiSi_3, substituting Pd to Ni in Gd_2PdSi_3 have successfully grown using floating zone method. Gd_2NiSi_3 has a centrosymmetric crystal structure (AlB_2-type, $P6_3/mmm$) with Gd^{3+}triangular lattice, which is a good candidate of magnetic frustration system and censtosymmetric skyrmion compounds. Magnetization measurements revealed a positive Weiss temperature θ_W = +11.3 K and an antiferromagnetic transition at T_N = 13.6 K, certainly manifesting the effects of magnetic frustration. The produced magnetic field-temperature phase diagram is similar to that of Gd_2PdSi_3, with a pronounced anomaly in Hall resistivity observed in the skyrmion phase. The topological Hall resistivity was extracted from this data, and a clear topological Hall effect appeared, reflecting either the emergence of skyrmion lattices or topological spin textures.

$Gd_2Rh_3Al_3$

Single crystals of a new Gd-based intermetallic $Gd_2Rh_3Al_3$ were successfully grown using high-pressure and high-temperature method. The crystal crystallizes in orthorhombic $Y_2Co_3Ga_3$-type structure ($Cmcm$) with alternating slightly distorted Gd-honeycomb and Rh-triangular layers, which system is expected as a candidate for skyrmion-host materials. The successive transitions at T_1 = 13.6 K and T_2 = 4.1 K under the field of 0.1 T, indicating the effective antiferromagnetic interaction on the Gd^{3+} (S = 7/2) network is qualitatively similar to other skyrmion materials, however the negative value of Weiss temperature θ_W = -31.8 K implies the opposite property. In conclusion, $Gd_2Rh_3Al_3$ did not provide evidence for the existence of a skyrmion phase. This may be attributed, at least in part, to the significantly stronger antiferromagnetic interactions compared to other Gd-based skyrmion materials. Anomalies observed in specific heat and electrical resistivity consistent with antiferromagnetic transitions.

The characteristics of skyrmions

In this section, I discuss the size of the skyrmions and the characteristics of the induced topological Hall effect in $GdOs_2Si_2$ and Gd_2NiSi_3. Currently, the world's smallest skyrmion lattice has a diameter of 1.9 nm and is formed on Gd ions in the c-plane of $GdRu_2Si_2$. Here, a comparison of the lattice constants of $GdOs_2Si_2$ and $GdRu_2Si_2$ found in previous studies is shown in Table 5.1. From Table 5.1, $GdOs_2Si_2$ is slightly shrunk in a (= b) (blue) and stretched in c (red) direction compared to $GdRu_2Si_2$: in other words, the c-plane shrinks by pulling in the c-axis direction. Hence, in $GdOs_2Si_2$, a skyrmion lattice of less than 1.9 nm is expected, although this is only a guess. To identify the actual size of the skyrmion lattice, experiments using resonant X-ray diffraction and electron microscopy such as Lorentz TEM are required, and this is a future prospect.

Next, I discuss the characteristics of topological Hall effect in Gd_2NiSi_3. The topological Hall effect observed in Gd_2NiSi_3 is $\rho_{yx}^{T} \sim 2.6\ \mu\Omega$ cm, which is much larger than other Gd-based skyrmion compounds such as $GdRu_2Si_2$ and $GdEu_4$. The nature of this difference is under discussion at present, although it can be assured that the size of skyrmion lattice is different in both: Gd_2PdSi_3 has a skyrmion size of several hundred nm and exhibits a larger topological Hall resistivity. The topological Hall resistivity of Gd_2NiSi_3 revealed in this thesis is $\rho_{yx}^{T} \sim 0.5$, which is a relatively small value, indicating that a smaller skyrmion lattice may be manifest. However, electrical conductivity is affected not only spin textures but also impurity effects etc., thus, further measurements are required as with $GdOs_2Si_2$.

Table 5.1: The lattice constant and observed (expected) skyrmion size in $GdOs_2Si_2$ and $GdRu_2Si_2$.

	$GdOs_2Si_2$	$GdRu_2Si_2$
Space group	$I4/mmm$	$I4/mmm$
a (Å)	4.1549	4.1634
c (Å)	9.8117	9.6102
Skyrmion size (nm)	**<1.9**	1.9

5.2 Large anomalous Hall conductivity

Mn_3Sb

The large anomalous Hall conductivity in a series of cubic antiferromagnet Mn_3X have successfully observed for the first time, using polycrystalline Mn_3Sb, although such anomalous Hall effect is typically observed in ferromagnetic metals or in certain non-collinear antiferromagnetic states. The measured value is comparable to the theoretical value and more than 50 times larger than the experimental observation for Mn_3Ir (at 300 K). This result suggests that the experimental issues reported so far in cubic antiferromagnet Mn_3X (X = Ir, Pt, Rh) are not essential, and further studies will enhance the possibility of developing new antiferromagnetic spintronic materials characterized by cluster-multipole moments.

Comparison of Hall conductivity

The calculated value of σ_{xy} is 146 Ω^{-1} cm^{-1}, which is significantly larger than the room temperature values of Mn_3Sn (20 Ω^{-1} cm^{-1}) and Mn_3Ge (60 Ω^{-1} cm^{-1}), but is comparable to the maximum value of Mn_3Sn (130 Ω^{-1} cm^{-1} at 50 K) and nearly 40% of the maximum value of Mn_3Ge (380 Ω^{-1} cm^{-1} below 50 K). Despite having different magnetic structure, cubic Mn_3Sb exhibits nearly comparable σ_{xy} values with hexagonal Mn_3Ge and Mn_3Sn. Hence, exploring the mechanism of the large anomalous Hall effect in cubic Mn_3Sb is an important matter.

References

[1] F. Steglich, J. Aarts, C. D. Bredl, W. Lieke, D. Meschede, W. Franz, and H. Schäfer: Phys. Rev. Lett. **43** (1979) 1892.

[2] S. Hayami, M. Yatsushiro, Y. Yanagi, and H. Kusunose: Phys. Rev. B **98** (2018) 165110.

[3] K. Inoue and J. Kishine: Journal of the Crystallographic Society of Japan **53** (2011) 339.

[4] K. Ohgushi, S. Murakami, and N. Nagaosa: Phys. Rev. B **62** (2000) R6065.

[5] N. Nagaosa, J. Sinova, S. Onoda, A. H. MacDonald, and N. P. Ong: Rev. Mod. Phys. **82** (2010) 1539.

[6] M. Lee, W. Kang, Y. Onose, Y. Tokura, and N. P. Ong: Physical Review Letters **102** (2009).

[7] A. Neubauer, C. Pfleiderer, B. Binz, A. Rosch, R. Ritz, P. G. Niklowitz, and P. Boni: Physical Review Letters **102** (2009) 186602.

[8] H. Kusunose: Journal of the Physical Society of Japan **77** (2008) 064710.

[9] Y. Kuramoto, H. Kusunose, and A. Kiss: Journal of the Physical Society of Japan **78** (2009) 072001.

[10] T. Skyrme: Nuclear Physics **31** (1962) 556.

[11] A. N. Bogdanov and D. A. Yablonskii: Soviet Journal of Experimental and Theoretical Physics **68** (1989) 101.

[12] A. Bogdanov and A. Hubert: Journal of Magnetism and Magnetic Materials **138** (1994) 255.

[13] N. Nagaosa and Y. Tokura: Nature Nanotechnology **8** (2013) 899.

[14] B. Berg and M. Luscher: Nuclear Physics B **190** (1981) 412.

[15] S. Muhlbauer, B. Binz, F. Jonietz, C. Pfleiderer, A. Rosch, A. Neubauer, R. Georgii, and P. Boni: Science **323** (2009) 915.

[16] X. Z. Yu, Y. Onose, N. Kanazawa, J. H. Park, J. H. Han, Y. Matsui, N. Nagaosa, and Y. Tokura: Nature **465** (2010) 901.

[17] B. P and J. M, H: Journal of Physics C: Solid State Physics **13** (1980) L881.

[18] I. Dzyaloshinskii: Journal of Physics and Chemistry of Solids **4** (1958) 241.

[19] T. Moriya: Phys. Rev. **120** (1960) 91.

[20] U. K. Roessler, A. N. Bogdanov, and C. Pfleiderer: Nature **442** (2006) 797.

[21] B. Binz, A. Vishwanath, and V. Aji: Phys. Rev. Lett. **96** (2006) 207202.

[22] B. Senyuk, J. Aplinc, M. Ravnik, and I. I. Smalyukh: Nature Communications **10** (2019) 1825.

[23] E. H. Hall: American Journal of Mathematics **2** (1879) 287.

[24] E. Hall: The London, Edinburgh, and Dublin Philosophical Magazine and Journal of Science **10** (1880) 301.

[25] E. Hall: The London, Edinburgh, and Dublin Philosophical Magazine and Journal of Science **12** (1881) 157.

[26] N. Kanazawa, Y. Onose, T. Arima, D. Okuyama, K. Ohoyama, S. Wakimoto, K. Kakurai, S. Ishiwata, and Y. Tokura: Phys. Rev. Lett. **106** (2011) 156603.

[27] Y. Li, N. Kanazawa, X. Z. Yu, A. Tsukazaki, M. Kawasaki, M. Ichikawa, X. F. Jin, F. Kagawa, and Y. Tokura: Phys. Rev. Lett. **110** (2013) 117202.

[28] E. M. Pugh and T. W. Lippert: Phys. Rev. **42** (1932) 709.

[29] E. M. Pugh and N. Rostoker: Rev. Mod. Phys. **25** (1953) 151.

[30] R. Karplus and J. M. Luttinger: Phys. Rev. **95** (1954) 1154.

[31] M. V. Berry: Proceedings of the Royal Society of London Series A **392** (1984) 45.

[32] J. Smit: Physica **21** (1955) 877.

[33] J. Smit: Physica **24** (1958) 39.

[34] L. Berger: Phys. Rev. B **2** (1970) 4559.

[35] Embedded Technology Lab. はじめての人でも分かるホールセンサーの原理と種類. https://emb.macnica.co.jp/articles/10315/, 2020.

[36] S. Luo and L. You: APL Materials **9** (2021) 050901.

[37] Y. Wu, L. Kong, Y. Wang, J. Li, Y. Xiong, and J. Tang: Applied Physics Letters **118** (2021) 122406.

[38] W. Jiang, P. Upadhyaya, W. Zhang, G. Yu, M. B. Jungfleisch, F. Y. Fradin, J. E. Pearson, Y. Tserkovnyak, K. L. Wang, O. Heinonen, S. G. E. te Velthuis, and A. Hoffmann: Science **349** (2015) 283.

[39] G. Yu, P. Upadhyaya, Q. Shao, H. Wu, G. Yin, X. Li, C. He, W. Jiang, X. Han, P. K. Amiri, and K. L. Wang: Nano Letters **17** (2017) 261. PMID: 27966987.

[40] X. Z. Yu, N. Kanazawa, Y. Onose, K. Kimoto, W. Z. Zhang, S. Ishiwata, Y. Matsui, and Y. Tokura: Nature Materials **10** (2011) 106.

[41] N. Kanazawa, J. H. Kim, D. S. Inosov, J. S. White, N. Egetenmeyer, J. L. Gavilano, S. Ishiwata, Y. Onose, T. Arima, B. Keimer, and Y. Tokura: Physical Review B **86** (2012) 134425.

[42] M. Kakihana, D. Aoki, A. Nakamura, F. Honda, M. Nakashima, Y. Amako, T. Takeuchi, H. Harima, M. Hedo, T. Nakama, and Y. Onuki: Journal of the Physical Society of Japan **88** (2019) 094705.

[43] S. Z. Lin and S. Hayami: Physical Review B **93** (2016) 064430.

[44] S. Hayami, R. Ozawa, and Y. Motome: Physical Review B **95** (2017) 224424.

[45] R. Ozawa, S. Hayami, and Y. Motome: Physical Review Letters **118** (2017) 147205.

[46] Z. Wang, Y. Su, S. Z. Lin, and C. D. Batista: Physical Review Letters **124** (2020) 207201.

[47] S. Hayami and Y. Motome: Physical Review B **103** (2021).

[48] A. O. Leonov and M. Mostovoy: Nature Communications **6** (2015) 8275.

[49] T. Okubo, S. Chung, and H. Kawamura: Physical Review Letters **108** (2012).

[50] P. A. KOTSANIDIS, J. K. YAKINTHOS, and E. GAMARI-SEALE: Journal of Magnetism and Magnetic Materials **87** (1990) 199.

[51] R. Mallik, E. V. Sampathkumaran, P. L. Paulose, H. Sugawarat, and H. Sato: PRAMANA journal of physics **51** (1998) 505.

[52] S. R. Saha, H. Sugawara, T. D. Matsuda, H. Sato, R. Mallik, and E. V. Sampathkumaran: Physical Review B **60** (1999) 12162.

[53] T. Kurumaji, T. Nakajima, M. Hirschberger, A. Kikkawa, Y. Yamasaki, H. Sagayama, H. Nakao, Y. Taguchi, T. Arima, and Y. Tokura: Science **365** (2019) 914.

[54] R. E. Gkandyshevskii, O. R. Strusievicz, K. Cenzual, and E. Parthe: Acta Crystal **49** (1993) 474.

[55] V. Chandragiri, K. K. Iyer, and E. V. Sampathkumaran: Journal of Physics Condensed Matter **28** (2016).

[56] M. Hirschberger, T. Nakajima, S. Gao, L. Peng, A. Kikkawa, T. Kurumaji, M. Kriener, Y. Yamasaki, H. Sagayama, H. Nakao, K. Ohishi, K. Kakurai, Y. Taguchi, X. Yu, T. hisa Arima, and Y. Tokura: Nature Communications **10** (2019) 5831.

[57] Y. Yasui, C. J. Butler, N. D. Khanh, S. Hayami, T. Nomoto, T. Hanaguri, Y. Motome, R. Arita, T. hisa Arima, Y. Tokura, and S. Seki: Nature Communications **11** (2020) 5925.

[58] N. D. Khanh, T. Nakajima, X. Yu, S. Gao, K. Shibata, M. Hirschberger, Y. Yamasaki, H. Sagayama, H. Nakao, L. Peng, K. Nakajima, R. Takagi, T. hisa Arima, Y. Tokura, and S. Seki: Nature Nanotechnology **15** (2020) 444.

[59] M. Slaski, A. Szytula, J. Leciejewicz, and A. Zygmunt: Journal of Magnetism and Magnetic Materials **46** (1984) 114.

[60] K. Hiebl, C. Horvath, P. Rogl, and M. J. Sienko: Solid State Communications **48** (1983) 211.

[61] A. Garnier, D. Gignoux, D. S. A', and T. Shigeoka: Physica B **222** (1996) 80.

[62] T. Samanta, I. Das, and S. Banerjee: Journal of Applied Physics **104** (2008) 123901.

[63] F. Jonietz, S. Muhlbauer, C. Pfleiderer, A. Neubauer, W. Munzer, A. Bauer, T. Adams, R. Georgii, P. Boni, R. A. Duine, K. Everschor, M. Garst, and A. Rosch: Science **330** (2010) 1648.

[64] T. Schulz, R. Ritz, A. Bauer, M. Halder, M. Wagner, C. Franz, C. Pfleiderer, K. Everschor, M. Garst, and A. Rosch: Nature Physics **8** (2012) 301.

[65] G. Kimbell, C. Kim, W. Wu, M. Cuoco, and J. W. A. Robinson: Communications Materials **3** (2022) 19.

[66] R. Takagi, N. Matsuyama, V. Ukleev, L. Yu, J. S. White, S. Francoual, J. R. Mardegan, S. Hayami, H. Saito, K. Kaneko, K. Ohishi, Y. Onuki, T. hisa Arima, Y. Tokura, T. Nakajima, and S. Seki: Nature Communications **13** (2022).

[67] R. Ozawa, S. Hayami, K. Barros, G.-W. Chern, Y. Motome, and C. D. Batista: Journal of the Physical Society of Japan **85** (2016) 103703.

[68] Y. Akagi, M. Udagawa, and Y. Motome: Phys. Rev. Lett. **108** (2012) 096401.

[69] M. A. Ruderman and C. Kittel: Physical Review **96** (1954).

[70] T. Kasuya: Progress of Theoretical Physics **16** (1956).

[71] K. Yosida: Physical Review **106** (1957).

[72] R. Shindou and N. Nagaosa: Phys. Rev. Lett. **87** (2001) 116801.

[73] G. Metalidis and P. Bruno: Phys. Rev. B **74** (2006) 045327.

[74] I. Martin and C. D. Batista: Phys. Rev. Lett. **101** (2008) 156402.

[75] H. Chen, Q. Niu, and A. H. MacDonald: Phys. Rev. Lett. **112** (2014) 017205.

[76] J. Kubler and C. Felser: Europhysics Letters **108** (2014) 67001.

[77] Y. Machida, S. Nakatsuji, S. Onoda, T. Tayama, and T. Sakakibara: Nature **463** (2010) 210.

[78] S. Tomiyoshi and Y. Yamaguchi: Journal of the Physical Society of Japan **51** (1982) 2478.

[79] P. J. Brown, V. Nunez, F. Tasset, J. B. Forsyth, and P. Radhakrishna: Journal of Physics: Condensed Matter **2** (1990) 9409.

[80] S. Nakatsuji, N. Kiyohara, and T. Higo: Nature **527** (2015) 212.

[81] T. Nagamiya, S. Tomiyoshi, and Y. Yamaguchi: Solid State Communications **42** (1982) 385.

[82] H. Hayashi, H. K. Yoshida, H. Sakurai, N. Kikugawa, and K. Yamaura: Proceedings of 29th International Conference on Low Temperature Physics, 2022.

[83] A. Garnier, D. Gignoux, N. Iwata, D. Schmitt, T. Shigeoka, and F. Y. Zhang: Journal of Magnetism and Magnetic Materials **140-144** (1995) 899.

[84] N. D. Khanh, T. Nakajima, S. Hayami, S. Gao, Y. Yamasaki, H. Sagayama, H. Nakao, R. Takagi, Y. Motome, Y. Tokura, T. hisa Arima, and S. Seki: Advanced Science **9** (2022).

[85] O. I. Utesov: Physical Review B **103** (2021).

[86] R. Oishi, Y. Shimura, K. Umeo, T. Onimaru, and T. Takabatake: Journal of the Physical Society of Japan **91** (2022).

[87] M. Bouvier, P. Lethuillier, and D. Schmitt: Physical Review B **43** (1991) 13137.

[88] J. A. Blanco, D. Gignoux, and D. Schmitt: Physical Review B **43** (1991) 13145.

[89] H. Hidaka, Y. Ikeda, I. Kawasaki, T. Yanagisawa, and H. Amitsuka: Physica B: Condensed Matter **404** (2009) 3005.

[90] J. Barandiaran, D. Gignoux, D. Schmitt, J. Gomez-Sal, J. R. Fernandez, P. Chieux, and J. Schweizer: Journal of Magnetism and Magnetic Materials **73** (1988) 233.

[91] R. Mallik and E. V. Sampathkumaran: Physical Review B **58** (1998) 9178.

[92] M. Shatruk: Journal of Solid State Chemistry **272** (2019) 198.

[93] S. Pakhira, C. Mazumdar, R. Ranganathan, S. Giri, and M. Avdeev: Phys. Rev. B **94** (2016) 104414.

[94] S. Pakhira, R. Ranganathan, and C. Mazumdar: Journal of Magnetism and Magnetic Materials **512** (2020) 167055.

[95] S. Nakamura, N. Kabeya, M. Kobayashi, K. Araki, K. Katoh, and A. Ochiai: Physical Review B **98** (2018).

[96] S. Nakamura, N. Kabeya, M. Kobayashi, K. Araki, K. Katoh, and A. Ochiai: Physical Review B **107** (2023).

[97] S. Hayami: JPhys Materials **6** (2023).

[98] A. W. Leishman, R. M. Menezes, G. Longbons, E. D. Bauer, M. Janoschek, D. Honecker, L. Debeer-Schmitt, J. S. White, A. Sokolova, M. V. Milosevic, and M. R. Eskildsen: Physical Review B **102** (2020).

[99] M. He, G. Li, Z. Zhu, Y. Zhang, L. Peng, R. Li, J. Li, H. Wei, T. Zhao, X. G. Zhang, S. Wang, S. Z. Lin, L. Gu, G. Yu, J. W. Cai, and B. G. Shen: Physical Review B **97** (2018).

[100] H. Y. Yuan, O. Gomonay, and M. Klaui: Physical Review B **96** (2017).

[101] G. M. Sheldrick: Acta Crystallographica Section A: Foundations of Crystallography **71** (2015) 3.

[102] G. M. Sheldrick: Acta Crystallographica Section C: Structural Chemistry **71** (2015) 3.

[103] T. P. Rashid, K. Arun, I. Curlik, S. Ilkovic, M. Reiffers, A. Dzubinska, and R. Nagalakshmi: Journal of Magnetism and Magnetic Materials **466** (2018) 283.

[104] G. Reiss, J. Vancea, and H. Hoffmann: Physical Review Letters **56** (1986) 2100.

[105] I. material database (AtomWork-adv) Japan: https://atomwork-adv.nims.go.jp/, National Institute for Materials Science .

[106] T. Yamashita, H. Takizawa, T. Sasaki, K. Uheda, and T. Endo: Journal of Alloys and Compounds **348** (2003) 220.

[107] V. S. Goncharov and V. M. Ryzhkovskii: Inorganic Materials **41** (2005) 557.

[108] T. McGuire and R. Happel: J. Phys. Radium **20** (1959) 424.

[109] M. Tanaka, Y. Katsuya, and A. Yamamoto: Review of Scientific Instruments **79** (2008) 075106.

[110] M. Tanaka, Y. Katsuya, and A. Yamamoto: Review of Scientific Instruments **79** (2008) 075106.

[111] H. M. Rietveld: Journal of Applied Crystallography **2** (1969) 65.

[112] F. Izumi and T. Ikeda: European Powder Diffraction 6, Vol. 321 of *Materials Science Forum*, 1 2000, pp. 198–205.

[113] G. Kresse and J. Furthmüller: Phys. Rev. B **54** (1996) 11169.

[114] J. P. Perdew, K. Burke, and M. Ernzerhof: Phys. Rev. Lett. **77** (1996) 3865.

[115] N. Marzari and D. Vanderbilt: Phys. Rev. B **56** (1997) 12847.

[116] I. Souza, N. Marzari, and D. Vanderbilt: Phys. Rev. B **65** (2001) 035109.

[117] G. Pizzi, V. Vitale, R. Arita, S. Blugel, F. Freimuth, G. Geranton, M. Gibertini, D. Gresch, C. Johnson, T. Koretsune, J. Ibanez-Azpiroz, H. Lee, J.-M. Lihm, D. Marchand, A. Marrazzo, Y. Mokrousov, J. I. Mustafa, Y. Nohara, Y. Nomura, L. Paulatto, S. Ponce, T. Ponweiser, J. Qiao, F. Thole, S. S. Tsirkin, M. Wierzbowska, N. Marzari, D. Vanderbilt, I. Souza, A. A. Mostofi, and J. R. Yates: Journal of Physics: Condensed Matter **32** (2020) 165902.

[118] Y. Zhang, Y. Sun, H. Yang, J. Železný, S. P. P. Parkin, C. Felser, and B. Yan: Phys. Rev. B **95** (2017) 075128.

[119] X. Wang, J. R. Yates, I. Souza, and D. Vanderbilt: Phys. Rev. B **74** (2006) 195118.

[120] T. Yamaoka: Journal of the Physical Society of Japan **36** (1974) 445.

[121] S. Tomiyoshi and Y. Yamaguchi: Journal of the Physical Society of Japan **51** (1982) 2478.

[122] S. Tomiyoshi: Journal of the Physical Society of Japan **51** (1982) 803.

[123] E. Kren and G. Kadar: Solid State Communications **8** (1970) 1653.

[124] V. M. Ryzhkovskii, V. S. Goncharov, S. S. Agafonov, V. P. Glazkov, V. A. Somenkov, A. P. Sazonov, and A. T. Senishin: Journal of Surface Investigation. X-ray, Synchrotron and Neutron Techniques **5** (2011) 109.

[125] V. S. Goncharov and V. M. Ryzhkovskii: Inorganic Materials **47** (2011) 1298.

[126] M. Wilkinson, N. Gingrich, and C. Shull: Journal of Physics and Chemistry of Solids **2** (1957) 289.

[127] Y. Yao, L. Kleinman, A. H. MacDonald, J. Sinova, T. Jungwirth, D.-s. Wang, E. Wang, and Q. Niu: Phys. Rev. Lett. **92** (2004) 037204.

[128] N. Kiyohara, T. Tomita, and S. Nakatsuji: Phys. Rev. Appl. **5** (2016) 064009.

[129] T. Chen, T. Tomita, S. Minami, M. Fu, T. Koretsune, M. Kitatani, I. Muhammad, D. Nishio-Hamane, R. Ishii, F. Ishii, R. Arita, and S. Nakatsuji: Nature Communications **12** (2021) 572.

[130] Y. Song, Y. Hao, S. Wang, J. Zhang, Q. Huang, X. Xing, and J. Chen: Phys. Rev. B **101** (2020) 144422.

[131] Z. H. Liu, Y. J. Zhang, G. D. Liu, B. Ding, E. K. Liu, H. M. Jafri, Z. P. Hou, W. H. Wang, X. Q. Ma, and G. H. Wu: Scientific Reports **7** (2017) 515.

[132] M. Budzynski, V. S. Goncharov, V. I. Mitsiuk, Z. Surowiec, and T. M. Tkachenka: Acta Physica Polonica A **125** (2014) 850.

[133] E. Krén, G. Kádár, L. Pál, J. Sólyom, P. Szabó, and T. Tarnóczi: Phys. Rev. **171** (1968) 574.

[134] A. Sakuma, R. Y. Umetsu, and K. Fukamichi: Phys. Rev. B **66** (2002) 014432.

[135] I. Tomeno, H. N. Fuke, H. Iwasaki, M. Sahashi, and Y. Tsunoda: Journal of Applied Physics **86** (1999) 3853.

[136] V. S. Goncharov and S. V. Trukhanov: Vol. 56, Dec 2020.

[137] A. P. Vokhmyanin, A. S. Gritsai, and V. M. Ryzhkovskii: The Physics of Metals and Metallography **113** (2012) 756.

[138] T. Yamaoka, M. Mekata, and H. Takaki: Journal of the Physical Society of Japan **36** (1974) 438.

[139] Y. Kobayashi, M. Kimata, D. Kan, T. Ikebuchi, Y. Shiota, H. Kohno, Y. Shimakawa, T. Ono, and T. Moriyama: Japanese Journal of Applied Physics **61** (2022) 070912.

[140] H. Iwaki, M. Kimata, T. Ikebuchi, Y. Kobayashi, K. Oda, Y. Shiota, T. Ono, and T. Moriyama: Applied Physics Letters **116** (2020) 022408.

[141] B. E. Zuniga-Cespedes, K. Manna, H. M. L. Noad, P.-Y. Yang, M. Nicklas, C. Felser, A. P. Mackenzie, and C. W. Hicks: New Journal of Physics **25** (2023) 023029.

[142] O. Busch, B. Göbel, and I. Mertig: Phys. Rev. Res. **2** (2020) 033112.

[143] S. Onoda, N. Sugimoto, and N. Nagaosa: Phys. Rev. Lett. **97** (2006) 126602.